

FLEXURAL BOND PERFORMANCE OF ANCHORED CFRP LAMINATES TO  
CONCRETE BEAMS

by

Ghusoon Subhi Alshami

A Thesis presented to the Faculty of the  
American University of Sharjah  
College of Engineering  
In Partial Fulfillment  
of the Requirements  
for the Degree of

Master of Science in  
Civil Engineering

Sharjah, United Arab Emirates

December 2021

## **Declaration of Authorship**

I declare that this thesis is my own work and, to the best of my knowledge and belief, it does not contain material published or written by a third party, except where permission has been obtained and/or appropriately cited through full and accurate referencing.

Signature: Ghusoon Alshami.....

Date: 05/12/2021.....

The Author controls copyright for this report.  
Material should not be reused without the consent of the author. Due  
acknowledgement should be made where appropriate.

© Year 2021

Ghusoon S. Alshami

**ALL RIGHTS RESERVED**

## Approval Signatures

We, the undersigned, approve the Master's Project/Thesis of Ghusoon S. Alshami.

Project Title: Flexural Bond Performance of Anchored CFRP Laminates to Concrete Beams.

Date of Defense: 29/11/2021

Name, Title and Affiliation	Signature
Dr. Rami Hawileh Professor, Department of Civil Engineering Thesis Advisor	
Dr. Jamal Abdalla Professor, Department of Civil Engineering Thesis Co-Advisor	
Dr. Farid Abed Professor, Department of Civil Engineering Thesis Committee Member	
Dr. Wael Abuzaid Associate Professor, Department of Mechanical Engineering Thesis Committee Member	
Dr. Lotfi Romdhane Associate Dean for Graduate Affairs and Research College of Engineering	
Dr. Sameer Al-Asheh Interim Dean College of Engineering	
Dr. Mohamed El-Tarhuni Vice Provost for Research and Graduate Studies	

## **Acknowledgment**

I would like to express my genuine gratitude to my advisors, Dr. Rami Hawileh and Dr. Jamal Abdalla, for their continuous support and guidance during my M.Sc. degree in Civil Engineering at the American University of Sharjah. It was an honor to work and study under their guidance. I would like to extend my sincere thanks to my thesis committee, Dr. Farid Abed and Dr. Wael Abizaid, for their insightful comments and for the effort and time devoted to reviewing this dissertation. I would also like to thank the American University of Sharjah for granting me graduate teaching assistantship and providing the financial support that aided in completing this research project.

I would also like to express appreciation to Engineers, Arshi Faridi and Mohammad Ansari for their help in the laboratory work. Moreover, I would like to thank Emirates Beton Readymix LLC. for casting the specimens and Mapei LLC. for providing the materials needed for preparing the test specimens.

Finally, I want to thank my family and friends for their constant encouragement and support throughout my graduate degree. It would have been impossible without their support.

## **Dedication**

*To my beloved parents and family.*

## Abstract

Fiber-reinforced polymer (FRP) composites are being extensively used in retrofitting and strengthening of reinforced concrete (RC) members due to their superior properties such as high strength and corrosion resistance. This form of retrofitting has proven to be effective in enhancing the flexural and shear capacities of RC members. However, the premature debonding of FRP laminates from the concrete substrate prior to utilizing its ultimate strength is a major concern and often results in a brittle member failure. Recent studies have indicated that adequate anchorage systems could improve the FRP-to-concrete bond and delay early debonding of the FRP laminates. The use of carbon-FRP (CFRP) splay anchors as an anchorage system is gaining wide acceptance due to its compatibility with CFRP laminates and its ability to suit a wide range of applications. However, limited studies are available in the literature that examines the effect of different anchor parameters on the laminate bond strength. Hence, this study aims to investigate the effect of different anchor parameters and configurations on the capacity of externally bonded concrete prisms with CFRP laminates. Consequently, the experimental program consisted of 30 concrete prisms that were strengthened with CFRP laminates and anchored with CFRP splay anchors. The parameters investigated were CFRP anchor diameter, embedment depth, and dowel angle. All prisms were tested in flexure under four-point bending tests. Test results showed that anchoring the laminates significantly enhanced the capacity of the prisms and FRP strain utilization compared to the unanchored strengthened prisms. In addition, varying the embedment depth and insertion angle had a significant effect on the capacity of the specimens. The strength improvement in the anchored specimens reached up to 50% over the control unanchored specimens. In addition, bond-slip models for the strengthened specimens are developed based on the obtained experimental data. The outcomes of this study will hopefully aid engineers in the design of FRP strengthened systems anchored with FRP splay anchors. It can also be concluded that CFRP splay anchors, if properly designed, could enhance the flexural capacity of RC beams by delaying the brittle debonding failure mode.

**Keywords: External Bonded Reinforcement (EBR); Carbon Fiber Reinforced Polymer (CFRP); RC beams; CFRP splay anchors; flexure.**

## Table of Contents

Abstract.....	6
List of Figures.....	10
List of Tables.....	13
Chapter 1. Introduction.....	14
1.1. Overview.....	14
1.2. Background.....	15
1.3. Flexural Strengthening.....	17
1.3.1. Externally bonded reinforcement (EBR).....	17
1.3.2. Near surface mounted (NSM) FRP reinforcement.....	17
1.4. Anchorage systems.....	18
1.4.1. Transverse wrapping (U-Wrapping).....	19
1.4.2. Mechanical anchorage.....	20
1.4.3. FRP spike anchors.....	21
1.4.4. FRP strips.....	22
1.5. Research Significance.....	23
1.6. Research Objectives.....	24
1.7. Thesis Framework.....	25
Chapter 2. Literature Review.....	26
2.1. Flexural Strengthening of Concrete Beams with FRP Laminates.....	26
2.2. Flexure Strengthening of RC Beams with CFRP Laminates and Anchors...30	
2.3. FRP Anchor Single Shear/Pullout Tests.....	36
2.4. American Concrete Institute Design Guidelines for Flexural Strengthening39	
2.5. Bond-slip Models.....	45
2.6. Forces in anchors.....	49
Chapter 3. Experimental Program.....	55
3.1. Specimen Details.....	55
3.2. Material Properties.....	57
3.2.1. Concrete.....	57
3.2.2. CFRP sheets and epoxy.....	59

3.2.3. CFRP anchors.....	62
3.3. Test Matrix.....	62
3.4. Test Setup.....	63
3.5. Specimen Preparation and Strengthening.....	65
3.5.1. Concrete prism preparation.....	65
3.5.2. Strengthening of prisms.....	65
Chapter 4. Experimental Results.....	70
4.1. Failure Modes.....	70
4.2. Load-deflection Responses.....	72
4.3. Ultimate Load, deflection, and maximum deflection.....	77
4.4. Strains in the CFRP.....	78
Chapter 5. Discussion of Results.....	84
5.1. Strengthening without anchors.....	84
5.2. Strengthening with anchors.....	84
5.2.1. Effect of anchor dowel diameter.....	88
5.2.2. Effect of anchor embedment depth.....	90
5.2.3. Effect of anchor dowel angle.....	91
Chapter 6. Bond-slip Models Results.....	94
6.1. Bond stress and slip models of control group.....	99
6.2. Bond stress and slip models of anchor dowel diameter group.....	101
6.3. Bond stress and slip models of anchor embedment depth group.....	103
6.4. Bond stress and slip models of anchor dowel angle group.....	106
Chapter 7. Summary and Conclusion.....	110
7.1 Summary.....	110
7.2 Conclusion.....	110
7.3 Suggested future work.....	112
References.....	114
Appendix.....	124
Sample Calculations - Bond-slip models.....	124



Vita..... 128

## List of Figures

Figure 1: Flexural strengthening of an RC beam [9].	17
Figure 2: Near Surface Mounted FRP reinforcement [23].	18
Figure 3: Debonding Failure Modes [45].	19
Figure 4: Transverse wrapping of longitudinal laminates [46].	20
Figure 5: Mechanical anchorage system [8].	20
Figure 6: Straight and bent FRP anchors [50].	22
Figure 7: 90° and 180° anchor spikes [46].	22
Figure 8: FRP strip anchorage [46].	23
Figure 9: Failure load based on width ratio [59].	26
Figure 10: CFRP sheet orientation [60].	28
Figure 11: Load-deflection plots for typical strip and anchor rupture tests [57].	32
Figure 12: Failure modes: (a) CFRP strip fracture; (b) CFRP anchor rupture; (c) Concrete beam shear failure; (d) Delamination between the CFRP strip and anchor fan [66].	33
Figure 13: Components used in ABAQUS model [67].	34
Figure 14: Test setup of: (a) flexural test (b) single shear pull-out test [69].	37
Figure 15: Processes of IC debonding failure [69].	38
Figure 16: FE model of FRP debonding for: (a) beam test; (b) single-shear pullout test [69].	39
Figure 17: Elastic strain and stress distribution of a rectangular beam [23].	44
Figure 18: Bond stress-slip model stages [74].	46
Figure 19: Specimen Details: (a) Prism Side View; (b) Prism Bottom View.	55
Figure 20: Strengthening and anchor detailing of prisms with: (a) FRP laminate; (b)FRP laminate and anchors.	56
Figure 21: Bottom view of strengthened specimens with: (a) FRP laminate; (b) FRP laminate and anchors.	56
Figure 22: Anchor parameters: (a) bottom view, (b) side view.	57
Figure 23: Concrete crushing setup.	58
Figure 24: Typical failure of :(a) concrete cubes; (b) concrete cylinders.	59
Figure 25: Tested flat CFRP coupons.	60
Figure 26: Tensile test machine.	61
Figure 27. Stress-strain curves of CFRP laminates of the tested coupons.	61

Figure 28: Test Setup .....	64
Figure 29: Strain gauge locations for prisms strengthened with: (a) CFRP laminates; (b) CFRP laminates and anchors.....	64
Figure 30: Prism preparation. ....	66
Figure 31: Sample of prepared CFRP sheet and anchor. ....	66
Figure 32: Strengthening procedure.....	69
Figure 33:After strengthening: (a) dry prisms; (b) dry prisms with strain gauges. ....	69
Figure 34: Load-Midspan deflection curves for the control group.....	73
Figure 35: Load-Midspan deflection curves for the anchor diameter group. ....	74
Figure 36: Load-Midspan deflection curves for the embedment depth group.....	75
Figure 37: Load-Midspan deflection curves for dowel angle group.....	75
Figure 38: Load-deflection curves of control group-3trials.....	76
Figure 39: Load-deflection curves of anchor dowel diameter group-3 trails. ....	76
Figure 40: Load-deflection curves of anchor embedment depth group- 3 trails.....	76
Figure 41:Load-deflection curves of anchor dowel angle group- 3 trails.....	77
Figure 42:Location of strain gauges for strain values.....	78
Figure 43: Strain versus distance plot of control group: (a) unanchored prism; (b) anchored control prism. ....	79
Figure 44: Load versus distance plot of dowel diameter group.....	80
Figure 45: Strain versus plot of embedment depth group.....	81
Figure 46: Strain versus distance plot of anchor dowel angle group.....	82
Figure 47: Percentage increase in terms of ultimate load capacity compared to unstrengthened prisms: (a)Anchor dowel angle group; (b) Anchor embedment depth group; (c) Anchor dowel angle group. ....	86
Figure 48: Typical load deflection response.....	87
Figure 49:Percentage increase in capacity of anchor dowel diameter group with respect to unanchored prisms (N-L1). ....	89
Figure 50: Normalized test results of anchor diameter group.....	89
Figure 51: Percentage increase in capacity of anchor embedment depth group with respect to unanchored prisms (N-L1). ....	91
Figure 52: Normalized test results of anchor embedment depth group. ....	91
Figure 53:schematic drawing for each anchor dowel angle.....	92

Figure 54: Percentage increase in capacity of anchor dowel angle group with respect to unanchored prisms (N-L1).....93

Figure 55: Normalized test results of anchor dowel angle group. ....93

Figure 56: Strain gauges used for bond stress and slip models: (a)unanchored prism; (b)anchored prism. ....97

Figure 57:Normalized maximum bond stress values for different anchor parameters. ....98

Figure 58:Normalized maximum slip values for different anchor parameters. ....98

Figure 59: Percentage increase of  $\tau_{max}$  compared to N-L1 .....99

Figure 60: Percentage increase of  $S_{max}$  compared to N-L1.....99

Figure 61: Bond stress-slip models of control group at different load levels..... 100

Figure 62: Bond stress vs. distance of control group at different load levels..... 101

Figure 63: Slip vs. distance of control group at different load levels..... 101

Figure 64: Bond stress vs. slip of anchor dowel angle group at different load levels. .... 102

Figure 65: Bond stress vs. distance of anchor dowel angle group at different load levels. .... 103

Figure 66: Slip vs. distance of anchor dowel angle group at different load levels... 103

Figure 67: Bond stress vs. slip of anchor embedment depth group at different load levels. .... 104

Figure 68: Slip vs. distance of anchor embedment depth group at different load levels. .... 105

Figure 69: Slip vs. distance of anchor embedment depth group at different load levels. .... 106

Figure 70: Bond stress vs. slip of anchor dowel angle group at different load levels. .... 107

Figure 71: Bond stress vs. slip of anchor dowel angle at different load levels..... 108

Figure 72: Slip vs. distance for anchor dowel angle at different load levels. .... 109

## List of Tables

Table 1: Original and factored cube compressive strengths. ....	58
Table 2: Compressive strength values of tested cylinders. ....	58
Table 3: FRP Sheets and Epoxy Properties. ....	60
Table 4: Mechanical properties of FRP laminates. ....	61
Table 5: FRP Anchors Properties. ....	62
Table 6: Test matrix of control specimens. ....	63
Table 7: Anchor Material Ratio of different anchor diameter – Method 1. ....	68
Table 8: Anchor Material Ratio of different anchor diameter – Method 2. ....	68
Table 9: Types of failure mode for each prism designation. ....	70
Table 10: Test results in terms of ultimate load, ultimate deflection, and maximum deflection. ....	77
Table 11: Normalized ultimate strain values. ....	83
Table 12: Normalized ultimate load values. ....	85
Table 13: Maximum bond stress and slip values. ....	97
Table 14: Sample Calculations - Strain values of N-AL1-155. ....	124

## Chapter 1. Introduction

### 1.1. Overview

Using fiber reinforced polymers (FRP) to strengthen and retrofit existing reinforced concrete (RC) structures has gained wide acceptance in the last decades. The advantages of FRP, compared to traditional strengthening techniques, includes high strength to weight ratio, ease of installment, durability, and versatility. FRP sheets could be applied onto the concrete surface in various forms to enhance the capacity of beams, columns, slabs, and walls. This technology extends the useful lives of concrete structures and helps in reducing maintenance costs in the future years. FRP laminates are formed by bonding FRP sheets to the concrete surfaces via epoxy adhesives by the wet-layup process. The laminates are usually applied manually by qualified and trained staff with certain equipment such as squeegees and aluminum rollers in such a manner that helps in releasing entrapped air bubbles when forming the laminate, hence densifying the FRP structure[1]–[15].

The conventional FRPs consist of a polymer matrix embedded with high strength fibers such as carbon (CFRP), glass (GFRP), basalt (BFRP), aramid (AFRP), and high-strength steel (HSS). These FRP materials provide an enhancement to structures in terms of ductility, axial capacity, flexural capacity, shear capacity, durability, increase of fatigue life (especially in bridges), and stiffness (reduce in deflections) [14],[15]. However, the main disadvantage of this strengthening system is the premature debonding of the FRP laminates prior to utilizing FRP tensile strength. Typically, FRP laminates debond from the concrete substrate at low FRP strain levels, leading to a brittle failure mode which is generally observed in FRP strengthened FRP systems.[9]. Such response limits the load-carrying capacity of the strengthened members due to inefficient utilization of the FRP material (i.e., debonding of the laminates before attaining the fracture strength of the FRP material).

Debonding mainly occurs due to increased stresses between FRP and concrete. The elevated stress levels promote the formation of cracks at the interface which propagate and eventually induce detaching of FRP laminates from the concrete surface. The debonding process is usually triggered by flexural and/ or flexural-shear cracks in the maximum moment region of the structure. These cracks start to open widely and then

develop high shear stress levels at the interface between the FRP and concrete substrate [15], [17]–[20]. Another form of debonding brittle failure is called delamination, where the FRP laminates detach from the concrete surface with the concrete cover adhering to it. Delamination occurs by the formation of cracks close to the end of the FRP laminate due to high stress concentrations at that point. The crack then propagates causing separation of concrete cover. Debonding and delamination are unfavorable failure modes that should be prevented in favor of FRP rupture, concrete crushing, and/or steel yielding [12], [15].

Studies have shown that debonding can be prevented by anchoring the FRP laminates to the concrete. Through proper anchoring, the debonding failure is delayed, thus providing higher levels of fiber utilization. In addition, anchoring could be feasible in the case of presence of geometrical obstructions that disrupt the continuity of the FRP stress field. There are many anchorage systems that have been developed so far, out of which FRP spike anchors have displayed many desirable advantages. The main advantage of FRP anchors, as opposed to other anchorage systems, is the compatibility of FRP anchors with the FRP laminates as they are made of the same material. In addition, FRP anchors could be implemented to suit a wide range of applications, as in beams (in flexure and shear), columns, slabs, and joints. Furthermore, FRP anchors have proven to be advantageous in preventing the early debonding of the FRP laminates, thus resulting in improved structural ductility, strength, and deformability [18], [19].

## **1.2. Background**

As previously mentioned, FRP has many advantageous and superior properties that make it an effective material for strengthening and repairing concrete structures. The typical densities of FRP range from  $1.2 \text{ g/cm}^3$  to  $2.1 \text{ g/cm}^3$  which is 4-6 times larger than that of steel. The mechanical properties of FRP may be reduced after getting exposed to certain environmental factors like high temperatures, chemical exposure, and humidity. Moreover, the decrease in mechanical properties could be influenced by duration of the exposure, type and formulation of resin, type of fiber, and resin curing method. The tensile properties reported by the manufacturer do not usually include the effect of the environmental exposure. The compressive strength of FRP composites is drastically lower than its tensile strength by about 20%-50%, so they cannot be used as

compression reinforcements [23]. FRP composites exhibit a linear elastic behavior with lower elastic modulus compared to steel. In addition, these materials are brittle in nature and break at low strain levels. The elastic modulus in general does not get affected by environmental conditions. The elastic modulus of FRP is calculated by Hooke's law by dividing the tensile strength of FRP by the rupture strain [20].

The conventional FRP composites (CFRP, BFRP, GFRP and AFRP) are brittle in nature, and thus cause brittle member failure when used in strengthening applications. In general, CFRP has higher tensile strength and elastic modulus than GFRP and BFRP, but relatively lower elongation at fracture. New FRP composites which are made of polyethylene naphthalate (PEN), polyethylene terephthalate (PET) and polyacetal (PAF) fibers, possess a nonlinear stress-strain behavior and fails at large rupture strains. The new FRPs are being mainly used in column confinement applications where ductility is required [24]–[26]. Besides FRP, high strength Aluminum Alloys (AA) were also used for flexural and shear strengthening by many authors, and they resulted in promising results from experiments and finite element analysis. Aluminum Alloys were capable of enhancing the ultimate load capacity and bond strength and were susceptible to premature debonding. Also, they have high ductility and desirable features that conquers some of the shortcomings of FRP [27]–[31]. FRP composites include high tensile fibers that are embedded in epoxy matrix. To achieve successful interaction between the strengthening FRP material and concrete, the surface of concrete must be well prepared before FRP installation. The quality of the FRP-to-concrete bond plays a major role in transferring stress between the concrete substrate and the FRP composite. The quality and reliability of the bond also depend on the material properties of epoxy matrix and the properties of concrete substrates, such as concrete compressive strength and roughness and cleanliness of the concrete surface. Epoxy resin is mostly selected for the strengthening procedure due to its excellent adhesive ability to both FRP and concrete. In some water or alkalis environments, epoxy adhesives may react with the surrounding environment, and thus affect the durability and mechanical properties of the FRP laminates. This could lead to the separation of the FRP material from the concrete substrate. In addition, it may cause reduction in the FRP laminates strength causing fatigue deterioration when the member is subjected to loads [32]–[37].



### 1.3. Flexural Strengthening

Strengthening of concrete beams using FRP materials significantly enhances the flexural capacity of the beams. The enhancement in capacity varies depending on the type of the strengthening material. According to Ashour et al. [38], CFRP provides the highest enhancement in the load-carrying capacity of the beams compared to other FRP types. However, specimens strengthened with CFRP possess the lowest ductility. The common failure mode of the specimens tested in [38] is the concrete cover peeling along with the CFRP sheets.

There are two common and effective strengthening techniques to strengthen RC beams in flexure using FRP materials. These include applying externally bonded reinforcement (EBR) to the concrete surface or inserting near-surface mounted (NSM) FRP rods in the tension side of the beam [39]–[41].

#### 1.3.1 Externally bonded reinforcement (EBR)

To enhance the flexural capacity of RC members, the externally bonded FRP laminates are attached to the tension face of the concrete member using epoxy adhesives. The fibers are oriented along the longitudinal axis of the beam as shown in Figure 1 [9]. The primary failure mode of EBR systems is the debonding of the FRP laminate from the concrete substrate. Debonding is a critical issue when designing FRP strengthened members, and it often limits the ultimate load carrying capacity [39], [40], [42].

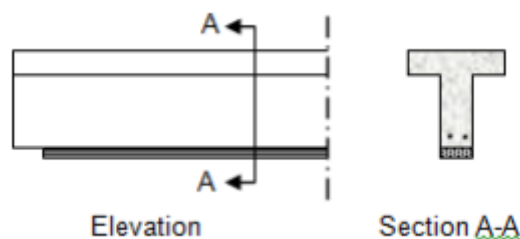


Figure 1: Flexural strengthening of an RC beam [9].

#### 1.3.2 Near surface mounted (NSM) FRP reinforcement

The NSM methodology is a contemporary technique in which an FRP bar or strip is inserted in a previously cut groove as shown in Figure 2. A groove filler consisting of epoxy or cement grout is used to bond the FRP to improve the bond performance. Advantages of NSM technique include protecting the FRP against external actions. In addition, it is suitable for strengthening regions where negative moments occur or

where minimal changes in the aesthetics of the structural element are required [39]. Furthermore, it is less prone to premature debonding failure when compared to EBR method, and it increases the resistance to fire damage, mechanical damage, aging effects, and vandalism acts. Moreover, this technique provides better durability, fatigue performance, and stress-sharing mechanisms. NSM has many other advantages; the amount of installation at site is reduced since surface preparation is not required. Furthermore, it is easily anchored into adjacent members which prevents debonding failures. These features are attractive in beams strengthened in flexure. However, this strengthening technique requires more concrete cover space, and cutting the grooves could accidentally damage the internal steel bars [30]–[33].

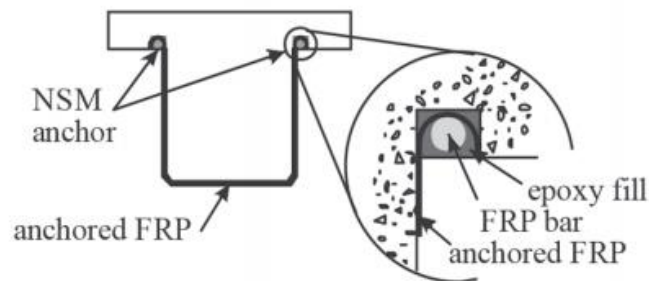


Figure 2: Near Surface Mounted FRP reinforcement [23].

#### 1.4. Anchorage Systems

Developing anchorage systems for externally bonded FRP laminates has been the interest of many recent research studies. These anchorage systems aid in enhancing the strength and deformability of strengthened concrete structures and provide load transfer mechanism after debonding. Therefore, this results in the development of the FRP strength. Anchorage systems used to anchor externally bonded FRP are used to satisfy the following purposes: (1) delay or prevent interfacial crack opening; (2) increase the total interfacial shear stress transfer available; and (3) provide stress transfer mechanism between the FRP and concrete [45]. Anchorage systems are used to prevent debonding failure modes including concrete cover separation, intermediate flexural crack-induced interfacial debonding, plate-end interfacial debonding, intermediate flexural shear crack induced interfacial debonding, and FRP debonding in shear strengthening. These debonding failures are illustrated in Figure 3 [45].

There are many types of anchorage systems that are being used to anchor FRP sheets to RC members. These include FRP spike anchors, transverse U-wrapping, U-anchors, FRP strips, and mechanically fastened anchors. In general, the anchors could be made up of FRP material or steel (used in mechanical anchors). The following subsections explain the different types of anchors used in flexural strengthening applications.

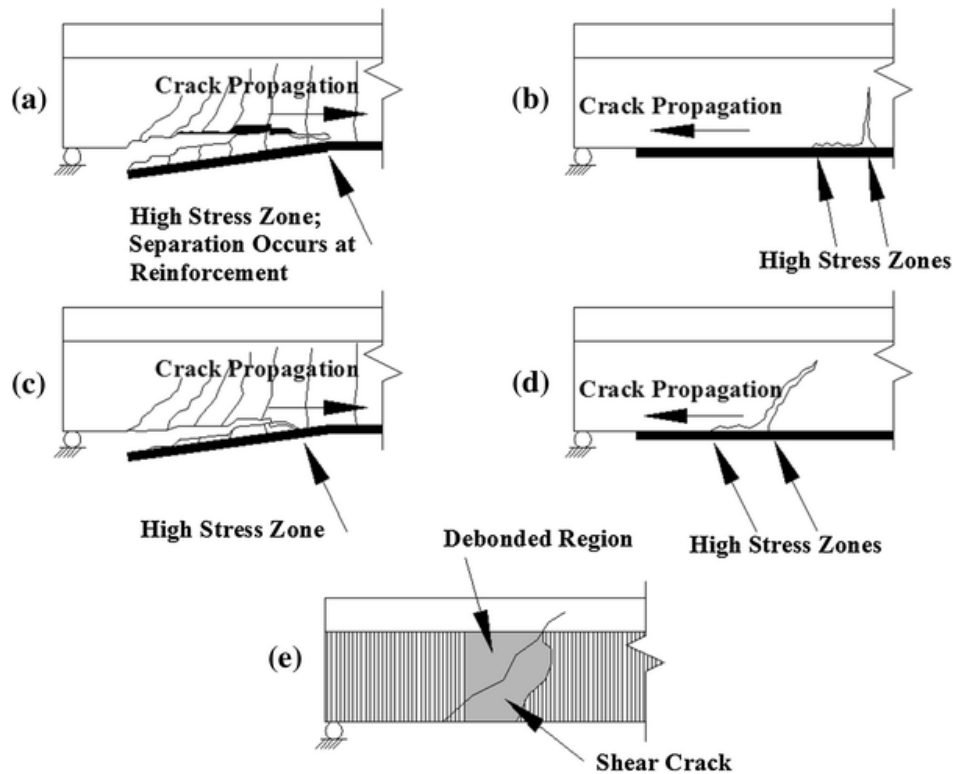


Figure 3: Debonding Failure Modes [45].

#### 1.4.1 Transverse wrapping (U-Wrapping)

Transverse wrapping consists of discrete FRP strips that are placed continuously along the length or at the end of the laminate as shown in Figure 4. The strips are usually made of the same FRP material as the laminates. Hence, this type of anchorage is noncorrosive, and it ensures durability to the structure. The orientation of the fibers is usually perpendicular to the longitudinal axis of the member or inclined at angle. Transverse wrapping is considered effective when a certain level of stress is maintained in the wrap, which results in generating a higher clamping force. This type of anchorage provides the necessary confinement to resist the tensile peeling stresses and the propagation of the longitudinal cracks at the termination points or intermediate cracks of the fiber. In addition, the U-wraps prevent or delay cracking on the onset of debonding and improve the interfacial shear transfer. Adding FRP U-wraps could also

change the debonding failure modes; for example, the critical debonding failure mode could be shifted from concrete cover separation to Intermediate Crack (IC) debonding [21]-[46]. IC debonding initiates a flexural-shear crack in the shear span and extends toward the FRP end in the direction of decreasing moment, and high local interfacial stresses are formed between the FRP and concrete [47], [48]. The installation of the U-wraps could be challenging in some cases due to geometrical obstructions, as it is required to place the wraps adjacently along the structure [21]-[46].

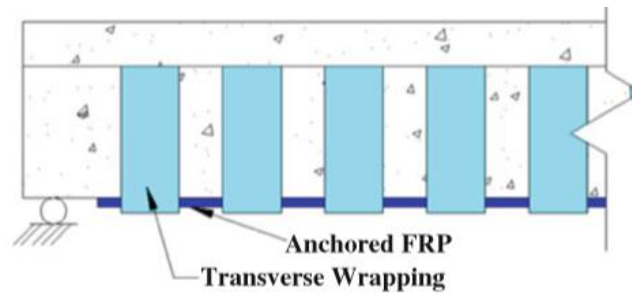


Figure 4: Transverse wrapping of longitudinal laminates [46].

#### 1.4.2 Mechanical anchorage

Mechanical anchorage involves metallic components such as steel bolts, angles or anchor rods used to anchor the FRP into the concrete. Figure 5 shows how longitudinal FRP laminates are anchored by using steel plates that are fastened with mechanical fasteners. Studies have shown that mechanical anchorage prevents premature debonding and considerably enhance the strength, stiffness, and ductility of the strengthened beam specimens. However, this anchorage system is unfavorable as it is susceptible to corrosion and hence it is not durable [49].

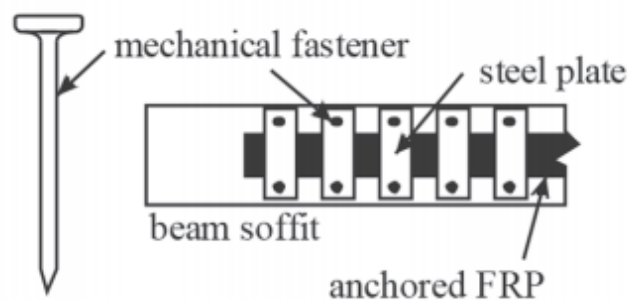


Figure 5: Mechanical anchorage system [8].

### **1.4.3 FRP spike anchors**

FRP anchors are made up of a bundle of fibers that are formed from a sheet of rolled FRP or from a bundle. One end of the anchor is splayed or spread out like a fan shape and the other is embedded in the concrete substrate. The splayed part of the anchors, known as the fan or splay component, is bonded to the FRP sheet to distribute the stresses while the embedded part, known as the dowel component, is inserted in a pre-drilled hole with epoxy resin. The transition segment between the fan to the dowel is referred to as the key portion [50]. FRP splay anchors have shown promising results in terms of enhancing the capacity and ductility of strengthened concrete members. There are numerous advantages of FRP splay anchors when compared to other anchorage systems. FRP anchors are more compatible with the FRP laminates since they are made of the same material. In addition, the anchors can be designed and fabricated in different ways to suit wide range of structural applications like shear/flexural strengthening, and slab to column joints. Moreover, FRP anchors have high strength to weight ratios and are noncorrosive [51]–[53].

Many studies have been conducted to study the impact of the FRP anchor configuration on the flexural strength capacity [40]–[43]. These configurations include geometrical parameters such as: 1) embedment depth ( $h_{emb}$ ) that refers to the depth of the embedded part of the anchors; 2) anchor diameter ( $d_a$ ) which is the dowel diameter; and 3) dowel angle ( $\beta$ ) which is the angle of the dowel embedded in the concrete, as shown in Figure 6. FRP anchors could be inserted straight into the structure (straight anchors) or at an angle (bent anchors). FRP anchor inclination angle has a great impact on the load-carrying capacity and ductility of strengthened beams[50], [58]. Straight anchors are only subjected to tensile stresses while bent anchors are subjected to tensile and shear stresses. Therefore, straight anchors are more effective and have higher capacity than bent anchors. However, in cases where straight anchors cannot be inserted, due to presence of internal steel or due to geometrical limitations for example, bent anchors with high dowel angles could be used instead[50].

#### ***1.4.3.1. 90° anchor spikes***

90° anchor spikes are fabricated in such a manner that the dowel is inserted in a hole drilled at 90° angle to the plane of the FRP in the concrete. The remaining fibers are fanned out on the face of the FRP sheet and integrated into the FRP matrix [46].

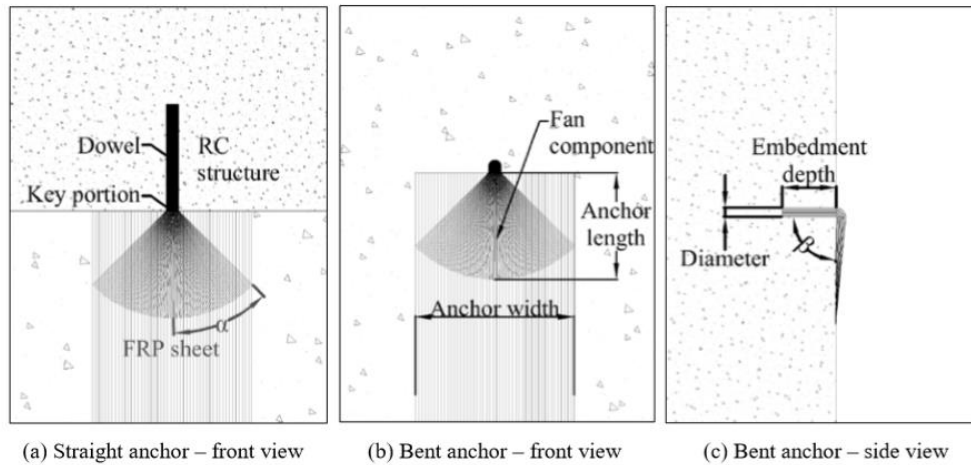


Figure 6: Straight and bent FRP anchors [50].

#### 1.4.3.2. 180° anchor spikes

180° anchor spikes are installed in-line with the FRP laminates allowing the fibers to transfer the tensile forces in the anchored FRP laminates to the anchor embedment. Both 90° and 180° anchor spikes have similar fabrication methods but different installation procedure and FRP strengthening application. The 180° anchor spikes are usually used to anchor FRP laminates in geometrically complex concrete members; this causes discontinuity in the FRP sheet. On the other hand, 90° anchor spikes are mostly used to anchor FRP sheets or plates throughout their lengths. Differences in the geometry shapes of 180° and 90° anchor spikes are shown in Figure 7 [46].

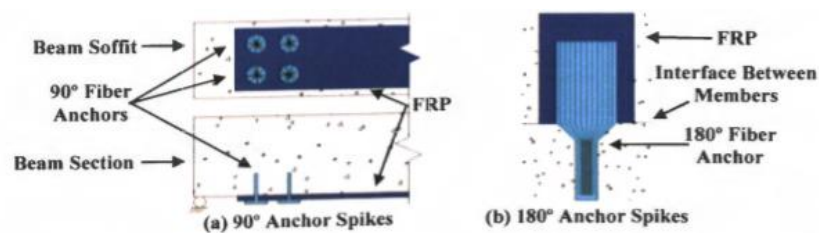


Figure 7: 90° and 180° anchor spikes [46].

#### 1.4.4 FRP strips

Fiber-reinforced polymer strips constitute a simple form of anchorage which is installed on top of the FRP sheet perpendicular to the direction of force in the FRP. In this type of anchor, fabrication is minimized because the laminates and the anchors are made of the same material. In some cases, FRP strips are not efficient to be used especially when

the geometry of the beam does not allow the right angle between the strip and strengthening sheet of the RC beam. FRP strips are usually loaded in a direction orthogonal to the strip fibers since they do not have the clamping effect like that of the transverse wrapping anchors [46]. Figure 8 shows an example of FRP strip anchorage system.

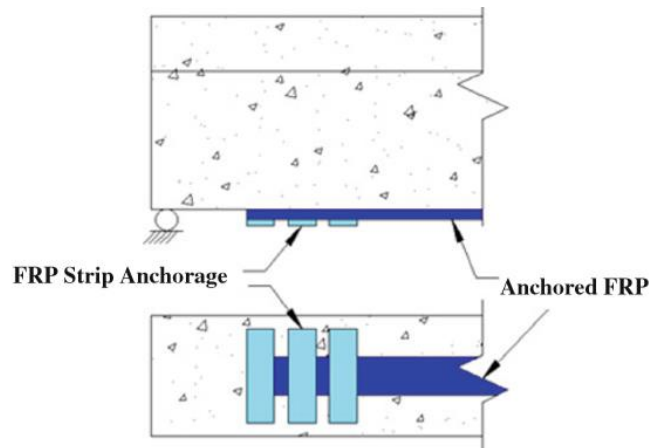


Figure 8: FRP strip anchorage [46].

### 1.5. Research Significance

Many RC structures have deteriorated over the decades due to increased loading caused by functional changes in the usage of the structures and corrosion of steel inside the concrete. The traditional retrofitting ways such as section enlargement and adding steel plates increase the lives of concrete structures; however, these techniques may result in negative consequences, such as increasing the structural load and corrosion of the steel plates. Strengthening of RC structures via applying externally bonded FRP reinforcement has proven to be advantageous in terms of enhancing the capacity, economical value (as the retrofitted structures require less maintenance), and durability.

Despite its benefits, strengthening of RC structures using FRP materials has a major disadvantage, i.e., the premature debonding of the laminates prior to utilizing FRP ultimate strength which results in a brittle member failure. To overcome this problem, researchers came up with different solutions, out of which anchoring the FRP laminates gave the most promising results. There are many effective anchorage systems discussed in the literature and are being implemented in the field. From the different anchorage systems available, FRP spike anchors have proven to enhance the strength and deformability of strengthened RC members. Moreover, the addition of FRP anchors

results in higher utilization of FRP tensile strength. However, the anchorage system is limited by the lack of design guidelines in the current codes of practice which hinders its implementation in real-life projects. Many studies addressed flexural strengthening using FRP laminates; however, fewer studies investigated the effect of some anchor parameters on the capacity and bond-slip response. Hence, more research is required to address wider range of anchor parameters. For the aforementioned reasons, the purpose of this study is to investigate the effect of anchoring CFRP laminates with different CFRP splay anchor parameters on the capacity of the structure, strain utilization of laminate, and bond stress-slip relationships. The performance of 33 normal weight concrete prisms was examined. The specimens include control unstrengthened and unanchored strengthened prisms in addition to strengthened prisms with CFRP laminates anchored with different CFRP anchor configurations. The parameters investigated are anchor diameter, embedment depth, and dowel angle. Also, bond-slip models are established to examine the effect of each studied anchor parameter on the bond stress and slip along the laminate.

#### **1.6. Research Objectives**

This research aims to study the overall performance of concrete prisms strengthened in flexure with CFRP laminates with different configurations of CFRP splay anchors. The main objectives of this research are:

1. Conduct bending tests on strengthened and unstrengthened concrete prisms to investigate the effect of strengthening small scale concrete beams in flexure with CFRP laminates and anchors.
2. Compare the load-deflection response curves and bond performance of CFRP strengthened, and anchored specimens with that of the control unstrengthened and unanchored specimens.
3. Study the strain in the CFRP laminates and compare the maximum attained strain in the laminates between anchored specimens and unanchored specimens.
4. Study the effect of the anchor dowel diameter, embedment depth, and dowel angle on the capacity of the strengthened and anchored concrete prisms.
5. Develop bond-slip models for the anchored and unanchored strengthened specimens to show the effect of each anchor parameter on the bond strength and load transfer mechanism.



## 1.7. Thesis Framework

The thesis is sectioned into eight chapters, organized as follows:

1. **Chapter 1: Introduction.** Introduces the topic and provides background on FRP flexural strengthening and anchorage systems. It also defines the objectives and research significance of this study.
2. **Chapter 2: Literature Review.** Presents some of the research published in areas related to the studied topic. Includes research topics about flexural strengthening with FRP laminates and anchors, FRP single shear pullout tests, ACI guidelines for flexural strengthening, Bond stress-slip models, and Forces in anchors.
3. **Chapter 3: Experimental Program.** Presents geometrical details related to the tested specimens, material properties, and preparation procedures. It also presents the test matrix, together with explaining the investigated parameters. In addition, the test setup and instrumentation were provided.
4. **Chapter 4: Experimental Results.** Presents the experimental results covering the failure modes, load-deflection response, ultimate loads and deflections, and strains in CFRP.
5. **Chapter 5: Discussion of Results.** Discusses the effect of strengthening with CFRP spike anchors with different anchor parameters.
6. **Chapter 6: Bond-slip models.** Bond-slip models are established to study the interface debonding and load transfer mechanism due to flexural cracking of concrete beams strengthened with anchored CFRP laminates and anchors.
7. **Chapter 7: Summary and Conclusion.** Summarizes the experimental results and concludes the outcomes of this study. Future work suggestions are also proposed.

## Chapter 2. Literature Review

### 2.1. Flexural Strengthening of Concrete Beams with FRP Laminates

Many tests were conducted to study the behavior of strengthened concrete structures with different types of FRP laminates. This section highlights some of the research done in this area.

Mazlan et al. [59] studied the behavior of concrete prisms strengthened by CFRP plates with various bond width ratios. The width ratio is the ratio of the FRP width to the concrete prism width. Four different ratios were tested under three-point bending test. A total of 15 concrete prisms of dimensions 75mm x 75mm x 350mm were prepared and tested, 12 were externally strengthened with CFRP, and the other three were set as control specimens. Four different widths were considered: 20, 40, 60, and 75 mm, all having length of 250 mm. Test results showed that that CFRP did not only provide load enhancement to the specimen, but also improved its ductility compared to the control specimens. Furthermore, increasing the CFRP width ratio, improved the ultimate load and stiffness of the CFRP strengthened specimens as shown in Figure 9 (a width ratio of 0.5 provided 80% enhancement in the capacity compared to the control specimen). It was also observed that as the width ratio increased, the failure mode changed from CFRP rupture to plate end interfacial debonding. The authors recommended providing an end anchor to anchor the CFRP plates in order to increase the ultimate load-carrying capacity and ductility of the strengthened specimens, and to avoid premature plate end debonding failure.

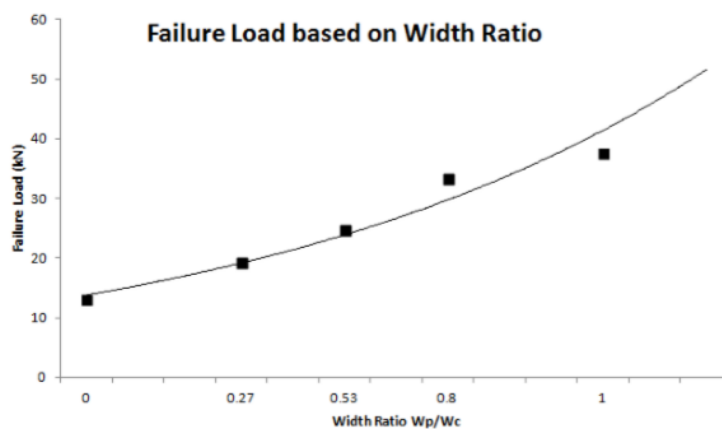


Figure 9: Failure load based on width ratio [59].

Murad [60] conducted an experimental study to investigate the influence of CFRP sheets on the overall performance of RC beams. The study focused on the effect of the CFRP sheet orientation angle on the strength and ductility of the RC beams. Different angles were examined ( $0^\circ$ ,  $45^\circ$ ,  $60^\circ$  and  $90^\circ$ ) as shown in Figure 10. The angles were measured with respect to the longitudinal axis of the beams. The experimental results showed that the flexural capacity was increased when CFRP laminates were bonded to the tension side of the beam. The highest strength was noted in the specimen strengthened with  $45^\circ$  inclined CFRP sheets compared to the control beam. However, flexural strength, ductility, and ultimate deflection decreased in beams strengthened with transverse and longitudinal CFRP sheets when compared to beams strengthened with inclined sheets. With respect to the ductility of the specimens, 8% of ductility reduction was observed for specimens strengthened with CFRP sheets inclined at  $45^\circ$  and  $60^\circ$  compared to the control beams; furthermore, 33% and 37% ductility reduction was attained with beams strengthened with longitudinal and transverse CFRP sheets, respectively.

It was observed that CFRP laminates delayed the appearance and propagation of cracks. In addition, the orientation of the laminates played a role in changing the crack pattern and failure mode. The typical failure mode of the specimens in Murad [60] study is the formation of flexural cracks, especially in specimens with horizontal and vertical orientation of CFRP sheets. For specimens with  $45^\circ$  and  $60^\circ$  inclined CFRP sheets, flexure-shear cracks occurred at ultimate capacity. The CFRP sheets in this case were perpendicular to the shear cracks, and thus resulted in enhancing the aggregate interlock and reduction in the shear cracks width. As a result, in the latter configuration, the occurrence of the initial cracks was postponed, which resulted in enhanced ductility. The deflection of specimens with  $45^\circ$  and  $60^\circ$  inclined CFRP sheets increased by 14% and 9 %, respectively. On the other hand, the ultimate deflection of specimens with transverse and longitudinal CFRP sheet decreased by 50 % and 34%, respectively. This study concluded that  $45^\circ$  inclined CFRP sheets was the best configuration among all other CFRP inclination angles.

A recent study by Hawileh et al. [14] investigated the effect of strengthening RC beams with side-bonded FRP sheets. The authors examined the effect of concrete compressive strength, FRP material type and size, and steel reinforcement ratio on the overall

performance of the specimens. Test results indicated that strengthened specimens had a higher load-carrying capacity and stiffness than the unstrengthened specimen; however, strengthening resulted in reduction in the ductility.

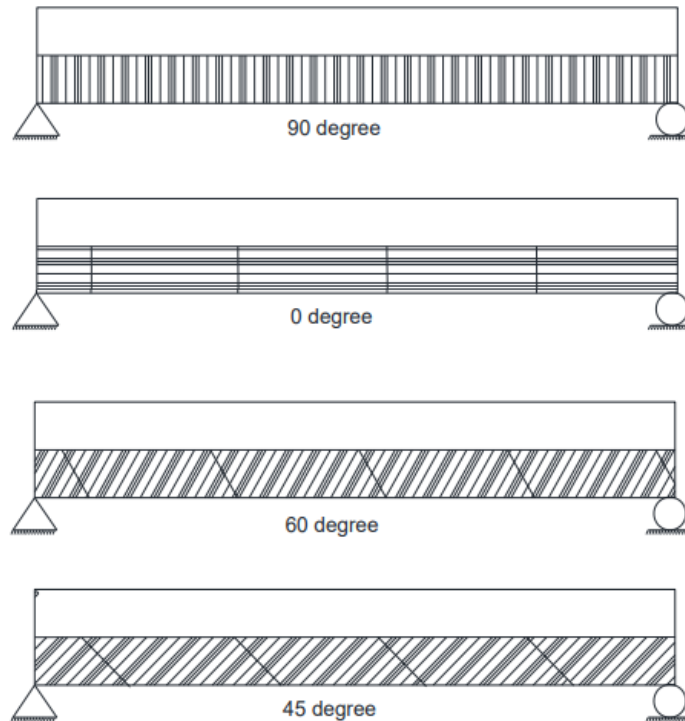


Figure 10: CFRP sheet orientation [60].

In addition, it was concluded that concrete compressive strength had a minor effect on the performance of the beams. The load-carrying capacity of the specimens with compressive strengths of 25, 35, and 47.2 MPa was enhanced by 33.8, 57.9, and 52.4% compared to the unstrengthened specimen, respectively. Furthermore, it was found that the width of the CFRP laminates was inversely proportional to the beam's load-carrying capacity. The FRP type also had a significant effect on the effectiveness of the strengthening system where CFRP achieved the highest enhancement in strength with 57.9% enhancement in capacity compared to the control specimen. Finally, numerical simulations were carried out using 3D finite element (FE) models on ANSYS software to verify the experimental results. The FE models generated curves simulated the flexural behavior of the RC beams strengthened with CFRP laminates. Particularly, the load-deflection responses, stiffness and failure modes were greatly captured by the FE models.

Other experiments investigated BFRP as strengthening material. Out of these is a study by Sim et al. [61] where they studied the applicability of BFRP sheets on concrete structures. BFRP laminates were applied at the beams' soffit to strengthen RC beams in flexure. The only parameter that varied between the specimens is the number of BFRP layers. The results showed that the yielding and ultimate strengths of the specimens increased as the number of BFRP layers increased. One layer of BFRP sheet increased the yield strength by 15% compared to the control beam but did not affect the ultimate strength. Using two layers of BFRP resulted in an increase in yielding strength and ultimate strength by 26% and 27%, respectively. Finally, when using 3 layers of BFRP sheets, the yielding strength was reduced compared to the two layers of BFRP, and the ultimate strength was improved by 29% compared to the control specimen. In addition, it was concluded that as the number of BFRP sheets increased, the post-yielding stiffness increased. Despite that, the specimen with 3 layers of BFRP failed by debonding which resulted in a drop in strength. Hence, it was concluded that using 2 BFRP sheets in flexural strengthening of RC specimens gave the optimum results.

Similarly, Duic et al. [62] conducted a study to determine the viability of BFRP composites for flexural strengthening and rehabilitation of RC beams. Seven full-scale RC beams were strengthened, and the flexural reinforcement ratio, corrosion level, number of layers of BFRP composite, and cross-strapping scheme were varied between the specimens. The authors found that BFRP composite is a suitable material for flexural strengthening and rehabilitation of RC beams. The best scheme in terms of providing higher strength and preventing premature debonding was via applying midspan and bottom span cross trapping. The application of BFRP was effective in improving the service load, yield load, and ultimate load capacity levels of uncorroded RC beams. The load-carrying capacity increased by 25% with three layers of BFRP laminates. Applying BFRP in the flexure side reduced crack widths at yield and service load; however, RC beams with higher reinforcement ratios developed more shear cracking than those with lower reinforcement ratios. The results also showed that the ductility was reduced due to strengthening with BFRP laminates. Different cross-strapping schemes gave different results. The midspan scheme of cross strapping allowed rupture to occur gradually while the bottom cross strapping scheme controlled the location of rupture allowing it to occur simultaneously for almost all fibers.

In addition to CFRP and BFRP, many studies investigated strengthening with GFRP laminates due to their desirable properties and relatively lower cost. Even though GFRPs have lower elastic modulus and tensile strength than CFRP, they have good deformability, break resistance and impact properties which makes them an appropriate material for strengthening. Almusallam [63] tested the durability of GFRP sheets by evaluating the flexural capacity under different environmental conditions which included the controlled laboratory, outside hot-dry field, wet-dry normal water, wet-dry saline (NaCl) water, and wet-dry alkaline (NaOH) environments. The RC beams were tested for 2 years, and results were taken after 6, 12, and 24 months of different environmental conditions. No degradation in strength and stiffness of the RC beam was observed. This shows that GFRP laminates are durable and effective in enhancing the capacity and ductility of RC beams

In another study by Attari et al. [64], the authors examined the efficiency of external strengthening of RC beams with unidirectional GFRP laminates. Four-point bending tests were conducted on the specimens until failure. The first loading phase corresponded to elastic behavior where no cracking appeared. In the second loading phase, cracking occurred and reduced the moment of inertia and bending stiffness consequently. Finally, the third loading phase included the yielding of the tensile longitudinal steel reinforcement while the external FRP sheet remained elastic. The test matrix included specimens with unanchored GFRP sheets and other specimens that are anchored with U-wrapped laminates. The strength gain in the GFRP strengthened specimens was 118% compared to that of the unstrengthened control specimen. Furthermore, the U-anchorage configuration improved the flexural strength due to redistribution of the internal forces, thus delayed debonding. GFRP was found to be a good alternative to the common CFRP in strengthening applications since it significantly increased the ductility and strength of the structure.

## **2.2. Flexure Strengthening of RC Beams with CFRP Laminates and Anchors**

Several studies investigated strengthening of RC beams with anchored CFRP laminates. Out of all anchors investigated, CFRP splay anchors proved efficient in allowing the laminates to attain their tensile capacity. This section highlights some of the research done in this area.

Ozdemir and Akyuz [65] conducted a study on CFRP anchors and investigated the effect of some variables on the tensile capacity of the anchors. The variables were the concrete compressive strength, anchorage depth, size of anchor hole, and width of CFRP sheet per anchor. The concrete compressive strengths tested were 10 MPa, 16 MPa, and 20 MPa. The diameters of the anchor holes were 12, 14, and 16 mm, and the three different sheet widths studied were 80, 120, and 160 mm. Four different embedment depths (50, 70, 100, and 150 mm) were also considered in this study. With respect to the embedment depth, the failure modes observed were shallow concrete cone failure for embedment depth of 50 mm, cone bend failure for embedment depth of 70 mm and more but not exceeding 100 mm, and rupture of CFRP sheet for a depth greater than 150 mm. The tensile capacity of CFRP anchor increased as the embedment depth increased from 70 mm to 100 mm. A decrease in the CFRP anchor capacity was observed when the embedment depth increased from 100 mm to 150 mm.

Moreover, test results showed that the concrete compressive strength did not affect the tensile capacity of the CFRP anchors with embedment depth less than 50 mm; however, the effect of the compressive strength became more significant as the embedment depth exceeded 50 mm. In addition, it was observed that the anchor hole diameter did not affect the tensile capacity of the CFRP anchor. Although the tensile capacity of the CFRP anchor increased with an increase in the amount CFRP materials, the increase was not proportional to the increase in the material. Furthermore, the effect of CFRP sheet width was also studied. Experimental results showed that the load capacity increased as the sheet width increased, but the behavior was not linearly proportional to the sheet width.

Sun et al. [57] tested 26 concrete beams of dimensions 152 mm x 152 mm x 610 mm with a 25.4 mm deep notch to ensure the flexural crack at midspan. The prisms were strengthened with CFRP sheets and anchored with two CFRP splay anchors (one on each side). The aim of the study was to investigate the influence of some parameters such as the width of the CFRP strip, the concrete strength, and the length/angle of the anchor fan on the flexural capacity of the prisms. In addition, the anchor material ratio (AMR) was studied. Since both the strip and anchor were made from the same CFRP material, the value of AMR is equal to  $w_{anchor} t_{f anchor} / w_{strip} t_{f strip}$  in which  $w$  and  $t$  are the widths and thicknesses of the CFRP strip and anchor, respectively. In general, the

results showed that the strip stresses increased by only 10% when high strength concrete was used compared to the normal weight concrete. In addition, it was observed that narrowing the CFRP strips resulted in higher average ultimate strip stresses at fracture. It was also found that anchors with larger cross-sections at a given load achieved more even strain distributions and lower maximum strains when compared to anchors with smaller cross-sections. The two major failure modes as shown in Figure 11 were CFRP strip fracture and anchor rupture. Anchor rupture occurred due to insufficient amount of CFRP material in anchors which led to anchor rupture before strips fracture.

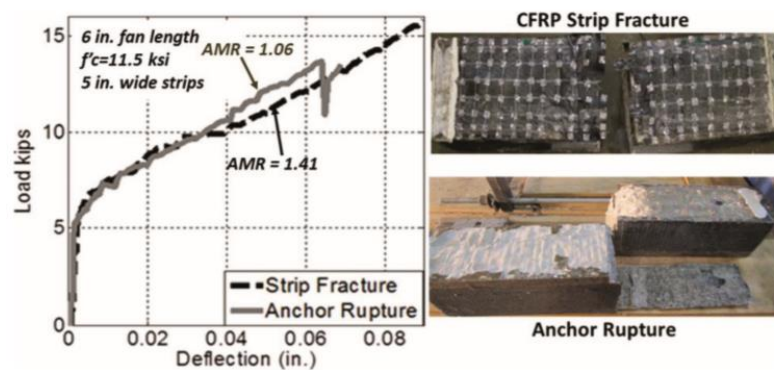


Figure 11: Load-deflection plots for typical strip and anchor rupture tests [57].

Test results also showed that increasing the fan angle from  $37^\circ$  to  $64^\circ$  did not show a significant change in stress at strip fracture. Test results showed that increasing the width of CFRP strips increased the local peak strains and decreased the average stress at fracture of the strip. However, the authors recommended the use of a fan angle between  $37^\circ$  and  $64^\circ$  to develop the tensile strength of the CFRP strip. It was also concluded that bonding CFRP strips to the concrete substrate improved the transfer of tensile forces from the CFRP strips to the CFRP anchors and prevented anchor rupture due to stress concentrations. Finally, CFRP anchors delayed the debonding of the CFRP strips under the loading conditions.

In a recent study by Sun [66], the author tested and evaluated the quality of CFRP anchors. The parameters investigated in this study were the ratio of the strength of CFRP anchor to the strength of the CFRP strip, CFRP strip width, concrete strength, fan angle, embedment depth, bend radius, hole diameter, CFRP patch, bond length, and the bond condition. CFRP anchors were inserted into a drilled hole through the CFRP sheet and concrete. Additional square CFRP patches were placed on the anchors with



an orientation perpendicular to the CFRP sheet to improve the transfer of force from the laminate to the anchor which would cause development of the strength of the laminate before anchor failure. To prevent shear failure of concrete, two U-wrap strips were bonded to the sides of the concrete prisms and oriented parallel to the tensile direction at the bottom. The U-wraps were not bonded to the CFRP laminate and were discontinued at the midspan to prevent its contribution to the flexural strength. Anchor holes were rounded at a specific bend radius to prevent the stress concentrations at the edges of the anchor hole, thus providing gradual transition of forces at the corners.

Three-point bending tests were conducted and four failure modes were observed: (1) CFRP laminate fracture; (2) anchor rupture at ultimate load; (3) concrete beam shear failure; and (4) delamination between the CFRP laminate and anchor fan. Figure 12 shows the failure modes of the prisms tested in [66].

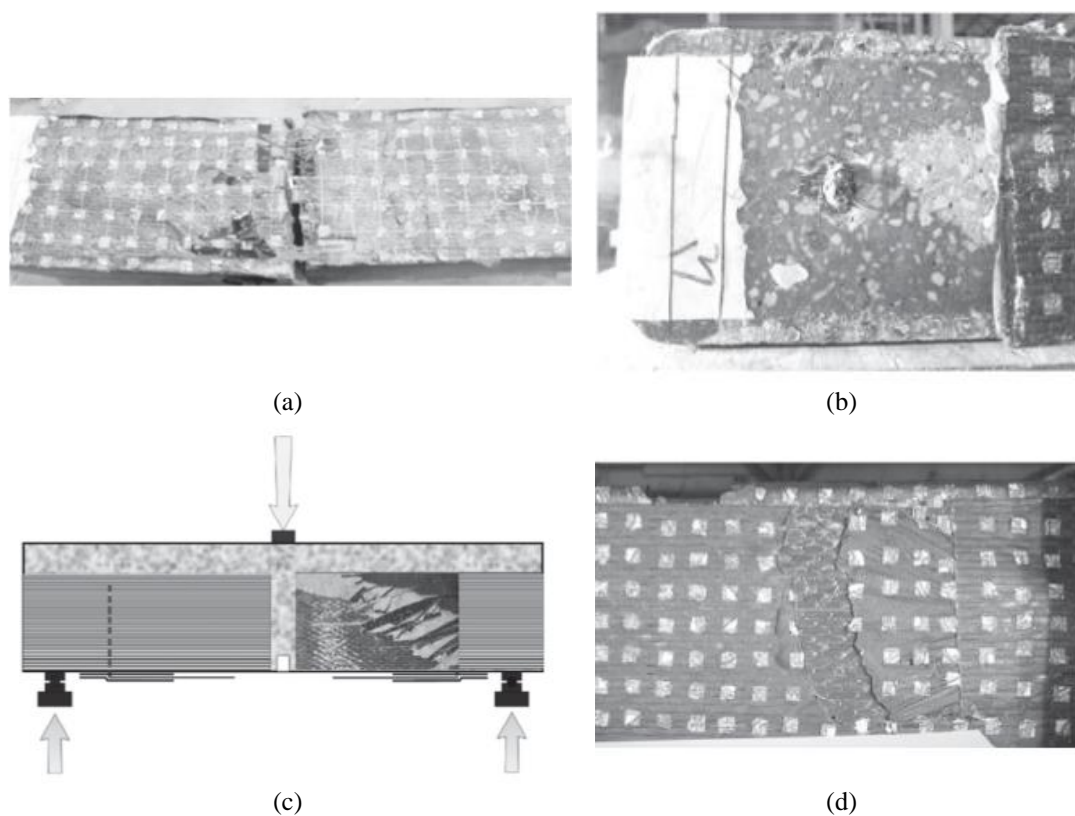


Figure 12: Failure modes: (a) CFRP strip fracture; (b) CFRP anchor rupture; (c) Concrete beam shear failure; (d) Delamination between the CFRP strip and anchor fan [66].

Test results showed that smaller fan angles allow gradual force transfer to the anchors. The author suggested the use of anchor fan angle less than  $45^\circ$  to maintain a reasonable and conservative anchor design and to develop the design strength of the CFRP

laminate. Furthermore, the bend radius of the anchors is also important to prevent stress concentrations at the edges of the anchor hole; therefore, the hole needed to be rounded to provide gradual transition of forces at the corners. The best test results were indicated in prisms with anchor bend radius of 13 mm. Moreover, the minimum recommended dimensions of CFRP patches are equal to the width of the CFRP laminate in both directions, and they should extend at least 38 mm away from the anchor hole. A bond length of 50 mm was able to fracture the CFRP laminate, so a 50 mm bond length was suggested to be applied in front of the anchor fan. Good bond condition is a necessity to ensure good performance of the anchorage system because it helps transfer the tensile stress from the CFRP laminate through the CFRP anchor into the concrete.

Al-Sammrai and Breña [67] developed finite element models using ABAQUS software to study the effect of different CFRP anchor parameters on the force development in FRP sheets. Experimental results of previously conducted single shear bond tests were used to validate the model after which a parametric study was conducted. The parametric study included several variables studied independently for anchors that include the number of anchors used in the sheet, the distance between anchors, anchor depth, anchor shaft diameter, anchor splay angle, and anchor splay diameter. The components of the FRP-anchored system modeled in ABAQUS is shown in Figure 13.

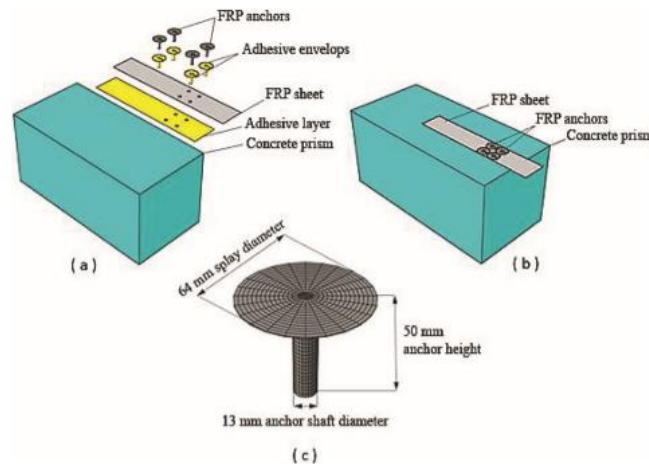


Figure 13: Components used in ABAQUS model [67].

Finite element analysis showed that cover separation of concrete was the main failure mode of the system. The cover separation started from the loaded end and propagated towards the back side of the CFRP sheet. This showed the importance of installing FRP

anchors at the loaded ends of the sheet where high tensile forces are present. Installing the anchors delayed the full separation until reaching higher load levels but did not prevent the propagation of debonding cracks behind the anchors [67].

Increasing the number of anchors resulted in a linear increase in system's tensile strength. However, after four anchors, the graph continues to increase but in a nonlinear manner. The sheet anchored with two anchors showed an increase of 60% in the tensile strength compared with the unanchored specimen. The tensile strength was increased by more than 100% when anchored with four anchors and more, indicating that the strength of the CFRP sheet was attained. With respect to the anchor splay diameter, the anchor splay covering the whole width of the CFRP sheet provided the maximum ultimate strength of the joint. Investigations of the effect of anchors' longitudinal spacing indicated that placing two anchors in a row with a long distance between the layers reduces the tensile strength and results in a comparable strength to placing two anchors as opposed to four. This is because the transfer zone area is reduced causing the transfer of the stress between the CFRP sheet and the underlying concrete to be reduced. Hence, it was concluded that anchors are more effective when placed in the stress transfer zone. Anchors placed far from the stress transfer zone may have a minor effect on the joint's strength.

The simulated models showed that anchor length is a key parameter that affects the FRP-concrete joint. Increasing the anchor length increases the tensile capacity of the anchors. In addition, long anchors prevent pull-out failures and the development of concrete-cone failure. FEM models also showed that reducing the CFRP anchor depth reduces the interface joint strength. It was observed that when the shaft depth is less than 30 mm, only 73% of the CFRP sheet strength was developed. On the other hand, when using a 50 mm shaft length, full strength of CFRP sheet was obtained. It was recommended not to use anchors with length less than 30 mm.

With respect to the effect of anchor shaft diameter, the FEM proved that increasing the diameter of the anchor shaft increases the strength of the joint since it increases the contact area between the shaft of the anchor and concrete hole. However, no enhancement was observed for anchor diameters exceeding 20 mm in diameter.

Finally, anchor splays are formed with radially oriented fibers either by forming a complete circle or a circular segment. The effect of the anchor splay geometry (fan angle) on joint strength was also observed. An exponential increase in the anchor capacity was noted when the fan angle increased from 0 to 90°. From 90° onwards, there was no increase in the capacity. In addition, anchors oriented in the direction of the tensile force showed the highest stress values.

### **2.3. FRP Anchor Single Shear/Pullout Tests**

Many research studies performed pullout experimental tests on FRP anchors to examine the different variables that affect the performance of the anchors. The parameters that affect the debonding behavior between the FRP and the concrete substrate in the

strengthening system include: (1) type of FRP used for anchors; (2) number of anchors; (3) anchor diameter; (4) embedment depth; (5) fan length and angle; (6) dowel angle; (7) distance between anchors; and (8) FRP type used in laminates.

Ozbakkaloglu and Saatcioglu [55] tested 81 CFRP anchors under monotonic axial loading to investigate the performance of CFRP anchors embedded in normal weight and high strength concrete specimens. The test parameters included the length, diameter, and angle of inclination of the anchors. Test results showed that the two different compressive strengths considered had a minor effect on the overall average bond strength of FRP material. Different failure modes were also observed. Most specimens failed by anchor pullout in the form of either concrete pull-out or combined cone-bond pull out. It was noted that the depth of the concrete cone decreased with increasing anchor embedment length. In addition, longer embedment depth increased the pullout capacity of the anchors. Likewise, the average pullout capacities of the anchors increased as the anchor diameter increased. On the other hand, the average bond strength of the FRP anchors decreased with increasing the anchor diameter and increasing the embedment depth. Finally, the pullout capacities of anchors decreased as the anchor angle of inclination increased.

In another study by Lim et al. [68], the authors examined the influence of the anchor size and fanning angle in bent FRP anchors. Twenty-four pullout tests were performed to understand the behavior of bent FRP anchors. The research focused on fiber rupture failure mode. Thus, dowel pullout failure mode was prevented by inserting the anchor

dowel into the RC base with sufficient depth. In addition, the fan-to-sheet debonding failure was prevented by introducing a large fan component. Results showed that acute FRP anchors performed better than obtuse ones. In addition, large anchors required larger loads to fail than smaller anchors but were less efficient. An equation was proposed in [68] to calculate the capacity of bent FRP anchors. However, this equation may not be reliable due to dispersion of results caused by the low reliability of FRP installation. The authors also recommended to keep the fanning angle in the range of 15 to 27 degrees.

Mohammadi et al. [69] studied the behavior of concrete beams strengthened in flexure with FRP laminates. The authors also performed single-shear pullout tests on strengthened specimens. Single shear tests were conducted to obtain the bond-slip behavior of the fiber reinforced polymer/concrete interface. Hence, the pullout specimens were designed to represent half the dimension of the beam specimen but with the same cross-section. The width of the FRP sheet was the same in all specimens. A half-depth saw-cut was located at the midspan of the beam specimens to trigger a pre-existing flexural crack. The condition of providing the same boundary condition for the beam tests and single-shear tests was satisfied by placing the single-shear pullout concrete specimens on a rigid frame with two steel reaction elements. The element relative to the notch of the bend test specimens (Element A in Figure 15) prevents the uncracked part near the top of the notch of the beam by providing horizontal reactions, while the element equivalent to the beam's support (Element B in Fig. 15) provides vertical reactions. Figure 14 presents the beam and single-shear pullout tests and the test setup.

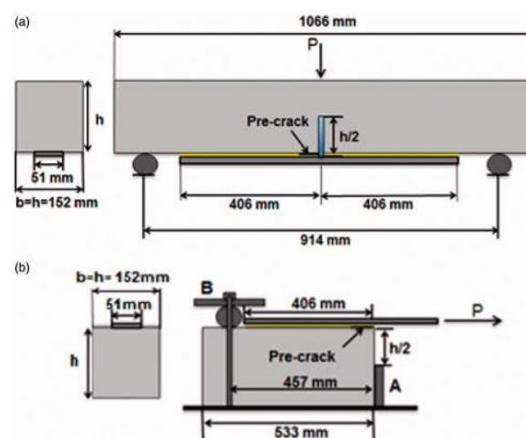


Figure 14: Test setup of: (a) flexural test (b) single shear pull-out test [69].

Beam bending tests were applied under displacement control mode, and results of the flexural loads and axial strains were recorded throughout the testing. In all bending tests, the process of (IC) debonding failure was as follows: first, flexural cracks were initiated at the top of the notch, then diagonal flexural/shear cracks appeared close to one or both sides of the notch. Then FRP debonding started along the interface of the FRP and concrete starting from the tip of the diagonal crack to the supports. Finally, sudden failures, such as diagonal cracks extending till the notch, cracks at the top of the notch extending to the point of loading, and full FRP debonding occurred. The failure process is shown in Figure 15. For single-shear pull-out tests, the applied load, FRP axial strain, and slip between the FRP and concrete at the tip of the diagonal crack were recorded. FRP debonding failure initiated at the tip of the pre-crack and extended to the end of the concrete [58].

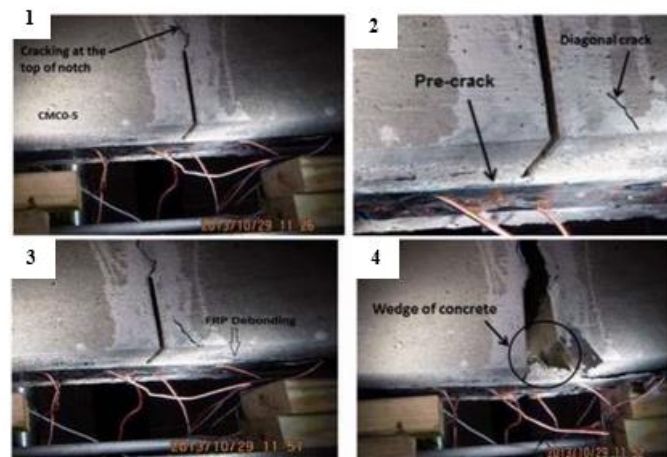


Figure 15: Processes of IC debonding failure [69].

Finite element models were simulated for both types of tests using ABAQUS software. In the beam test experiment, the debonding failure was not initiated at the tip of the applied pre-crack but at the tip of the diagonal crack without controlling at which side of the notch it will occur. To capture the diagonal crack behavior in the finite element analysis, a damage band was included along with the FRP. Furthermore, the cohesive method was applied to model the FRP/concrete interface which simulated the debonding behavior using bond-slip curve of the interface. The concrete was modelled using concrete damaged plasticity to maximize the principle stress for predicting the tension cracking in the concrete. Furthermore, the concrete plasticity model assumes that the crack starts when the maximum principle stress is equal to the tensile strength

of the concrete. The crack is usually perpendicular to the direction of the maximum principal stress.

According to the results of the FE model, the debonding in the single-shear specimens behaved in a similar manner to the experimental results, where the cracks started at the tip of the precrack and continued till the end through the FRP/concrete interface. The analysis was terminated due to an element at the top of the notch which resulted in a strain energy close to the critical fracture energy of concrete. Therefore, the element was no longer able to transfer stress. The debonding failures of both tests are shown in Figure 16. The FE model was also able to predict results similar to that of the experimental tests. In particular, the load versus deflection results of the FE model was compatible with the experimental results [69].

The experimental and numerical results showed that bond strength in beam specimens were smaller than those of the single-shear pullout specimens even though they had the same boundary conditions. Hence, it was concluded that the single-shear pullout tests cannot be used to analyze IC debonding failure in beams strengthened with FRP [69].

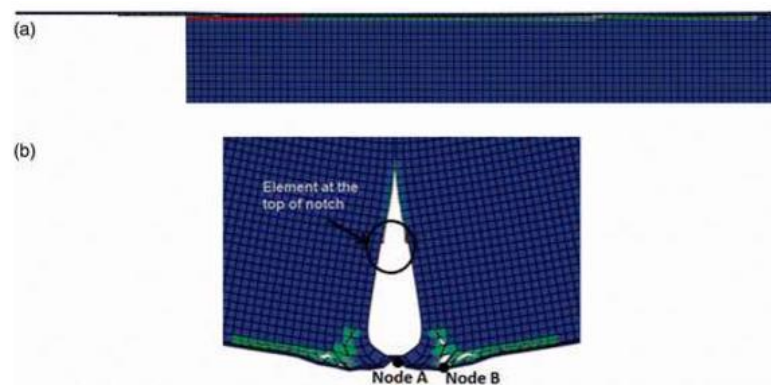


Figure 16: FE model of FRP debonding for: (a) beam test; (b) single-shear pullout test [69].

#### 2.4. American Concrete Institute Design Guidelines for Flexural Strengthening

Chapter 10 of the ACI 440.2R-17 [23] provides guidelines to design external reinforcement using FRP materials for flexural strengthened members. This section will present the detailed equations provided by the code. To enhance the flexural capacity, FRP laminates should be bonded to the tension face of concrete structures with the fibers oriented along the length of the member. The nominal flexural strength of the concrete structure should exceed the factored moment as indicated by Eq. 1.

$$\phi M_n \geq M_u \quad (1)$$

where:

$M_u$  = factored ultimate moment calculated by the ACI 318-19 code [70] (N-mm).

$\phi$  = strength reduction factor calculated by the following equation:

$$\phi = \begin{cases} 0.90 & \text{for } \varepsilon_t \geq 0.005 \\ 0.65 + \frac{0.25(\varepsilon_t - \varepsilon_{sy})}{0.005 - \varepsilon_{sy}} & \text{for } \varepsilon_{sy} < \varepsilon_t < 0.005 \\ 0.65 & \text{for } \varepsilon_t \leq \varepsilon_{sy} \end{cases} \quad (2)$$

$M_n$  = nominal strength of the member calculated by the following equation:

$$M_n = M_{ns} + \psi_f M_{nf} \quad (3)$$

where:

$\varepsilon_t$  = net tensile strain in extreme tension steel at nominal strength (mm/mm).

$\varepsilon_{sy}$  = steel yield strain (mm/mm).

$M_{ns}$  = steel contribution to bending calculated by the following equation:

$$M_{ns} = A_s f_s \left( d - \frac{\beta_1 c}{2} \right) \quad (4)$$

$M_{nf}$  = FRP contribution to bending calculated by the following equation:

$$M_{nf} = A_f f_{fe} \left( d_f - \frac{\beta_1 c}{2} \right) \quad (5)$$

$\psi_f$  = FRP strength reduction factor to improve the reliability of strength prediction and accounts for the different failure modes taken as 0.85.

$A_s$  = area of steel reinforcement (mm<sup>2</sup>)

$f_s$  = stress in tensile steel reinforcement (MPa), calculated by Eq. 10.

$d$  = effective depth of tensile steel reinforcement (mm).

$\beta_1$  = concrete stress block factor dependent on failure mode.

$c$  = depth of neutral axis (mm) (initially assumed) calculated by Eq. 12.

$A_f$  = area of FRP reinforcement =  $nt_f w_f$ .



$n$  = number of FRP layers.

$t_f$  = thickness of FRP sheet (mm).

$w_f$  = width of FRP sheet (mm).

$f_{fe}$  = effective stress in FRP reinforcement (MPa), calculated by Eq. 8.

$d_f$  = effective depth of the FRP reinforcement (mm).

The flexural capacity of the RC sections strengthened with EB-FRP reinforcement depends on the controlling failure mode. Several failure modes were observed in different studies. These include: (1) concrete crushing before steel yielding; (2) rupture of FRP laminate after steel yielding; (3) concrete crushing after yielding of steel; (4) shear/tension cover delamination; and (5) FRP debonding from the concrete substrate [23]. If the compressive strain in the concrete ( $\varepsilon_c$ ) reaches the maximum usable strain ( $\varepsilon_{cu} = 0.003$ ), concrete crushing is assumed to occur. Furthermore, the externally bonded FRP is assumed to rupture if the strain of the FRP ( $\varepsilon_f$ ) reaches its design rupture strain ( $\varepsilon_{fu}$ ) before the concrete reaches its maximum strain. FRP debonding and cover delamination occurs when the substrate cannot handle the force in the FRP. FRP debonding failure may govern when the bonded FRP terminates. To prevent such a failure, the effective strain of FRP reinforcement ( $\varepsilon_{fe}$ ) calculated by Eq. 6 is limited by the debonding strain ( $\varepsilon_{fd}$ ) as defined in Eq. 7.

$$\varepsilon_{fe} = \varepsilon_{cu} \left( \frac{d_f - c}{c} \right) - \varepsilon_{bi} \leq \varepsilon_{fd} \quad (6)$$

$$\varepsilon_{fd} = 0.41 \sqrt{\frac{f'_c}{nE_f t_f}} \leq 0.9\varepsilon_{fu} \quad (7)$$

where:

$f'_c$  = compressive strength of concrete (MPa).

$E_f$  = elastic modulus of FRP laminates (MPa).

$\varepsilon_{fu}$  = FRP rupture strain (mm/mm).

$\varepsilon_{bi}$  = initial strain in the substrate (mm/mm).

Anchorage systems such as U-wraps, mechanical fasteners, U-anchors, and fiber anchors delay and sometimes prevent debonding failure of the longitudinal FRP allowing the effective strain in the flexural FRP to reach the tensile rupture value. When calculating the flexural resistance of a strengthened section, some assumptions are made: (1) Design calculations are reliable on the internal steel reinforcement dimensions and the material properties of the strengthened member; (2) The strain values of the steel reinforcement and concrete are directly proportional to their distances from the neutral axis. So, a plane section before loading remains plane after loading; (3) No relative slip between the external FRP reinforcement and the concrete; (4) The adhesive layer is very thin with a very small thickness, so the shear deformation within this layer is neglected; (5) The maximum compressive strain in concrete is 0.003; (6) The tensile strength of concrete is neglected; and (7) The FRP is linearly elastic with a linear stress-strain relationship [23].

Some of these assumptions do not describe the reality of the fundamental behavior of FRP in flexure; however, this will not affect the computed flexural strength of the member. Since the FRP is linear elastic material, the maximum strain of the FRP will be governed by the strain developed in the FRP at concrete crushing or the strain at which FRP ruptures or the strain at which the FRP debonds from the concrete substrate. The stress strain compatibility on a strengthened beam is shown in Figure 17. The effective stress in the FRP ( $f_{fe}$ ) is the maximum level of stress developed by the FRP reinforcement before flexural failure and could be obtained by Eq. 8 from the strain in the FRP assuming a perfectly elastic behavior.

$$f_{fe} = E_f \varepsilon_{fe} \quad (8)$$

Based on the strain in the FRP, the strain in the steel reinforcement ( $\varepsilon_s$ ) is found by Eq.7 using strain compatibility. The stress in steel ( $f_s$ ) is then computed assuming elastic-perfectly plastic steel stress-strain curve using Eq. 9.

$$\varepsilon_s = (\varepsilon_{fe} + \varepsilon_{bi}) \left( \frac{d-c}{d_f-c} \right) \quad (9)$$

$$f_s = E_s \varepsilon_s \leq f_y \quad (10)$$

where:

$E_s$  = steel elastic modulus (MPa).

$f_y$  = steel yield stress (MPa).

The strain in concrete is calculated by similar triangles using the following equation:

$$\varepsilon_c = (\varepsilon_{fe} + \varepsilon_{bi}) \left( \frac{c}{d_f - c} \right) \quad (11)$$

With the stain and stress level in FRP and steel determined for an assumed neutral axis ( $c$ ), the internal force equilibrium should be checked by the following equation:

$$c = \frac{A_s f_s + A_f f_{fe}}{\alpha_1 f'_c \beta_1 b} \quad (12)$$

If concrete crushing governs and  $\varepsilon_{cu} \left( \frac{h-c}{c} \right) - \varepsilon_{bi} \leq \varepsilon_{fd}$  then:  $\alpha_1 = 0.85$  and  $\beta_1 = 0.85$  for  $f'_c$  value between 17 and 28 MPa. For  $f'_c \geq 28$  MPa, then  $\beta_1$  is reduced linearly by 0.05 for each 7 MPa compressive strength exceeding 28 MPa but shall not be taken less than 0.65.

If FRP rupture, cover delamination, or FRP debonding controls,  $\alpha_1$  and  $\beta_1$  should be calculated by the following equations:

$$\beta_1 = \frac{4\varepsilon'_c - \varepsilon_c}{6\varepsilon'_c - 2\varepsilon_c} \quad (13)$$

$$\alpha_1 = \frac{3\varepsilon'_c \varepsilon_c - \varepsilon_c^2}{3\beta_1 \varepsilon'^2_c} \quad (14)$$

$$\varepsilon'_c = \frac{1.7 f'_c}{E_c} \quad (15)$$

where:

$\varepsilon'_c$  = strain in concrete at compressive strength (mm/mm).

$E_c$  = concrete elastic modulus (MPa) calculated as  $4700\sqrt{f'_c}$ .

The serviceability of a member under service load should be also checked. Eqs. (16) – (18) provide the stress limits in the steel reinforcement, concrete and FRP. The distribution of strain and stress in a reinforced concrete section is shown in Figure 17.

$$f_{s,s} \leq 0.80 f_y \quad (16)$$

$$f_{c,s} \leq 0.60 f'_c \quad (17)$$

$$f_{f,s} \leq \begin{cases} 0.2 f_{fu} & \text{for GFRP} \\ 0.3 f_{fu} & \text{for AFRP} \\ 0.55 f_{fu} & \text{for CFRP} \end{cases} \quad (18)$$

where:

$f_{s,s}$  = stress in flexural steel reinforcement (MPa), calculated by the following equation:

$$f_{s,s} = \frac{[M_s + \varepsilon_{bi} A_f E_f (d_f - \frac{kd}{3})] (d - kd) E_s}{A_s E_s (d - \frac{kd}{3}) (d - kd) + A_f E_f (d_f - \frac{kd}{3}) (d_f - kd)} \quad (19)$$

$f_{c,s}$  = stress in concrete (MPa), calculated by the following equation:

$$f_{c,s} = \frac{M_s}{I_{cr}} n \quad (20)$$

$f_{f,s}$  = stress in FRP reinforcement (MPa).

$$f_{f,s} = f_{s,s} \left( \frac{E_f}{E_s} \right) \left( \frac{d_f - kd}{d - kd} \right) - \varepsilon_{bi} E_f \quad (21)$$

$f_{fu}$  = FRP rupture stress (MPa).

$M_s$  = moment at service load (N-mm).

$kd$  = depth of the neutral axis at service (mm). It is computed by taking the first moment of the areas of the transformed sections. The transformed area of the FRP is obtained by multiplying the area of the FRP by the modular ratio of FRP to concrete. The stress values are then compared to the limits.

$I_{cr}$  = moment of inertia of cracked section ( $\text{mm}^4$ ).

$n$  = concrete modular ratio which calculated by  $\frac{E_s}{E_c}$ .

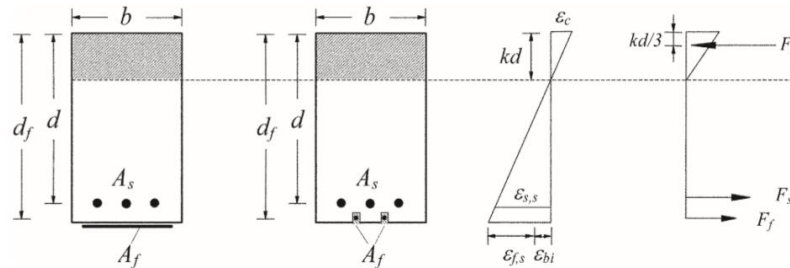


Figure 17: Elastic strain and stress distribution of a rectangular beam [23].

## 2.5. Bond-slip Models

To maintain an effective strengthening system for concrete structures, the stress distributions between the concrete substrate and FRP materials should be adequate to prevent failure modes caused by debonding of FRP from the concrete substrate. The behavior between the epoxy bonded FRP and the concrete substrate should be studied following approaches like empirical bond-strength models, bond-slip models, and analytical derivation of bond-slip models [71].

Bond failure controls the bearing capacity of beams strengthened in flexure and shear leading to debonding that usually occurs in the concrete substrate or along the FRP sheet. Interfacial shear stress between the FRP sheet and concrete substrate is calculated by obtaining strain values from consecutively strain gauges placed on the FRP sheets; the difference of these strain values is used to calculate the mean stress. The position of the strain gauges play an important role in giving the number of points where the shear stress could be obtained [72].

Typically, pullout tests represent the stress state of the interfacial part between the concrete substrate and FRP sheet when subjected to tension. Bond-slip curves are usually determined from strains obtained using strain gauges or from load-displacement curves. When using the strain gauges, the shear stress is calculated from the strain values obtained by using the distance formula leading to the slip calculations by numerically integrating the measured axial strains. The drawback of this method is that it might not give accurate bond-slip curves due to unexpected crack locations of concrete, so strain gauges may give inaccurate values when not placed on these cracks [73].

Nelson et al.[74] conducted bond tests on concrete specimens strengthened with FRP laminates where forces were applied at the end of the specimens. The force was transferred through the bond between the concrete substrate and the FRP laminate. The bond stress and strain are denoted by  $\tau$  and  $\epsilon$ , respectively. Figure 18(a) shows the relation between the bond and slip where the bond forces start from zero force in the laminate and increases linearly reaching point A which is the maximum force the laminate can provide. With continuous loading, points B and C are formed in the bond slip curve showing the initiation and propagation of microcracks along the interface leading to macrocracks. Moving to point D, the load carrying capacity does not increase

anymore transferring the interfacial stress from the bond length to the substrates. After point D, the FRP strain remains constant, and any applied load exceeding point E leads to sudden brittle failure due to FRP debonding from the concrete substrate.

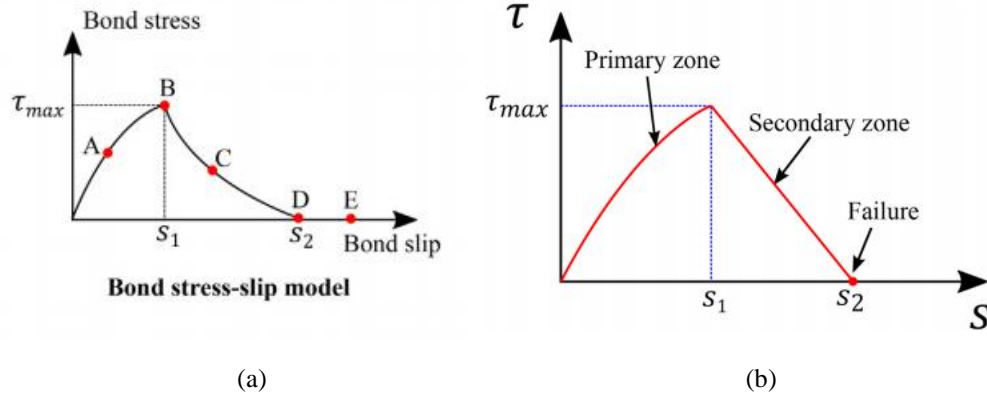


Figure 18: Bond stress-slip model stages [74].

According to the authors, the externally bonded FRP debonding process is divided into three stages (shown in Figure 18(b)): the primary zone, the secondary zone, and the failure stage. The first stage that occurs in the primary zone is when the bond stress increases to the maximum  $\tau_{max}$  and corresponds to  $s_0$  (which is the slip when reached to  $\tau_{max}$ ). The area within the zone before reaching the maximum bond stress is uncracked. The secondary zone includes interfacial softening and decrease in the bond stress reaching zero, and it corresponds to  $s_f$  which is the slip when  $\tau$  reaches zero; this leads to microcracks in the concrete. The effective length  $L_e$  is formed to accommodate both the primary and secondary stages to withstand the maximum axial load when reached.

Failure stage is the last stage which indicates that the ultimate slip is met and the debonding failure occurred. Complete debonding occurs when  $s_f$  exceeds the distance of  $L_e$  from the free end leading to sudden failure and therefore global debonding of FRP (over the full length of FRP).

Lu et al. [73] presented a review of existing bond-slip models and proposed new bond-slip models based on finite element methods. A numerical approach was developed to determine the bond-slip curve at different points along the interface between the FRP and concrete substrate. The stress state of the interface was represented by pull tests

where debonding was the primary failure mode. As a result, the authors suggested that stress and slip could be obtained along the interface if the concrete member is modelled accurately. According to the finite element models, it was concluded that bond-slip curves include ascending and descending branches, and when the slip is very large the bond stress decreases towards zero. As microcracks appear in the concrete, the stiffness decreases gradually causing the bond stress to increase. Moreover, the maximum bond stress ( $\tau_{max}$ ), the corresponding slip ( $s_0$ ) and concrete tensile strength ( $f_t$ ) are linearly related while the interfacial fracture energy ( $G_f$ ) increases almost linearly with  $\sqrt{f_t}$ . Bond-slip models were proposed which were linear and bilinear models.

The first approach that Lu et al. [73] developed was for the nonlinear bond-slip relationship that defined the ascending and descending portions of the curve precisely. The following equations are the bilinear models developed by Lu et al. [73]. :

$$\tau = \tau_{max} \sqrt{\frac{s}{s_0}} \quad \text{if } s \leq s_0 \quad (22)$$

$$\tau = \tau_{max} e^{-\alpha(\frac{s}{s_0}-1)} \quad \text{if } s > s_0 \quad (23)$$

The following equations were used in the bilinear model predictions:

$$\tau = \tau_{max} \frac{s}{s_0} \quad \text{if } s \leq s_0 \quad (24)$$

$$\tau = \tau_{max} \frac{s_f - s}{s_f - s_0} \quad \text{if } s_0 < s \leq s_f \quad (25)$$

$$\tau = 0 \quad \text{if } s > s_f \quad (26)$$

$$G_f = 0.308\beta_w^2 \sqrt{f_t} \quad (27)$$

where:

$\tau$  = local bond stress.

$s$  = local slip.

$G_f$  = interfacial fracture energy.

$\tau_{max}$  = maximum local bond stress, calculated by the following equation:

$$\tau_{max} = \alpha\beta_w f_t \quad (28)$$

$s_0$  = local slip at  $\tau_{max}$ , calculated by the following equation:

$$s_0 = 0.0195\beta_w f_t \quad (29)$$

$s_f$  = local slip when bond stress  $\tau$  reduces to zero, calculated by the following equation:

$$s_f = 2G_f/\tau_{max} \quad (30)$$

The maximum shear stress  $\tau_{max}$  and slip are governed by the concrete tensile stress and FRP width ratio factor that are denoted by  $f_t$  and  $\beta_w$ , respectively. The tensile stress  $f_t$  is given by the manufacturer while FRP width ratio factor  $\beta_w$  is calculated by the following equation:

$$\beta_w = \sqrt{\left(2.25 - \frac{b_f}{b_c}\right) / \left(1.25 + \frac{b_f}{b_c}\right)} \quad (31)$$

where:

$b_f$  = width of FRP.

$b_c$  = width of concrete.

In Eq. 32 the factor  $\alpha$  is related to the interfacial fracture energy  $G_f$  which is the energy per unit bond area required for full debonding of FRP and is calculated by the following equation:

$$\alpha = 1/[G_f/(\tau_{max}s_0) - 2/3] \quad (32)$$

The bond strength of FRP to concrete can be calculated in terms of interfacial fracture energy by the following equation:

$$P_u = \beta_l b_f \sqrt{2E_f t_f G_f} \quad (33)$$

where:

$\beta_l$  = bond length factor.

If  $L > L_e$ ,  $\beta_l = 1$  but if  $L < L_e$ ,  $\beta_l < 1$ ,  $\beta_l$  is calculated by the following Eqs.34 and 35. It was noted that both equations provide similar predictions.

$$\beta_l = \sin\left(\frac{\pi L}{2L_e}\right) \quad \text{if } L < L_e \quad (34)$$



$$\beta_l = \frac{L}{L_e} \left( 2 - \frac{L}{L_e} \right) \quad \text{if } L < L_e \quad (35)$$

The effective bond length which is the length that can carry most of the stresses on the FRP and is calculated by the following equations:

$$L_e = a + \frac{1}{2\lambda_1} \ln \frac{\lambda_1 + \lambda_2 \tan(\lambda_2 a)}{\lambda_1 - \lambda_2 \tan(\lambda_2 a)} \quad (36)$$

where:

$$\lambda_1 = \sqrt{\frac{\tau_{max}}{s_0 E_f t_f}} \quad (37)$$

$$\lambda_2 = \sqrt{\frac{\tau_{max}}{(s_f - s_0) E_f t_f}} \quad (38)$$

$$a = \frac{1}{\lambda_2} \arcsin \left[ 0.99 \sqrt{\frac{s_f - s_0}{s_f}} \right] \quad (39)$$

It was concluded that bond-slip models should consist of both ascending and descending branches. To be more precise, the bond-slip model should include curved ascending and descending branches, and bilinear models are considered as good approximations. In addition, the models should provide accurate predictions of fracture energy.

## 2.6 Forces in Anchors

Different design models were proposed in literature for different anchor failure modes to predict the force in straight and bent anchors. Failure modes were investigated by isolating each FRP anchor component to develop an anchor design methodology and designer-friendly equations that estimates the design capacity of the anchors. However, more studies should be implemented to develop these equations and ensure their accuracy for different structural types and applications. With respect to straight anchors, the predicted force ( $N_{pred}$ ) is calculated as the minimum anchor capacity of the three common failure modes including fiber rupture ( $N_{fr}$ ), concrete cone pullout ( $N_{cc}$ ), and concrete-cone and bond pullout ( $N_{cb}$ ). Equations used for these types of anchors could be also used for anchors with insertion angles close to  $180^\circ$  as recommended by Del Rey Castillo [75] ensuring conservative results.

In a recent study by Del Rey Castillo et al. [75], semi-empirical design models were developed to calculate FRP anchor capacity considering extensive data and different anchor parameters that have an effect on the failure mode . Equation 40 is used for straight anchors with fiber rupture failure mode and Eq.41 is used for bent anchors with 90° dowels. The literature still lacks design models to calculate the capacity of bent anchors with varying dowel angles; however, Eq.41 is applicable for the range of parameters provided.

Straight anchors - Fiber rupture failure mode:

$$N_{fr}^{95\%} = 3.1E_a\varepsilon_a 10^{-3}A_{dowel}^{0.62} \left(\frac{90-\alpha}{90}\right) \quad (40)$$

The range of parameters used to develop these models were:  $E_a = 253$  GPa,  $\varepsilon_a = 0.0098$ ,  $168 \text{ mm}^2 \geq A_{dowel} \geq 14 \text{ mm}^2$ , and  $60^\circ \geq \alpha \geq 15^\circ$ .

Bent anchors,  $\beta = 90^\circ$ : Fiber rupture failure mode:

$$N_{fr}^{95\%} = 2.3E_a\varepsilon_a 10^{-3}A_{dowel}^{0.62} \left(\frac{90-\alpha}{90}\right) \quad (41)$$

The range of parameters used to develop these models were:  $E_a = 253$  GPa,  $\varepsilon_a = 0.0098$ ,  $84 \text{ mm}^2 \geq A_{dowel} \geq 28 \text{ mm}^2$ ,  $60^\circ \geq \alpha \geq 15^\circ$ , and  $\beta = 90^\circ$ .

where:

$N_{fr}$  = anchor fiber rupture capacity (N).

$E_a$  = elastic modulus of the anchor (MPa).

$\varepsilon_a$  = rupture strain of the anchor (mm/mm).

$A_{dowel}$  = cross-sectional area of the anchor dowel ( $\text{mm}^2$ ).

$\alpha$  = half of the fanning angle ( $^\circ$ ).

Design models developed by Kim and Smith [56] were also presented by Del Rey Castillo considering concrete failure modes such as concrete-cone failure and combined concrete-cone and bond failure to calculate the pullout capacity of straight anchors. An extensive database was calibrated as models and is presented in Eqs.42-44.

Straight anchors-Concrete cone failure:

$$N_{cc}^{95\%} = 9.68h_{ef}^{1.5}\sqrt{f'_c} \quad (42)$$

Straight anchors-Combined concrete-cone and bond failure:

$$N_{cb}^{95\%} = 4.62\pi d_o h_{ef} (f'_c < 20 \text{ MPa}) \quad (43)$$

$$N_{cb}^{95\%} = 9.07\pi d_o h_{ef} (f'_c \geq 20 \text{ MPa}) \quad (44)$$

where:

$N_{cc}$  = anchor concrete-cone capacity (N).

$N_{cb}$  = anchor combined concrete-cone and bond capacity (N).

$h_{ef}$  = anchor embedment depth (mm).

$f'_c$  = concrete compressive strength (MPa).

$d_o$  = hole diameter (mm).

The range of test parameters used to develop these models were:  $100 \text{ mm} \geq h_{ef} \geq 17.5 \text{ mm}$ ,  $60 \text{ MPa} \geq f'_c \geq 10.4 \text{ MPa}$ , and  $11.8 \text{ mm} \geq d_o \geq 20 \text{ mm}$ .

Kobayashi [76] stated that the force transfer mechanism from the FRP sheet to the concrete substrate could be affected by fan splay of anchors. Further, installing the FRP sheet perpendicular to the load activates the full fan length by spreading the load along it, hence improves the capacity. Kanitkar et al. [77] conducted single-lap shear tests to study large diameter anchors (9.5 mm, 13 mm, and 16 mm) with different fan splay lengths (100 mm, 150 mm, and 200 mm) and fan angle of 30°. Based on the manufacturer's installation guidelines, FRP anchors were installed after placing the saturated FRP sheet on the concrete substrate. In some cases, anchors were installed after curing the FRP sheet. Moreover, anchor fans could be installed between two FRP sheets to improve the capacity of the structure. In different applications fan-to-FRP debonding failure could be dominant. Equation 45 could be used to predict the capacity of the anchors for this failure mode.

Fan-to-FRP fan debonding failure:

$$N_{sd} = 0.35V_{sb}A_{fan} \quad (45)$$

where:

$N_{sd}$  = anchor fan debonding capacity (N).

$V_{sb}$  = shear bond strength of epoxy resin (MPa); 5 MPa is recommended if unknown.

$A_{fan}$  = total surface area of fan sheet bonded to the laminates ( $\text{mm}^2$ ).

The range of test parameters used to develop this model were:  $100 \text{ mm} \geq fan \text{ length} \geq 215 \text{ mm}$ , maximum splay angle ( $\alpha$ ) =  $30^\circ$ , resulting in range of  $A_{fan}$ :  $6500 \text{ mm}^2 \leq A_{fan} \leq 21000 \text{ mm}^2$ ,  $V_{sb} = 14.5 \text{ MPa}$ .

Zhang and smith [78] presented an equation proposing a linear relationship between the anchor dowel angle ( $\beta$ ) and bonded surface. The angles ranging between  $45^\circ$  and  $135^\circ$  were recommended for Eq.46. However, equations of straight anchors could be used for larger angles between  $135^\circ$  and  $180^\circ$  since they are close to  $180^\circ$  anchors.

$$k_\beta = 2.34 \left( \frac{\beta}{2\pi} \right) - 0.33 \quad (46)$$

where:

$k_\beta$  = strength enhancement coefficient for bent anchors.

$\beta$  = insertion angle (radians).

Villanueva et. al [10] developed an analytical model to predict the capacity of anchors with different geometrical and installation parameters. The maximum strength of anchors was defined as the minimum value of three strengths representing three common failure mechanisms: adherent strength, bending-zone strength, and tensile strength. Concrete cone failure is one of the undesirable failures that usually occurs due to low dowel embedment depths, and the capacity for this failure mode is calculated using Eq.47. In some cases, this failure is combined with adherent failure where the depth of the concrete pullout cone increases when decreasing the dowel embedment depth. The authors considered this failure since it usually indicates that the structure is already damaged by the reinforcement, and hence it should be avoided. A minimum embedment depth of 50 mm is recommended for concrete strengths above 20 MPa; however, embedment depths greater than 40 mm were also suggested to transfer stress without taking place in the concrete cover region. Equation 48 was proposed to calculate the capacity of adherent or mixed failure which mainly depends on the bond shear stress, dowel diameter, and embedment depth. In reality, shear stress is non-uniform through the embedment depth of the anchors. As a result, Eq.48 considers the

average stress value, which is usually applied for small, embedded anchors. Since tensile and bending failures dominate the behavior of deep anchor, this equation was recommended for short, embedded dowels.

$$P_{cc} = 9.68 h_{emb}^{1.5} \sqrt{f'_c} \quad (47)$$

$$P_{cb} = \tau_{ave} \pi d_o h_{emb} \quad (48)$$

Where:

$P_{cc}$ : maximum capacity of FRP anchor for concrete cone failure mode (kN).

$P_{cb}$ : maximum capacity of FRP anchor in adherent of mixed failure mode (kN).

$\tau_{ave}$  : average shear strength (MPa).

$d_o$ : hole diameter (mm).

$h_{emb}$ : dowel embedment depth (mm).

With respect to the failure in bending region due to the FRP rupture at the key portion, an expression was developed taking into consideration the parameters affecting this type of failure including the embedment depth and dowel angle. Different studies proved that increasing embedment depths increases strength to a certain limit. Therefore, an effective embedment depth of anchors should be suggested for different structural member depths similar to that provided for the development length of structures with EBR systems. The proposed model considered an embedment depth of 150 mm to be sufficient in terms of stiffness and development depth where it provided enough bond capacities for anchors with dowel diameter between 10 and 13 mm. Moreover, the dowel insertion angle with the bend radius was also engaged in the model due to their effect on the bend strength of anchors. Zhang and Smith [78], and Ozbakaloglu and Saatciglu [79] concluded that obtuse angles getting closer to 180° (straight angles) results in higher capacities. So, based on these results, Eq.49 was developed for bend zone failure.

$$P_{bend} = \left[ 0.3 \left( \frac{h_{emb}}{150} \right) + 0.05 r_b \left( \frac{\alpha}{\left( \frac{\pi}{2} \right)} \right) \right] \cdot P_u \quad (49)$$

Where:

$P_{bend}$ : maximum bend capacity of FRP anchor (kN).

$\alpha$ : dowel angle of FRP anchors (degrees).

$r_b$ : bend ratio.

$P_u$ : tensile strength of FRP anchor (kN).

The third mechanism is the tensile capacity of anchors which could be determined using coupon tests. Anchors could be ready-made and supplied from the manufacturer with the diameter requested or handmade from bundle fibers or from FRP sheets. If anchors are formed by FRP sheets, Eq. 50 is used to calculate its tensile strength where diameter is irrelevant. Circular sections of anchors could be considered if the manufacturer provide FRP bundles with fixed fiber quantities. The tensile strength of composite is calculated for the matrix and used with the anchor diameter to define its tensile capacity as shown in Eq.51.

$$P_u = \gamma w_{FRP} t_{FRP} f_{FRP} \quad (50)$$

$$P_u = \pi \left( \frac{d_a}{2} \right)^2 f_{FRP} = A_a f_{FRP} \quad (51)$$

where:

$d_a$ : FRP anchor diameter (mm).

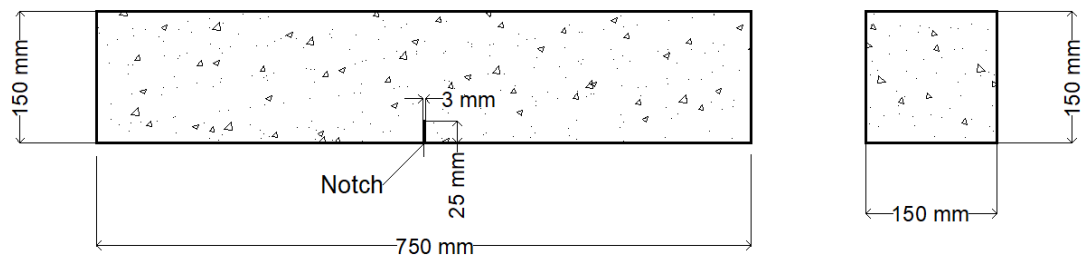
$f_{FRP}$ : Tensile strength of composite (MPa).

$A_a$ : cross-sectional area of FRP anchors (mm<sup>2</sup>).

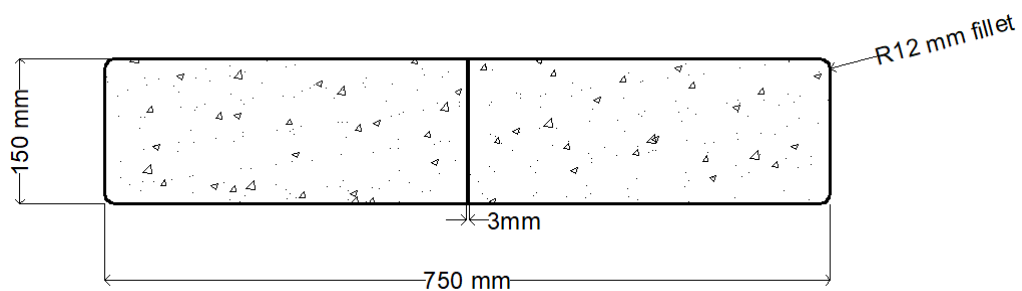
## Chapter 3. Experimental Program

### 3.1. Specimen Details

A total of 33 concrete prisms were cast and tested. The depth of the beams was 750 mm, with a cross-section of 150 mm x 150 mm as shown in Figure 19. It is worth noting that small-scale specimens were chosen because of their size and weight which allow them to be easily handled in the laboratory. To ensure flexural cracking at midspan, a notch of 3 mm width and 25 mm depth was grinded at the bottom midspan of the prisms as shown in Figure 19. The prisms were strengthened in flexure with CFRP sheets in the tension side (bottom of the prisms). The CFRP sheets were 100 mm in width and 550 mm in length and were bonded to the concrete at a distance 100 mm away from each end. In addition, two CFRP anchors were installed in predrilled holes at 125 mm away from each end of the concrete prism. The strengthened prism section details are shown in Figures. 20-22.

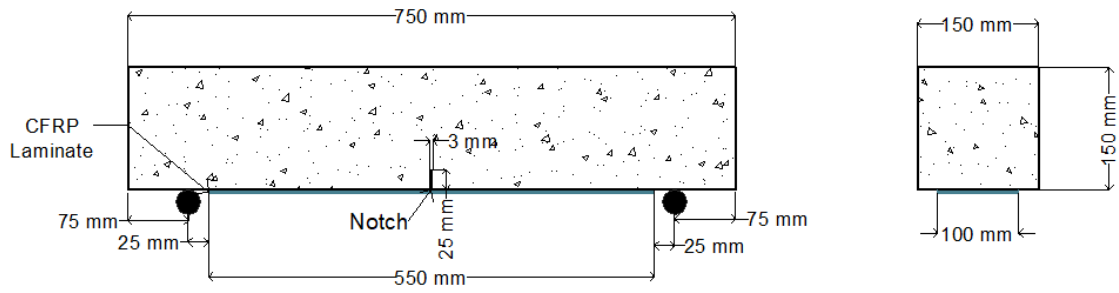


(a) Prism Side View

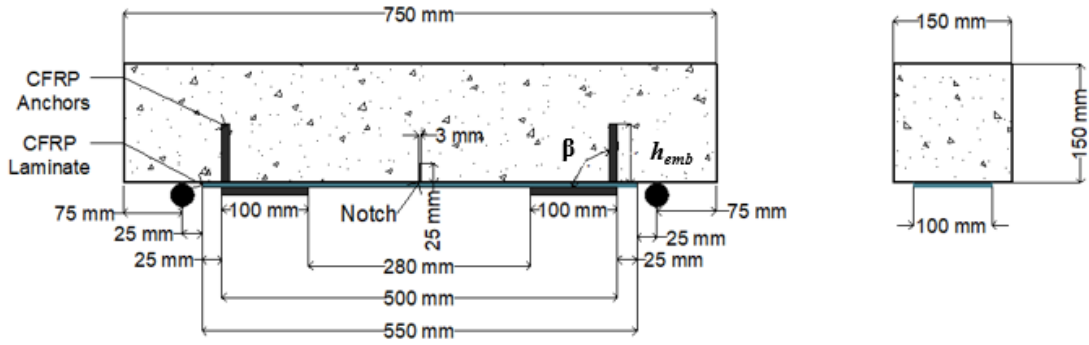


(b) Prism Bottom View

Figure 19: Specimen Details: (a) Prism Side View; (b) Prism Bottom View.

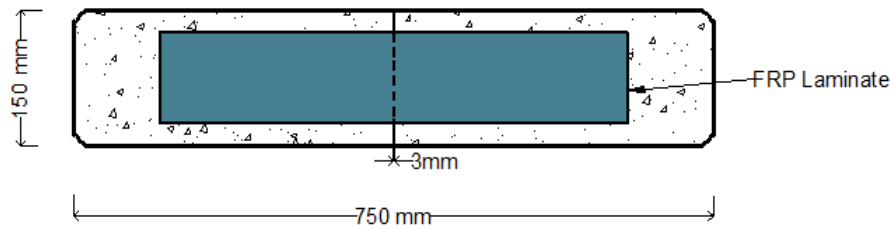


(a)

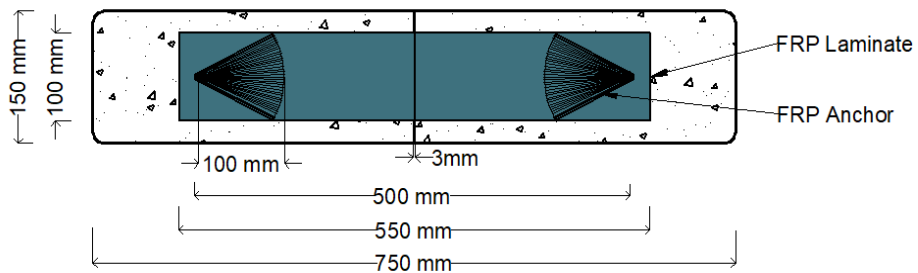


(b)

Figure 20: Strengthening and anchor detailing of prisms with: (a) FRP laminate; (b) FRP laminate and anchors.



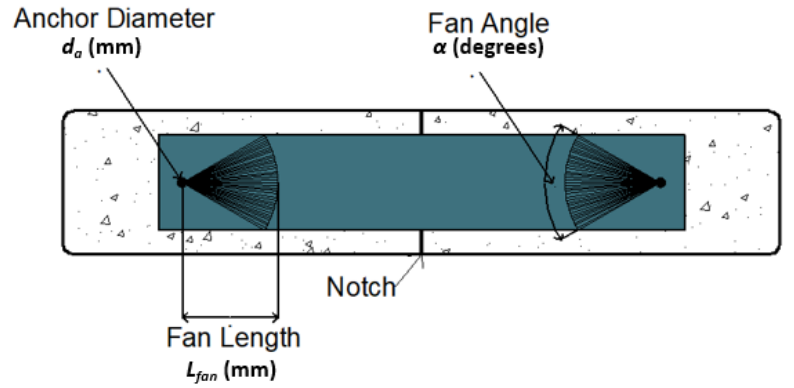
(a)



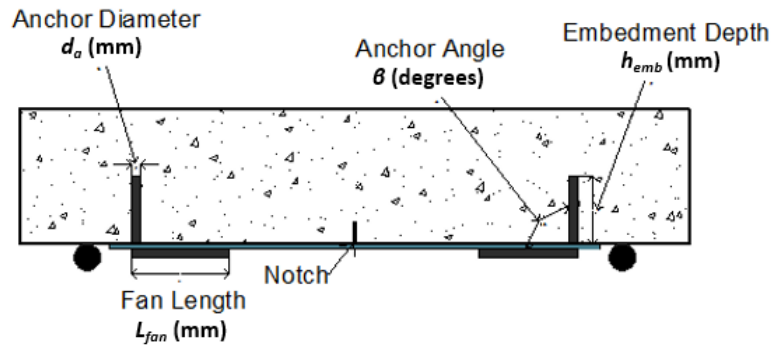
(b)

Figure 21: Bottom view of strengthened specimens with: (a) FRP laminate; (b) FRP laminate and anchors.





(a)



(b)

Figure 22: Anchor parameters: (a) bottom view, (b) side view.

### 3.2. Material Properties

#### 3.2.1. Concrete.

The beams were cast using normal weight concrete with a design compressive strength of 50 MPa. The concrete compressive strength for the prism was measured by crushing 3 cubes and 3 cylinders from each casted batch after 28 days of curing, using a compression-testing machine. Compressive strength tests were carried out in the Asphalt lab of the American University of Sharjah according to ASTM C109/C109M-16a [80] standards at a stress control rate of 0.25 MPa/sec, using the concrete crushing setup shown in Figure 23. The cubes and cylinders were centered at the middle of the machine under the loading cell; their typical failures are shown in Figure 24. Tested values of the cube compressive strength ( $f'_c$ ) were multiplied by a factor of 0.83 and compared to the obtained cylindrical tested compression values. In addition, the test results of the original and factored cube compressive strengths are presented in Table

1. The design requirement was met since the compressive strength values of the cubes and cylinders are close as shown in Table 2.

Table 1: Original and factored cube compressive strengths.

	Cubes $f_{cu}$ (MPa)			Cubes by factor $f'_c$ (MPa)		
	First Batch	Second Batch	Third Batch	First Batch	Second Batch	Third Batch
Trial 1	65	65.6	64.3	53.95	54.448	53.369
Trial 2	63.4	64.1	62.5	52.622	53.203	51.875
Trial 3	63.2	64.2	63.3	52.456	53.286	52.539
Average:				<b>53.01</b>	<b>53.65</b>	<b>52.59</b>

Table 2: Compressive strength values of tested cylinders.

	Cubes by factor $f'_c$ (MPa)			Cylinders $f'_c$ (MPa)		
	First Batch	Second Batch	Third Batch	First Batch	Second Batch	Third Batch
Trial 1	53.95	54.448	53.369	51.9	50.3	55.4
Trial 2	52.622	53.203	51.875	55.7	54.8	55.6
Trial 3	52.456	53.286	52.539	54.6	56.7	54.6
Average:	<b>53.01</b>	<b>53.65</b>	<b>52.59</b>	<b>54.07</b>	<b>53.93</b>	<b>55.20</b>



Figure 23: Concrete crushing setup.



(a)



(b)

Figure 24: Typical failure of : (a) concrete cubes; (b) concrete cylinders.

### 3.2.2. CFRP sheets and epoxy.

The CFRP sheets that were used consisted of high-strength unidirectional CFRP material. The dry and laminate (fiber + epoxy) properties of CFRP sheets and the mechanical properties of the primer [81] and epoxy resin [82] used for impregnation of the laminates and anchors, as provided by the manufacturer, are presented in Table 3. High-strength unidirectional CFRP composite [83] was used in this study. Three flat coupon specimens were prepared with a total length of 200 mm and a width of 15 mm using the wet layup process. The nominal thickness for the CFRP was 0.5 mm. ASTM standard D3039M-08 [84] was used for the conducted tensile tests on the flat coupons, shown in Figure 25, to evaluate the mechanical properties of the CFRP laminates using the tensile test machine in Figure 26. Two strain gauges were placed on each side at

the center of the specimens to record the strain response of the laminates. An average value between the two readings was reported, and tensile strength was calculated by dividing the tensile load by the product of the width and nominal thickness of the coupon specimens. Stress-strain response curves of the samples are illustrated in Figure 27. Moreover, Table 4 shows the average results in terms of elastic modulus ( $E$ ), tensile strength ( $f_u$ ), and ultimate strain ( $\epsilon_u$ ). The mechanical properties provided by the manufacturer are also tabulated for comparison purposes.

Table 3: FRP Sheets and Epoxy Properties.

Material	Material Industrial Name	Weight	Density	$t$ (mm)	$E$ (GPa)	$f_u$ (MPa)	$\epsilon$ (%)
CFRP Sheet	MAPEWRAP C UNI-AX 300	300 g/m <sup>2</sup>	1800 kg/m <sup>3</sup>	0.164	252	4900	2
CFRP laminate		-	-	0.5	83.848	1492	1.7
Primer	MapeWrap Primer 1	1.1 Kg/L	1.1 g/m <sup>3</sup>	-	-	-	-
Epoxy Resin	MapeWrap 31	1.06 Kg/L	A	-	2.6	40	1.6
			B				

$t$ : thickness;  $E$ : elastic modulus;  $f_u$ : tensile strength;  $\epsilon$ : rupture strain

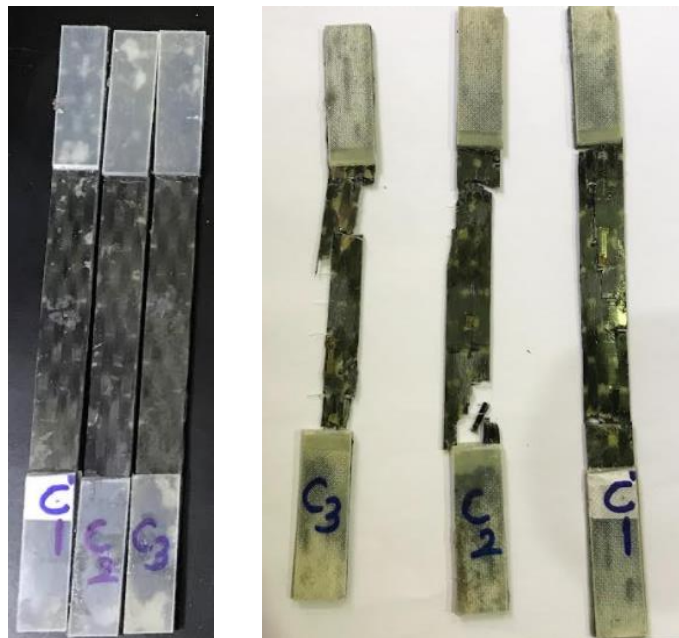


Figure 25: Tested flat CFRP coupons.



Figure 26: Tensile test machine.

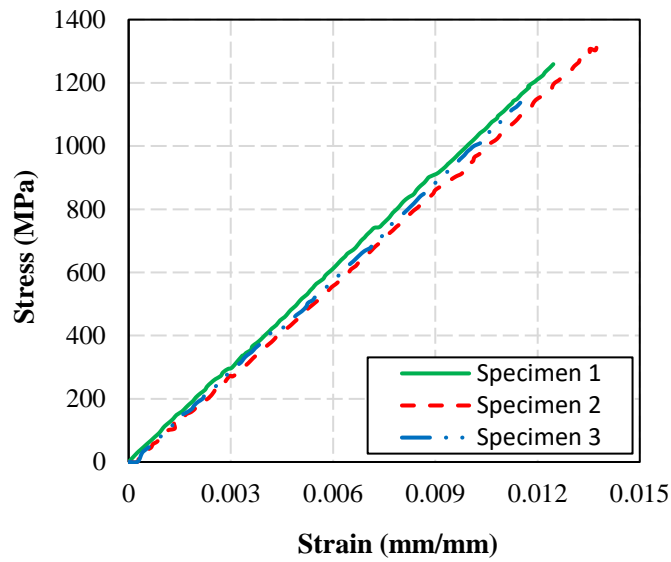


Figure 27. Stress-strain curves of CFRP laminates of the tested coupons.

Table 4: Mechanical properties of FRP laminates.

Material	Elastic Modulus (GPa)			Tensile strength (MPa)			Ultimate strain (%)		
	$E$			$f_u$			$\epsilon_u$		
	Value*	Average	SD	Value*	Average	SD	Value*	Average	SD
CFRP	83.8	99.2	2.0	1492	1242.7	98.6	1.7	1.3	0.1

\* Value provided by the manufacturer

### 3.2.3. CFRP anchors.

CFRP anchors with 10mm diameter were ready-made[85] while 8 mm and 12 mm anchors were fabricated using the same CFRP material used for the CFRP sheets. The length and the width of the CFRP sheets used to make the 8 mm anchors were 175 mm and 125mm, respectively. Similarly, sheets of 175 x 210mm were used to fabricate the 12 mm anchors. The mechanical properties of the 10 mm anchors that were used in this study, as provided by the manufacturer, are presented in Table 5.

Table 5: FRP Anchors Properties.

Material	Material Industrial Name	Density	Diameter (mm)	Surface Area (mm <sup>2</sup> )	Elastic Modulus (GPa)	Tensile strength (MPa)	Elongation at failure (%)
CFRP Anchors	MapeWrap C FIOCCO	1.8 g/cm <sup>3</sup>	10	26.79	230	4830	2

### 3.3. Test Matrix

This study investigates the effect of different FRP anchor parameters including anchor diameter, anchor inclination angle (dowel angle), embedment depth, fan length and fan angle on the flexural capacity of small-scale, normal weight concrete prisms. The test matrix is divided into four groups: (1) control group which includes plain concrete prism, strengthened unanchored prism, and strengthened and anchored prism with anchor parameters that are common in all groups; (2) prisms strengthened with CFRP laminates and anchored with different anchor diameters (3) prisms strengthened with CFRP laminates and anchored at different dowel angles; and (4) prisms strengthened with CFRP laminates and anchored at different embedment depths. The test matrix of this study is summarized in Table 6. It should be noted that three prisms of each strengthening scheme were prepared and tested to ensure consistency and accuracy of results. The designations of the specimens start with N to indicate that the concrete prism is of normal weight strength. Unstrengthened specimens are indicated by a letter C (for control) following the initial letter. On the other hand, unanchored strengthened specimens are identified by L1 signifying that the sample is strengthened by one layer of CFRP laminates. All other specimens are designated by AL1 indicating that the specimen is strengthened with one layer of anchored CFRP laminates. Specimen N-AL1-C represents the control anchored specimens for the normal weight concrete

groups. The letters and numbers following AL1 in the specimen's designation indicate the parameter that is investigated and the quantity of the tested parameter. The letters D, A, and E represent dowel diameter, insertion angle, and embedment depth, respectively. For example, specimen N-AL1-D8 is a normal weight concrete specimen strengthened with one layer of CFRP laminates and anchored with an anchor dowel diameter of 8 mm.

Table 6: Test matrix

Parameters	Specimen	$f'_c$ (MPa)	$d_a^1$ (mm)	$\beta^2$ (degrees)	$h_{emb}^3$ (mm)	Number of samples
Control	N-C	50	-	-	-	3
	N-L1	50	-	-	-	3
	N-AL1-C	50	10	90	75	3
Anchor dowel diameter	N-AL1-D8	50	8	90	75	3
	N-AL1-D12	50	12	90	75	3
Anchor embedment depth	N-AL1-E50	50	10	90	50	3
	N-AL1-E100	50	10	90	100	3
	N-AL1-E125	50	10	90	125	3
Anchor dowel angle	N-AL1-A45	50	10	45	75	3
	N-AL1-A135	50	10	135	75	3
	N-AL1-A155	50	10	155	75	3

<sup>1</sup> $d_a$ : anchor dowel diameter (mm).

<sup>2</sup> $\beta$ : anchor dowel insertion angle (degrees).

<sup>3</sup> $h_{emb}$ : anchor embedment depth (mm).

### 3.4. Test Setup

A mechanical testing machine (MATEST) was used for testing following the ASTM C1609 (C1609/C1609M) [86] testing manual for concrete prisms strengthened with FRP. The machine was equipped with appropriate bend fixtures, two displacement transducers, and software capable of recording the load and deflection values. All beams were tested under two-point loading at a displacement-controlled mode rate of 0.25 mm/min. Figure 28 shows the testing setup. In addition, to monitor the strain along the length of the CFRP laminates, four strain gauges were placed on half of the

strengthened prisms with 75 mm spacing between each strain gauge, as shown in Figure 29. The equidistance between strain gauges was chosen to ensure accurate and consecutive results while considering the same results for the other half part of the prism. Strain gauges were used to aid in the development of bond-slip models between the concrete and the anchored CFRP laminates.

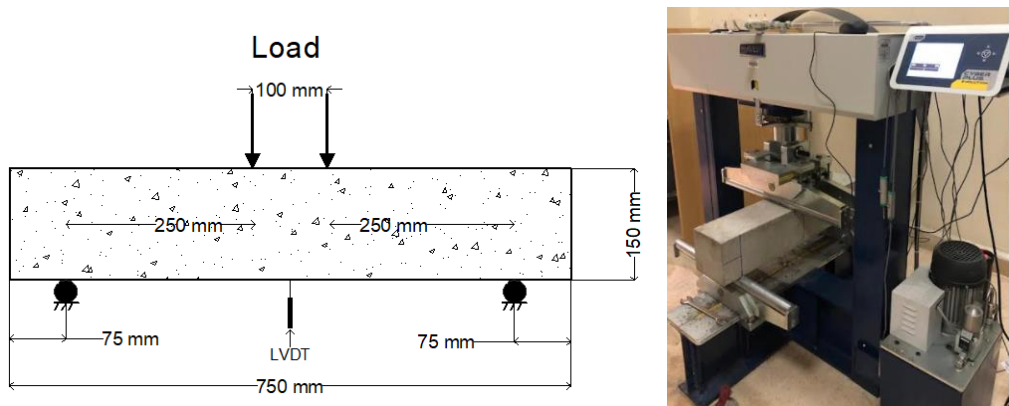


Figure 28: Test Setup

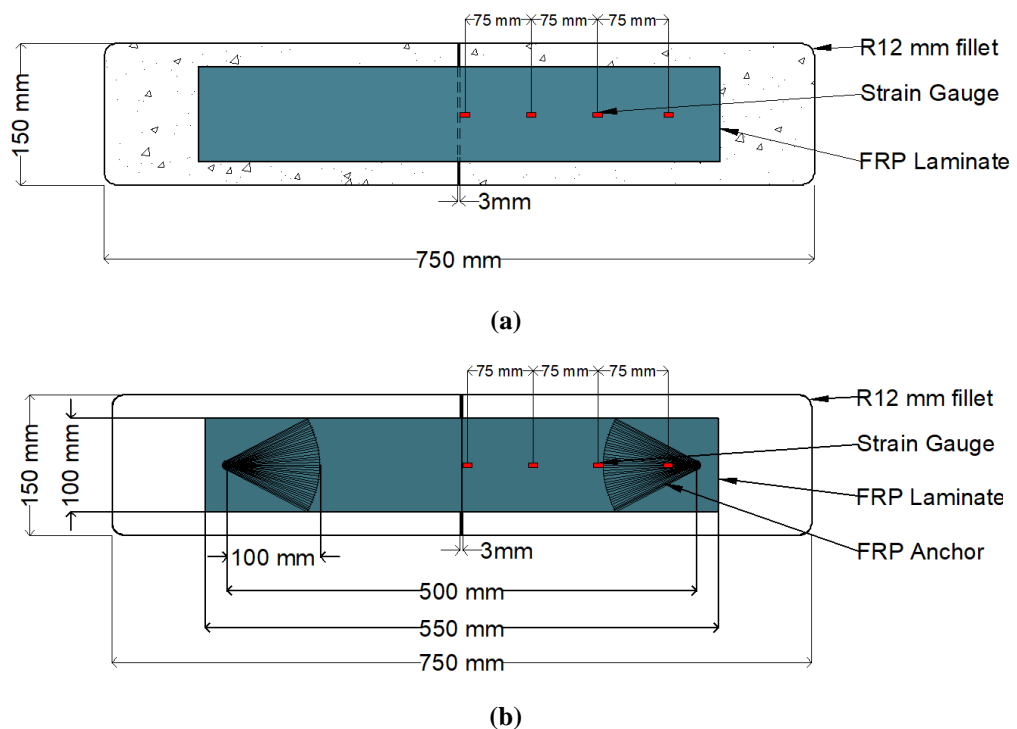


Figure 29: Strain gauge locations for prisms strengthened with: (a) CFRP laminates; (b) CFRP laminates and anchors.



### **3.5. Specimen Preparation and Strengthening**

#### **3.5.1. Concrete prism preparation**

Concrete prisms were cast at Emirates Beton Readymix. The formwork was prepared for the proposed prism size, and concrete was poured into the formwork. The concrete was poured into three equal layers and after pouring each layer the vibration table was used to remove air voids during the filling process. When the concrete hardened, formwork was removed, and prisms were cured for 28 days. In addition, concrete cubes and cylinders were cast for each casted batch of prism to determine the compressive strength of concrete.

#### **3.5.2. Strengthening of prisms**

Concrete surfaces, midspan notches, and anchor holes were prepared before strengthening. First of all, laitance was grinded off the bottom surface of concrete prisms and all dust was removed to improve the bond between the concrete and CFRP laminate, as shown in Figure 30a. Then, CFRP laminate and anchor hole locations were marked, and a 2.5 mm deep, 3 mm wide notch was cut at the bottom midspan (Figure 30b,c) to ensure the occurrence of concrete flexural cracking failure. After that, anchor holes were drilled from both ends of the prisms with different bit diameters. Beams having anchor diameters of 8-, 10-, and 12 mm were drilled using bits of 10-, 12-, and 14 mm, respectively. The purpose of the extra 2 mm in the hole diameter was to provide enough space for the impregnated anchor and epoxy. In addition, the drill was marked up to the required embedment for each specimen and was aligned at each hole to the required insertion angle using a protractor to ensure all parameters are achieved as shown in Figure 30d.; these holes were then cleaned and remeasured. To avoid premature failure and improve the insertion bond of the CFRP anchors in the concrete, the ends of the anchor holes were rounded while drilling providing a smoother surface for the transition segment of the anchor.

Next, CFRP sheets were prepared by cutting them from the sheet roll into strips of length 550 mm and width 100 mm. The 10 mm anchors were cut from the ready-made provided roll. On the other hand, the 8 and 12 mm anchors were handmade by cutting the sheets to a certain length and width depending on the anchor diameter, embedment depth, and fan length. The CFRP sheet dimensions for the 12 mm anchor were 210 x 175 mm (width x length). Similarly, for the 8 mm diameter anchor, the CFRP sheet was

cut to dimensions of 125 mm by 175 mm. All fibers in each sheet were separated and regrouped to form each anchor, and their diameter and dimensions were rechecked to satisfy the design. A sample of the prepared CFRP sheets and anchors is illustrated in Figure 31.

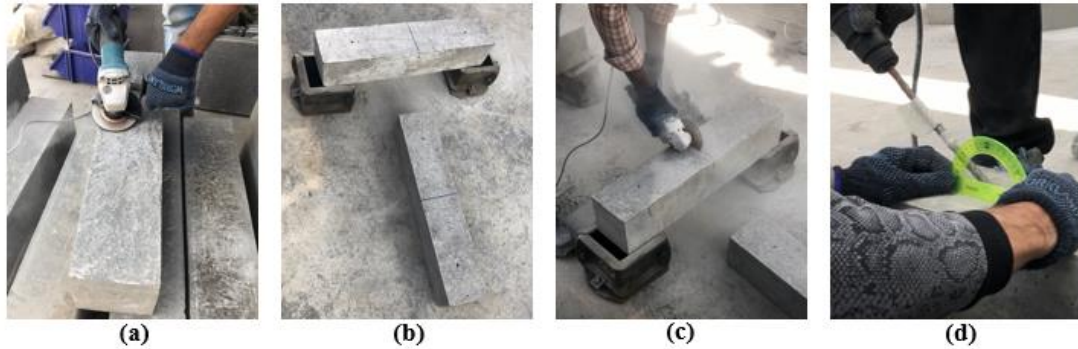


Figure 30: Prism preparation.

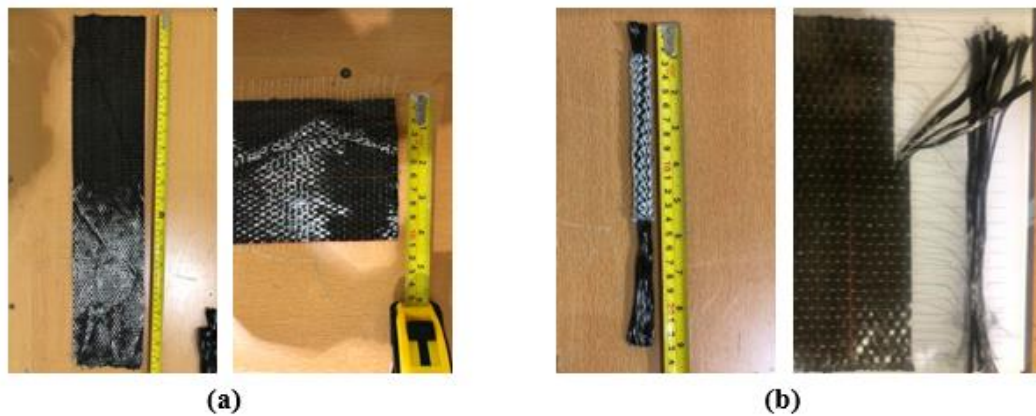


Figure 31: Sample of prepared CFRP sheet and anchor.

Insufficient amount of FRP material in anchors could lead to anchor rupture failure before sheet rupture, and this reduces the effectiveness of the system in terms of transferring tensile forces in the CFRP laminates; therefore, anchor material ratio (AMR) was also calculated. AMR is the equivalent cross-sectional area of the laminate used to make anchors divided by the cross-sectional area of the laminate developed by the anchors[57]. Usually, the manufacturer provides the nominal anchor diameter, but it is not recommended for calculating anchor area since it is not an exact measurement. In this research, the AMR for each anchor diameter was calculated using two methods.. The first method was conducted by dividing the equivalent sheet cross-sectional area used to make anchors for each diameter by the area of the dry sheet ( $w_{\text{sheet}} \times t_{\text{sheet}}$ ) used

for the flexural CFRP sheets. Since anchors with diameter 10 mm were readymade, the equivalent dry sheet area used was obtained by fabricating 10 mm diameter anchors from the same CFRP anchor material. The second method given by Jirsa et al. [87] was carried out by evaluating dry fiber weight per unit length and then calculating the anchor equivalent laminate area using Eq.52. Then the anchor material ratio (AMR) was calculated by Eq.54. For the 8 mm and 12 mm anchor diameter, the weight of anchors was obtained by multiplying the volume of the sheet used to fabricate the anchors by the density from the manufacturer's data sheet given in (kg/m<sup>3</sup>). Then, the weight of anchor per length and area were calculated and substituted in the equations. Since 10 mm anchors were readymade, the equivalent sheet area was obtained by fabricating a 10 mm anchor from the same material, making sure that the weight of the fabricated one is close to the readymade anchor. In order to obtain all AMR values, dry fiber properties were used in all calculations to maintain consistency. AMR values for both methods are tabulated in Table 7 and Table 8. AMR values herein ranged between 1.25 and 2.1 which is close to the range obtained in other studies [57], [87].

$$A_{eqv} = \frac{\lambda_A}{w_f \gamma_{s,exp}} \cdot w_f t_f \quad (52)$$

$$A_{sheet} = w_f t_f \quad (53)$$

$$AMR = \frac{A_{eqv}}{A_{sheet}} \quad (54)$$

Where:

$A_{eqv}$ : Anchor equivalent laminate area (cm<sup>2</sup>).

$A_{sheet}$ : Cross-sectional area of FRP sheets used on concrete substrate (cm<sup>2</sup>).

$\lambda_A$ : Weight of anchor per length (g/cm).

$\gamma_{s,exp}$ : Weight of sheet per surface area used to fabricate anchors (g/cm<sup>2</sup>)

$w_f$ : FRP sheet width (cm).

$t_f$ : FRP sheet thickness (cm).

Table 7: Anchor Material Ratio of different anchor diameter – Method 1.

Anchor diameter (mm)	$w_{sheet}$ (mm)	$t_f$ (mm)	Equivalent area of dry fiber (mm <sup>2</sup> )	Area of dry sheet (mm <sup>2</sup> )	AMR
8	125	0.164	20.5	16.4	1.25
10	160	0.164	26.24	16.4	1.60
12	210	0.164	34.44	16.4	2.10

Table 8: Anchor Material Ratio of different anchor diameter – Method 2.

Anchor diameter (mm)	$L_{sheet}$ (mm)	$w_{sheet}$ (mm)	$t_f$ (mm)	Weight of dry anchor (g)	$\lambda_A$ (g/cm)	$\gamma_{s,exp}$ (g/cm <sup>2</sup> )	$A_{eqv}$ (cm <sup>2</sup> )	AMR
8	175	125	0.164	6.458	0.369	0.0295	0.205	1.25
	150			7.085				
10	175	160	0.164	8.266	0.472	0.0295	0.262	1.60
	200			9.446				
	225			10.267				
12	175	210	0.164	34.44	0.620	0.0295	0.344	2.10

The two-component primer (Primer1) and epoxy adhesive (MapeWrap31) were each mixed by following the manufacturer's instructions at a ratio of 3:1 (Figure 32a). The first step in the strengthening process was to brush the prism surface with a layer of primer to ensure better bonding with the CFRP laminate, as shown in Figure 32b. Next, CFRP sheets were installed using the wet layup method in which the dry fibers were impregnated in the epoxy (Figure 32c) and placed on the marked area at the bottom of the prism (Figure 32d). Groove rollers were used to remove all air bubbles and densify the laminate. Following that, fibers on the hole locations were gently separated using the edge of a metallic spatula, and anchors were impregnated in the epoxy and inserted into the holes (Figure 32e). Groove rollers were used again to remove any air voids, as shown in Figure 32f. Finally, prisms were left to dry for 3-4 days before testing, and strain gauges were placed in the proposed locations (Figure 33).

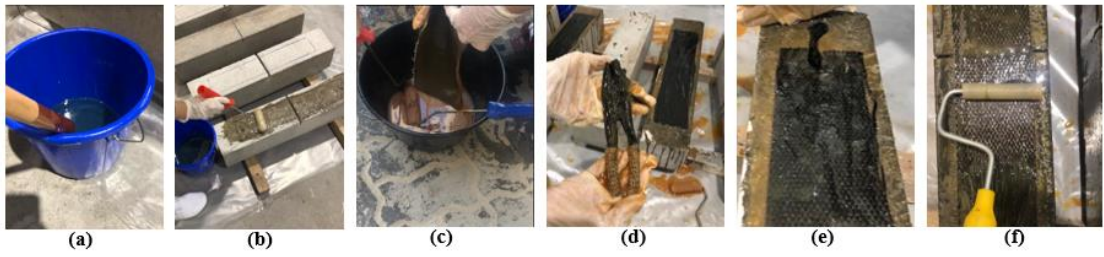


Figure 32: Strengthening procedure.




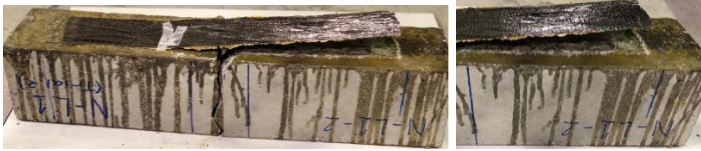






Figure 33: After strengthening: (a) dry prisms; (b) dry prisms with strain gauges.

## Chapter 4. Experimental Results




### 4.1. Failure Modes

All beams in this study were designed to fail in flexure in the midspan area. Table 9 shows the failure modes for each prism with different anchor parameters. The common failure mode in all strengthened prisms was CFRP sheet debonding but with different anchor failure modes.

Table 9: Types of failure mode for each prism designation.

Prism Designation	Physical Observation	Failure Mode
N-C		Flexural concrete crack
N-L1		Debonding
N-AL1-C-E75		Debonding + anchor rupture at key portion
N-AL1-D8		Debonding + anchor rupture at key portion
N-AL1-D12		Debonding
N-AL1-E50		Debonding + anchor rupture at key portion
N-AL1-E100		Debonding + anchor rupture at key portion
N-AL1-E125		Debonding + anchor rupture at key portion



N-AL1-A45		Debonding + anchor rupture at key portion
N-AL1-A135		Debonding + partial anchor pullout
N-AL1-A155		Debonding + partial anchor pullout

It can be observed from Table 9 that the control unstrengthened prism N-C failed with flexural concrete cracking, while the control strengthened prism with one CFRP layer N-L1 failed by sheet debonding. The failure modes for all the tests reported herein were debonding with anchor rupture or anchor pullout. The rupture of the anchor fibers at the key portion at the junction of the anchor dowel and anchor fan could be due to many factors such as the pullout force or shear force in anchors, reduction in strength due to the bent fibers, and stress concentrations at the bent transition region directly above the impregnated dowel region of the anchor. Anchor rupture was observed at the key portion, at middle length at the top of the anchor [88].

With respect to the anchor diameter group, prisms N-AL1-D8 and prism N-AL1-C (D10) failed by anchor rupture at key portion along with sheet debonding. Increasing the anchor diameter to 12 mm for prism N-AL1-D12, changed the failure mode to midspan sheet debonding only without any effect on the anchors. Prisms N-AL1-A45 with 45° insertion angle failed by anchor rupture at key portion and debonding of the CFRP laminate. On the other hand, increasing the anchor dowel angle above 90° increased the capacity of anchors and resulted in sheet debonding and anchor pullout, as illustrated for prisms N-AL1-A135 and N-AL1-A155. In addition, prisms with dowel angles above 90° were able to transfer the load better than smaller ones and resulted in larger load carrying capacities. Prisms N-AL1-E50, N-AL1-E100, and N-AL1-E125 failed by anchor rupture at key portion along with CFRP laminate debonding. This shows that embedding the anchors at different depths of 50, 100, and 125 mm were insufficient for transferring all the load, since they resulted in anchor rupture before the laminate; yet, increasing the embedment depth increased the capacity of the prisms.

## 4.2. Load-deflection Responses

The load-deflection responses of all prisms will be presented in this section. Load values were obtained from Matest concrete flexural machine, while displacement values were obtained from the LVDT placed at the midspan of the prisms from both sides. The control group that includes 3 prism designations were set in all load-deflection graphs for comparison purposes, since N-C and N-L1 are set as the benchmark, and N-AL1-C has common anchor parameters from each group. Figures 34-37 show the plotted load-deflection responses of all representative prisms. It should be noted that tests were terminated after the failure occurred, and the load dropped by more than 50 percent.

It can be seen from Figures 34-37 that all prisms have close initial stiffness since the slopes of the ascending part are similar. They all had a stiff linear segment up to concrete flexural cracking, followed by an increase of load and deflections. The typical load-deflection response of a strengthened prisms consists mainly of 3 phases. The first phase presented a linear curve before flexural cracking which means that the CFRP laminate was completely bonded to the concrete substrate until cracking load was attained. At the second phase, the curves undergo gradual softening due to the flexural cracking. At this stage, the CFRP laminates started to debond from the concrete substrate, while the load resistance of the prisms increased. Finally, the third phase represents the stage where the load is mostly transferred to the anchors. A nearly linear curve is observed at this stage which is followed by a sudden drop in the load-deflection curve due to failure after reaching the ultimate load. At ultimate load, rupture of CFRP laminate could be observed if CFRP anchors were designed and installed properly to sufficiently carry the transferred load. If not, anchor rupture at the bent portion of the anchor or between the sheet and anchor was observed. In all cases, brittle and sudden failure occurred [89]. Different failure modes were observed in this study depending on the anchor parameters.

The slope of the load-deflection graph of the unstrengthened control specimen (N-C) started to decrease after attaining a load of 22 kN, and then suddenly dropped due to failure. Load-deflection response of the strengthened, unanchored prism N-L1 shows that strengthening concrete without anchorage enhanced the load-carrying capacity of the beams. The slope remained constant until reaching an ultimate load value of 35.31



kN. Following that, the load slightly decreased for a short interval, followed by a sudden drop that indicated the occurrence of debonding. The failure of the strengthened unanchored prism was brittle where less ductility was exhibited before failure, compared to the anchored prisms. On the other hand, anchoring CFRP laminates with CFRP anchors enhanced the load-carrying capacity, leading to a ductile failure mode. The load-deflection graph of N-AL1-C shows that the stiffness remained constant up to 23 kN after which the slope decreased, while the load carrying capacity increased until it reached a value of 42.05 kN. Then, the capacity decreased leading to failure. Similarly, all other strengthened and anchored prisms had a similar trend but with differences in the ultimate load and deflection values.

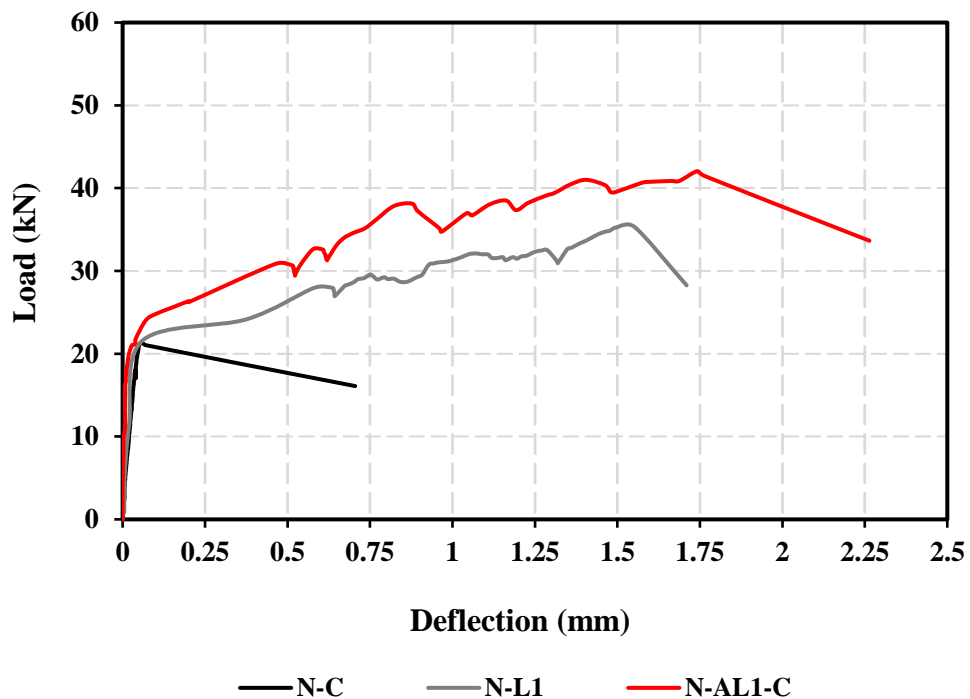


Figure 34: Load-Midspan deflection curves for the control group.

Load-displacement curves of dowel diameter group in Figure 35 shows a relation between the anchor diameter and initial stiffness where the prisms with anchor diameter 12 mm had the highest stiffness followed by the 10 mm and 8 mm dowel diameters. Furthermore, prism N-AL1-D12 recorded the highest ultimate capacity value of 45.39 kN. N-AL1-D8, and N-AL1-C (D10) had an ultimate load value of 37.63 kN and 42.05 kN, respectively. Therefore, it can indicate that there is a direct relation between anchor diameter and ultimate capacity since the increase in diameter showed a trend in capacity

increase. Moreover, the anchor diameter group reflected a good enhancement in deformability and capacity when compared to unanchored prisms.

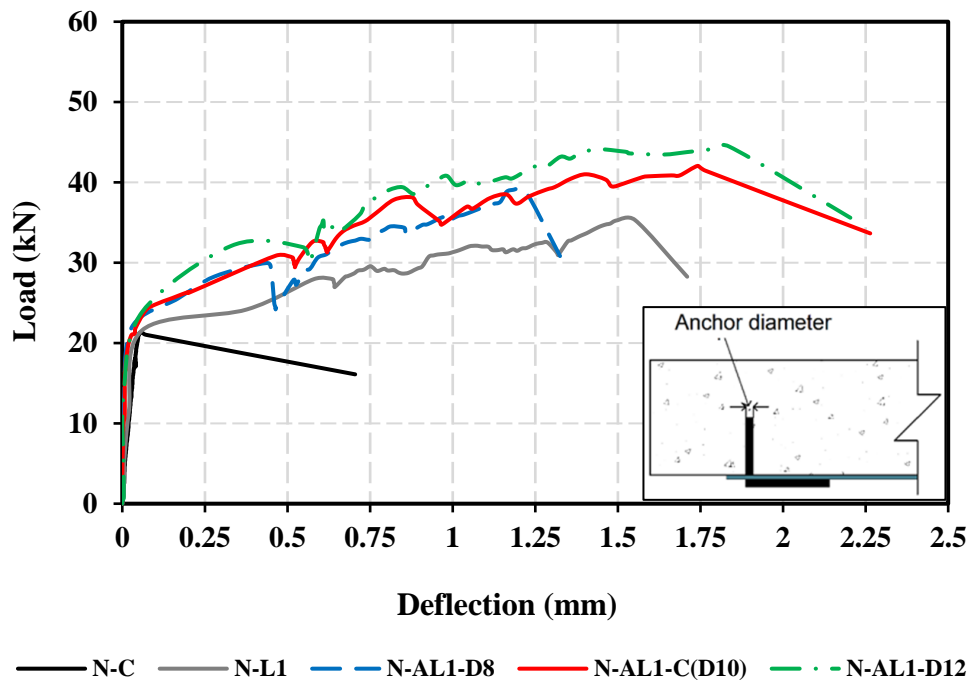


Figure 35: Load-Midspan deflection curves for the anchor diameter group.

Load-deflection responses of embedment depth group in Figure 36 illustrated a clear trend where increasing embedment depths showed better results in terms of increasing the load-carrying capacity of the specimens. Also, the ultimate deflection value of N-AL1-E125 was the highest among other embedment depth prisms, with ultimate load and ultimate deflection values of 51.31 kN and 2.41 mm, respectively. Similarly, load-deflection responses of insertion angle group in Figure 37 showed a direct relation between the insertion angle and load-carrying capacity, i.e., increasing the dowel angle (away from center of prisms) enhanced the load-carrying capacity of the specimens. N-AL1-A155 performed better in terms load-carrying capacity and deformability; the ultimate load and deflection values were 52.83 kN and 2.41 mm, respectively.

For each anchor parameter, 3 specimens were tested to ensure the accuracy of results. Figures 38-41 illustrate the load-deflection responses for the 3 trials of each designation. The results represented previously demonstrate the representative trial for each designation.

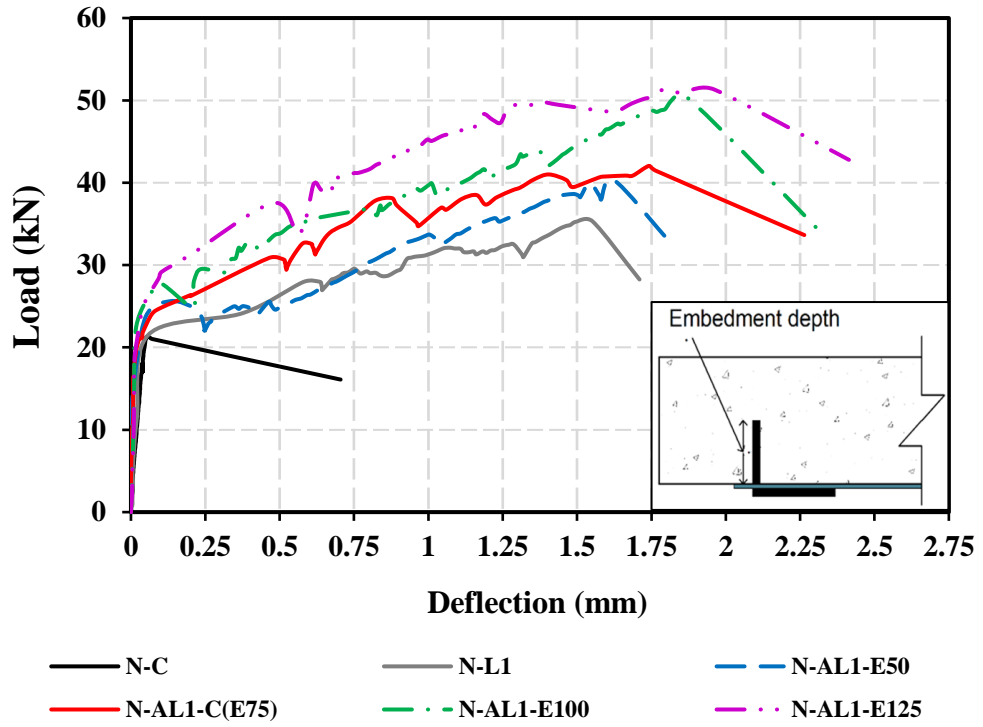


Figure 36: Load-Midspan deflection curves for the embedment depth group.

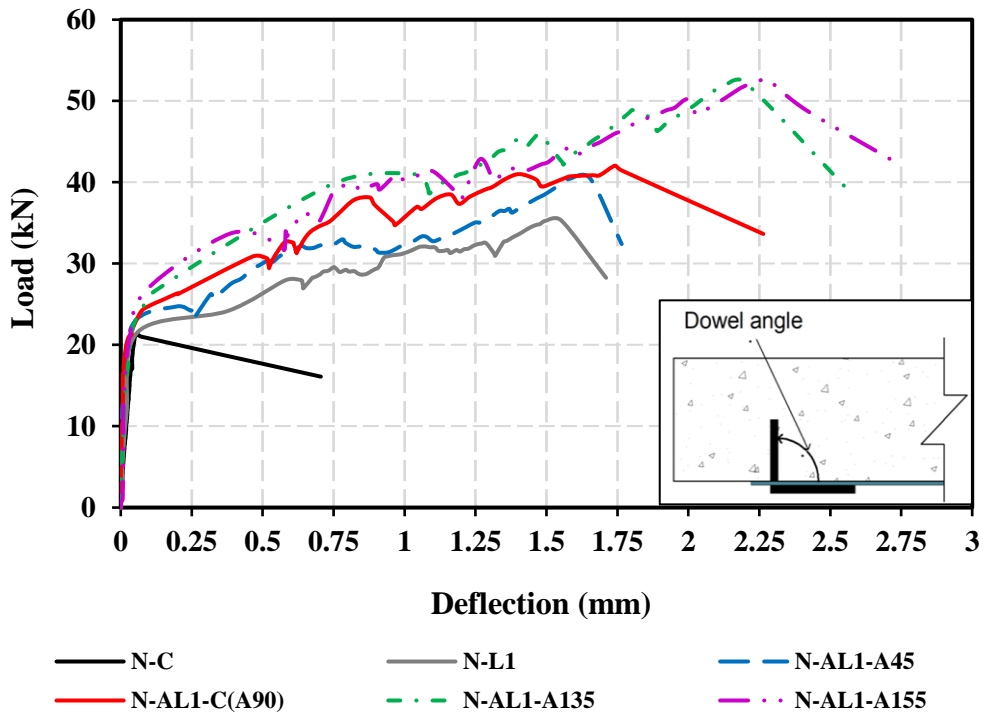
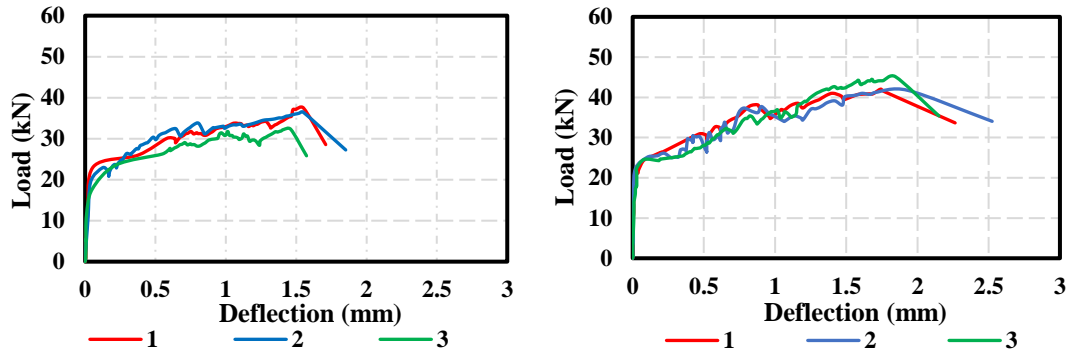


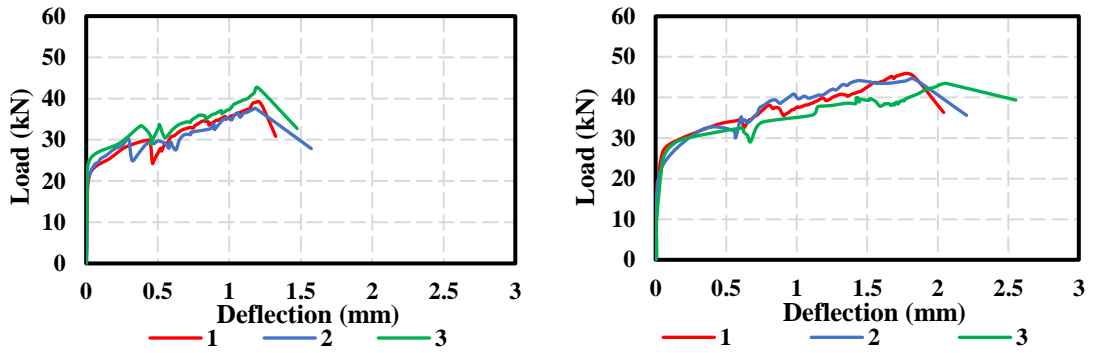
Figure 37: Load-Midspan deflection curves for dowel angle group.



(a) N-L1

(b) N-AL1-C

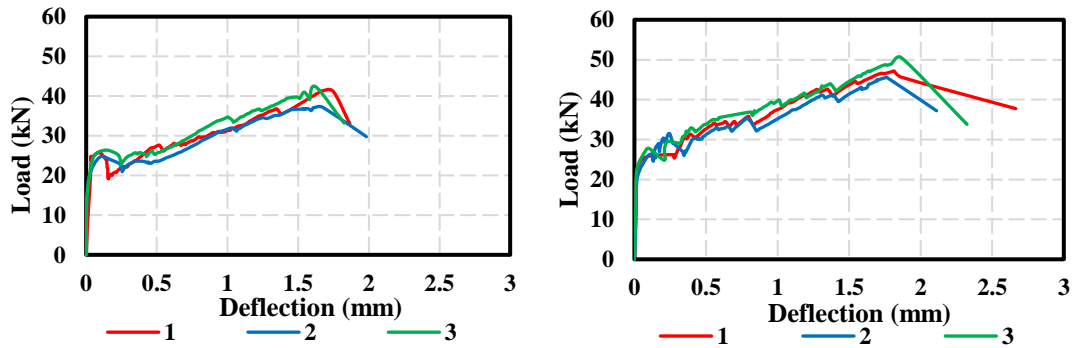
Figure 38: Load-deflection curves of control group-3 trials.



(a) N-AL1-D8

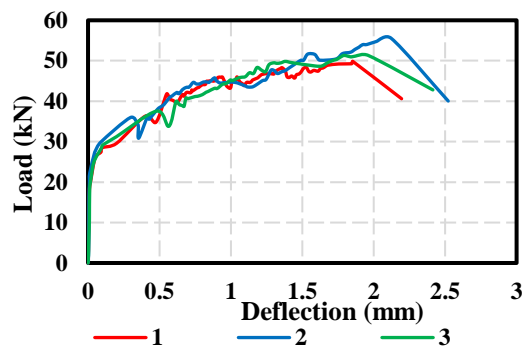
(b) N-AL1-D12

Figure 39: Load-deflection curves of anchor dowel diameter group-3 trials.



(a) N-AL1-E50

(b) N-AL1-E100



(c) N-AL1-E125

Figure 40: Load-deflection curves of anchor embedment depth group-3 trials.

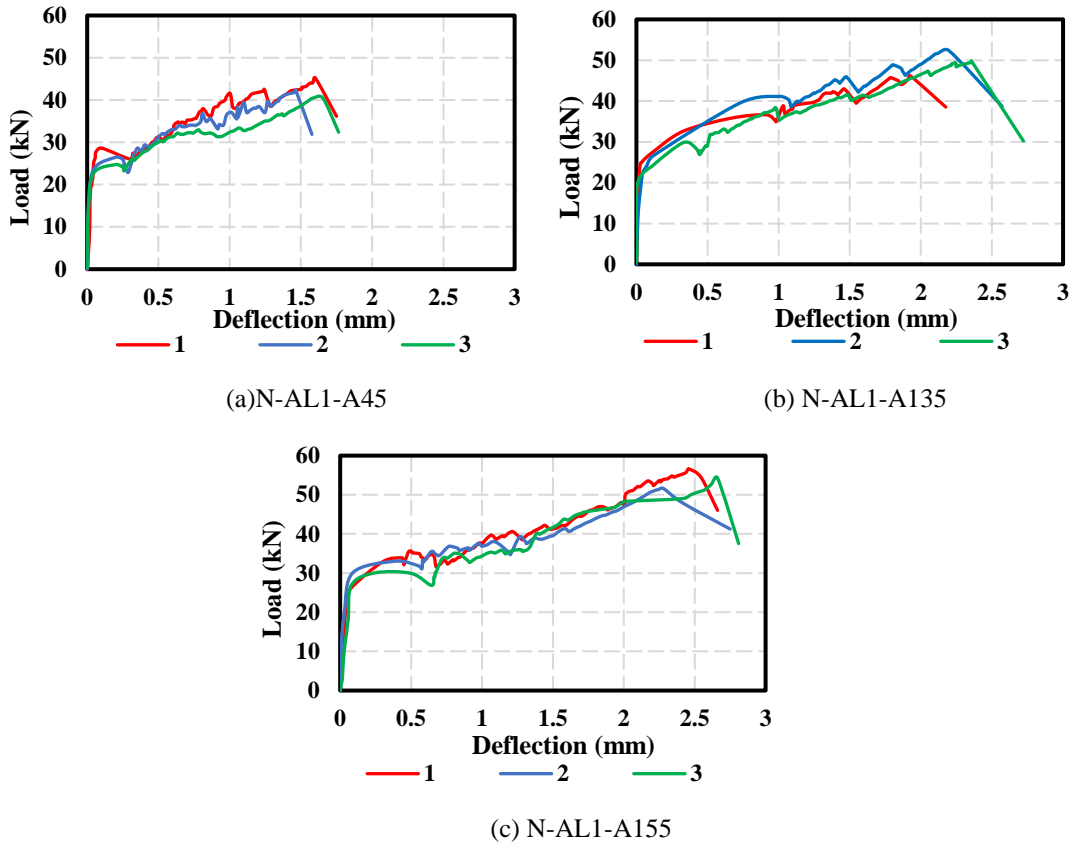


Figure 41: Load-deflection curves of anchor dowel angle group- 3 trails.

### 4.3. Ultimate Load, Deflection, and Maximum Deflection

Measured values of ultimate load ( $P_u$ ), deflection at ultimate load ( $\delta_u$ ), and maximum deflection with their standard deviations are summarized in Table 10. The results indicate that strengthening using CFRP laminates enhanced the ultimate load carrying capacity of concrete prisms from approximately 21 kN to 35 kN. In addition, anchoring the CFRP laminates with CFRP anchors increased the ultimate load capacities even more since the CFRP laminates were utilized in terms of strength and deflection. Results analysis on the performance and effect of anchor diameter, anchor embedment depth and anchor dowel angle on the flexural load capacity and anchor efficiency are presented in the next chapter.

Table 10: Test results in terms of ultimate load, ultimate deflection, and maximum deflection.

	Prism Designation	$P_u$ (kN)	$\delta_u$ (mm)	$\delta_{max}$ (mm)
Control group	N-C	$20.81 \pm 1.88$	$0.2 \pm 0.04$	$0.24 \pm 0.06$
	N-L1	$35.02 \pm 2.61$	$1.54 \pm 0.08$	$1.71 \pm 0.14$
	N-AL1-C	$44.18 \pm 2.79$	$1.84 \pm 0.1$	$2.26 \pm 0.18$

Dowel diameter group	N-AL1-D8	39.03 ± 2.65	1.32 ± 0.16	1.44 ± 0.12
	N-AL1-D12	46.30 ± 3.78	1.97 ± 0.13	2.29 ± 0.26
Embedment depth group	N-AL1-E50	40.26 ± 2.72	1.68 ± 0.1	1.81 ± 0.12
	N-AL1-E100	47.77 ± 2.53	1.87 ± 0.16	2.30 ± 0.18
	N-AL1-E125	52.18 ± 2.95	1.98 ± 0.14	2.37 ± 0.17
Dowel insertion angle group	N-AL1-A45	41.41 ± 3.24	1.57 ± 0.09	1.70 ± 0.10
	N-AL1A135	49.45 ± 3.13	2.33 ± 0.19	2.71 ± 0.17
	N-AL1-A155	52.63 ± 4.24	2.39 ± 0.27	2.62 ± 0.29

Note: Ranges based on standard deviation.

#### 4.4. Strains in the CFRP

To evaluate the effect of CFRP ultimate strain, 4 strain gauges were attached on each laminate from center till the tip of the anchor and one on the anchor, from one side of the prism. Locations of strain gauges are illustrated in Figure 42. Figures 43-46 show the load versus CFRP strain development of all strengthened prisms at the proposed locations. Different load levels were considered to specify strain values, which were at 20%, 40%, 60%, 80%, and 100% of the recorded ultimate load. Maximum CFRP strain values corresponding to ultimate load ( $\epsilon_{ult}$ ), ratio of maximum strain of anchored prism to unanchored prism at ultimate load level, and percentage of strain utilization according to the measure ruptured strain values are reported in Table 11. Strain distribution along the CFRP laminate is plotted at different load levels. The flexural crack initiated the failure modes of all prisms at the center. This flexural crack caused a significant increase in strain measurements, indicating that debonding has been initiated with other type of anchor failure modes in most prisms. Strain values decreased as moving towards the end of the sheet; moreover, increase in load level led to an increase in the strain readings in all gauges.

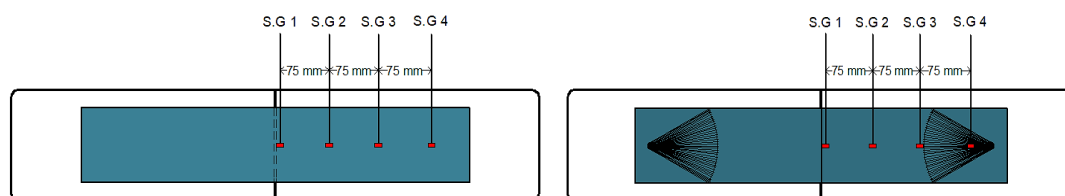


Figure 42: Location of strain gauges for strain values.

Observing Figures 43a of the unanchored prism, it can be seen that strain values at 20% of the ultimate load were minimal until the load reached to 40% of the ultimate load

value at 18 kN, which is at the point where the cracking was clearly observed and debonding failure started. As the load increased, the strain increased until complete debonding failure was observed at ultimate load. This increase in strain values implies that the CFRP laminate gets activated and starts resisting load after flexural cracking, leading to debonding propagation throughout the laminate till failure. Moving on to all anchored prisms, the strain values showed different trend due to the different parameters.

Control prism N-AL1-C (Figure 43b) showed similar behavior at all load levels in which the maximum strain was at the center. Flexural cracking started at the lowest load level but was clearly observed at 40% of the ultimate load; however, the debonding initiated at the next load level and started to move toward the end of the laminate. About zero strain was on the anchor close to the end of the sheet in the first three load levels, then the strain started to increase when anchor rupture occurred after debonding and showed a minor strain value near the end of the sheet when reaching the ultimate load level. The ultimate capacities of specimens N-L1 and N-AL1-C were 35.02 kN and 44.18 kN, corresponding to maximum recorded center strain values of 3544.01 and 6933.30  $\mu\epsilon$ , respectively.

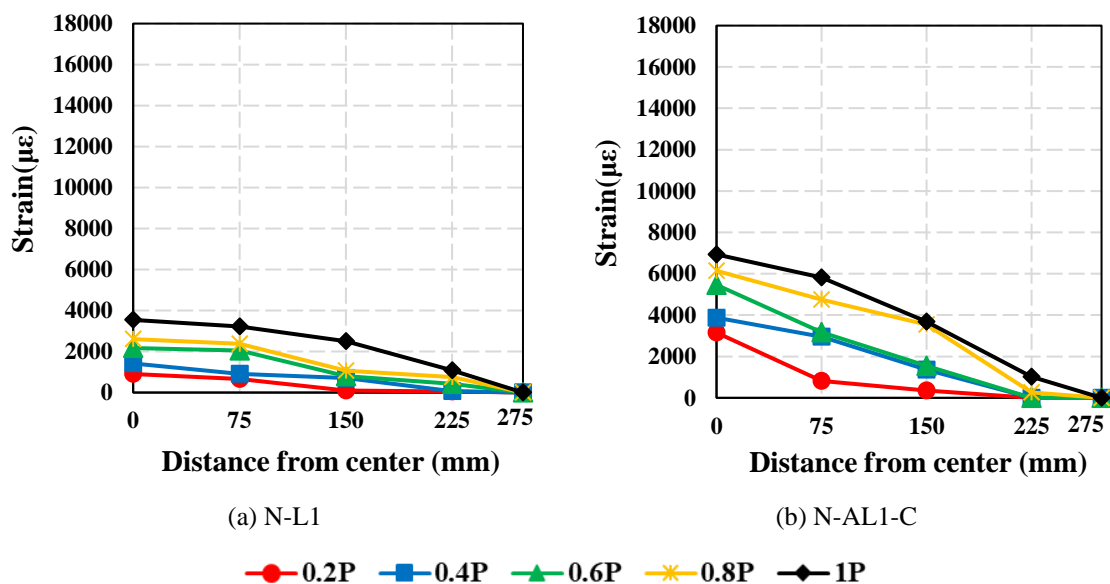


Figure 43: Strain versus distance plot of control group: (a) unanchored prism; (b) anchored control prism.

With respect to the dowel diameter group, different strain distributions were observed. In N-AL1-D8 prism, the CFRP laminate started debonding at the second load level (0.4P) with no effect near the end of the sheet. As the load increased, the force was

distributed throughout the sheet and debonding propagated causing an increase in strains in the last three load levels, as shown in. Figure 44a. Comparing this prism to the control prism (N-AL1-C) with 10 mm dowel diameter, it can be observed that increasing the anchor diameter reduces the strain at the anchor, and thus delays anchor rupture failure. Furthermore, increasing the dowel diameter to 12 mm resulted only in debonding failure with no anchor failure, and debonding was initiated at 40% of the ultimate load as the prisms of this group. The strain versus distance values of this prism is plotted in Figure 44b. The ultimate capacities of prisms N-AL1-D8 and N-AL1-D12 were 39.03 kN and 46.30 kN with maximum center strain values of 4061.39 and 7692.779  $\mu\epsilon$ , respectively. This indicates that increasing the dowel diameters not only increases the capacity of the prism, but also the strain on the CFRP laminate especially at the center where flexural cracking occurs.

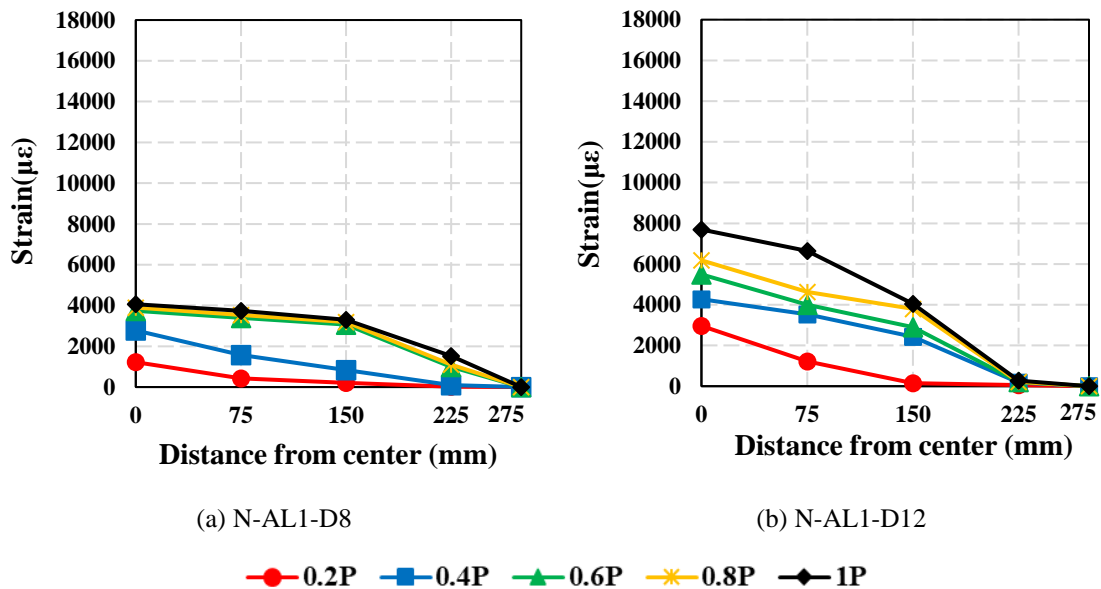


Figure 44: Load versus distance plot of dowel diameter group.

The prisms of the embedment depth group failed by debonding and anchor rupture. As illustrated in Figure 45a, the lowest anchor embedment depth (50mm) did not have an effect in delaying debonding, and therefore the strain significantly increased on the laminate and anchor directly after passing the first load level. On the other hand, higher embedment depth of values 100 mm enhanced the capacity of the prisms resulting in lower strain values at the early levels of loads. N-AL1-E100 plot in Figure 45b shows that the CFRP laminate sustained low strain values with no strain at the anchors even after cracking at 25 kN (0.6 P). This indicates that the system resisted the load after



cracking, then debonding and anchor rupture occurred due to higher strain values in the next load levels. In addition, N-AL1-E125 (Figure 45c) showed a similar trend but with higher strain values after the start of flexural cracking directly (0.4P). The ultimate loads recorded for prisms N-AL1-E50, N-AL1-E100, and N-AL1-E125 were 40.26 kN, 47.77 kN, and 52.18 kN, with corresponding maximum strain values of 4978.05, 8478.56 and 10440.04  $\mu\epsilon$ , respectively. When comparing these values with the control prism N-AL1-C (E75), it can be observed that increasing embedment depth shows a trend in terms of increased strain values.

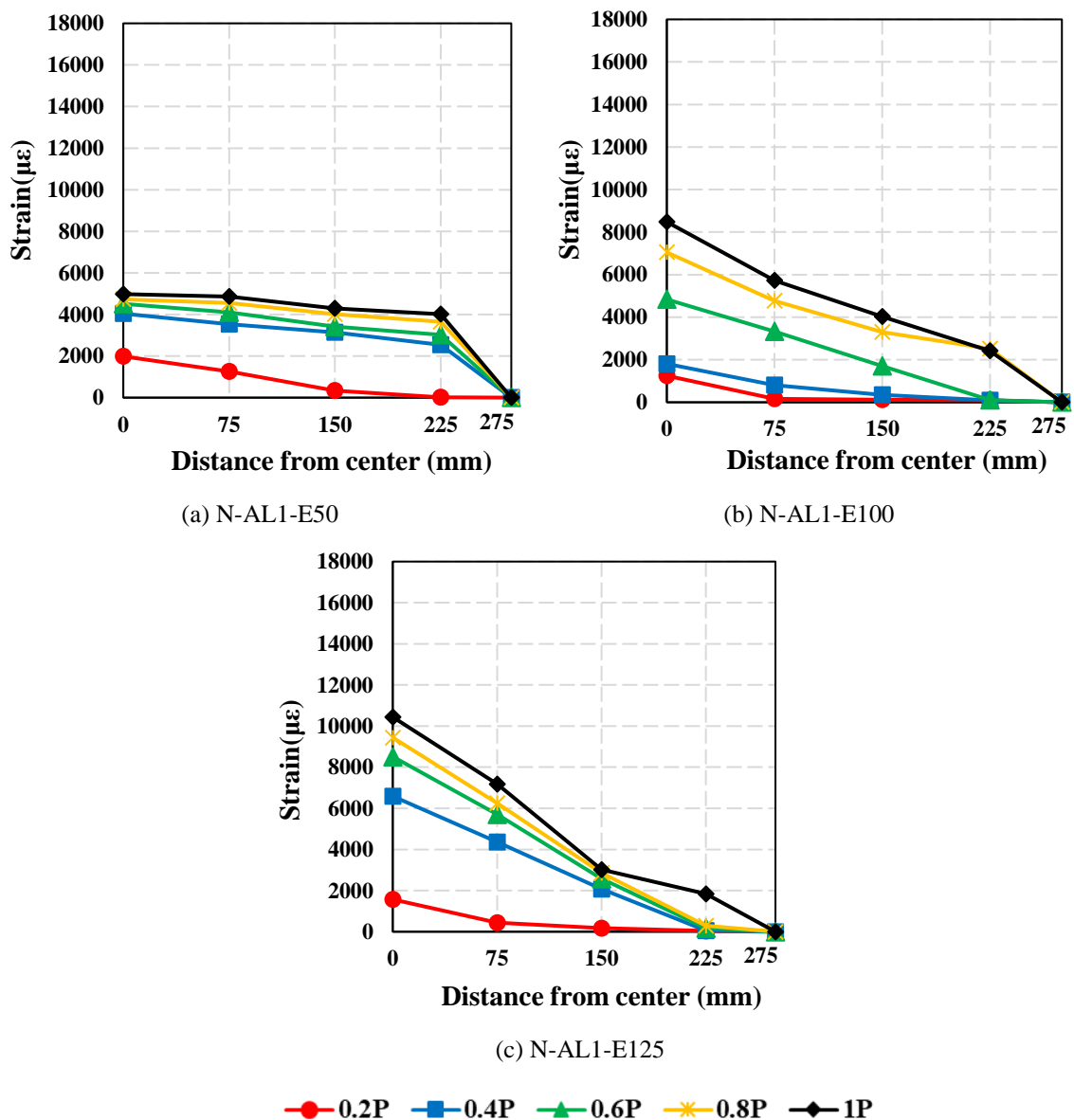
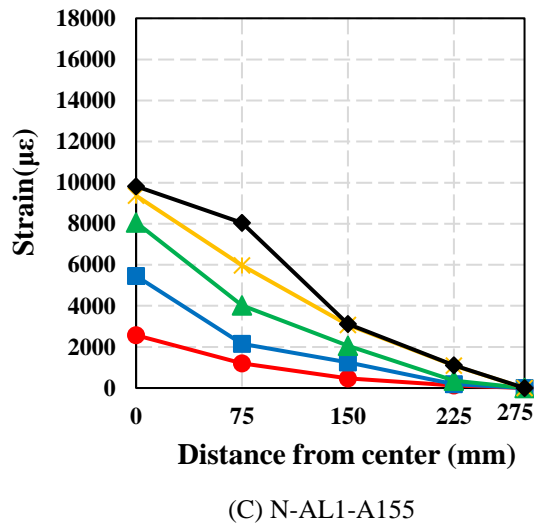
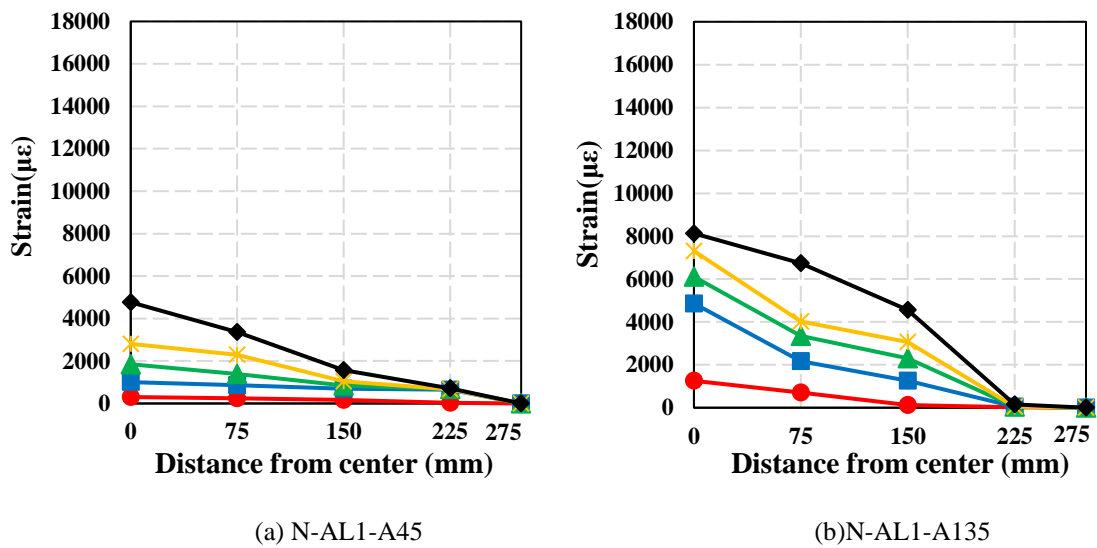


Figure 45: Strain versus plot of embedment depth group.

The data collected from the strain gauges of the dowel angle group shows that N-AL1-A45 (Figure 46a) had the lowest strain values, and the plot of the first two load levels were approximately horizontal, which indicates that the failure started early along the sheet to the anchor. As the load increased, the strain values increased especially in the center part of the prism. This led to anchor rupture failure prior to debonding at low strain values. On the other hand, larger angle dowels (N-AL1-A135 and N-AL1-A155) resulted in higher strain values on the laminate with similar failure behavior as other prisms.



● 0.2P   
 ■ 0.4P   
 ▲ 0.6P   
 ✱ 0.8P   
 ◆ 1P

Figure 46: Strain versus distance plot of anchor dowel angle group.

About zero strain was recorded on the anchor; however, anchor pullout was the failure mode of these two prisms. Ultimate loads for prisms N-AL1-A45, N-AL1-A135, and

N-AL1-A155 were 40.51 kN, 49.82 kN, and 52.83 kN with corresponding maximum strains of 4768.13, 8129.47 and 11082.12  $\mu\epsilon$ , respectively. All strengthened prisms did not reach rupture strain of 13000  $\mu\epsilon$  since non failed by sheet rupture, and debonding failure was dominant.

Table 11 presents the normalized average ultimate strain values showing the effect of anchoring on the utilization of strain with respect to the obtained rupture strain. Moreover, the percentage increase of strain values of anchored prisms with respect to the unanchored one was also presented and ranged between 12% and 126%. Using 8 mm diameter anchors utilized the strain by 42% only; however, increasing the diameters to 10 mm and 12 mm showed close percentage strain utilization values of 59% and 65%, respectively. Increasing the anchor embedment depths resulted in clear strain utilization that ranges between 46%-84% with respect to rupture strain. In addition, anchor dowel angle was effective in utilizing the strain; using 45° anchors utilized the strain by 48% only. On the other hand, obtuse angles (135° and 155°) showed more utilization percentages values of 74% and 83%, respectively.

Table 11: Normalized ultimate strain values.

Prism Designation	$\epsilon_{ult}^1$	$\frac{\epsilon_{ult,a}}{\epsilon_{ult,ua}}^2$	% Increase of $\epsilon_{ult}$ with respect to N-L1	% Strain utilization with respect to $\epsilon_f^3$
N-L1	4699	-		37
N-AL1-C	7409	2.09	58	59
N-AL1-D8	5281	1.49	12	42
N-AL1-D12	8244	2.33	75	65
N-AL1-E50	5801	1.64	23	46
N-AL1-E100	8896	2.51	89	71
N-AL1-E125	10642	3.00	126	84
N-AL1-A45	6007	1.69	28	48
N-AL1-A135	9313	2.63	98	74
N-AL1-A155	10462	2.95	123	83

<sup>1</sup> Maximum average strain corresponding to ultimate load level.

<sup>2</sup> Ratio of maximum average strain of anchored prism to unanchored prism at ultimate load level.

<sup>3</sup> Ultimate rupture strain of CFRP laminate.

## **Chapter 5. Discussion of Results**

### **5.1. Strengthening without anchors**

Using FRP laminates in strengthening concrete beams increased the ultimate load carrying capacity and delayed the failure of the structure. Concrete prisms strengthened with CFRP laminate resulted in significant increase in the load carrying capacity of the prism by 68 % when compared to unstrengthened prisms. Furthermore, unanchored prisms failed by CFRP debonding where the laminate debonded from the concrete substrate at low CFRP strain levels throughout the laminate. Strain values of unanchored prisms are much lower than those of anchored prisms due to their lower load resistance capacities; thus, they delayed concrete flexural failure.

### **5.2. Strengthening with anchors**

FRP spike anchors consists of anchor dowel embedded into the concrete substrate and anchor fan bonded on the FRP reinforcement on the concrete surface. Two main parameters could affect the efficiency of FRP anchors which are geometrical and installation parameters. Geometrical parameters are variables that affect the characteristics of the dowel and fan regions. Anchor dowel parameters include the embedment depth, hole diameter, dowel diameter, and dowel angle. Further, hole edge is also considered a geometrical parameter since it affects the bend radius of the anchor, and hence reduces the stress concentration in the bended region. Anchor fan parameters include fan angle, fan type (single or bow-tie fan), fan length, and fan position relative to the FRP reinforcement. Installation and manufacturing techniques influence the quality of the strengthened and anchored structure. Most researchers fabricate anchors from FRP sheets instead of using readymade ones from the manufacturer; however, this depends on the availability of the studied anchor's diameters and material type. Locating anchors within the stress transfer zone improves its efficiency if included within the development length of the adherent mechanism. No agreement was reached about the best distance of anchors from the end of the FRP reinforcement; however, authors found that anchor enhancements are valid when the bonded length is increased up to 200 mm. Moreover, anchor arrangements like number of anchors, number of rows, anchor alignment and location (within the stress transfer zone), and distance between anchors also influence anchor efficiency. More research is needed on design of multiple anchors, yet it is assumed that the anchor fan width should be equal to the

width of the FRP reinforcement bonded to it [90]. In this section, several parameters related to the geometrical configuration and anchor arrangement were studied. The effect of these parameters will be discussed showing the anchor efficiency on the strengthened structure for each parameter. Table 12 shows the average ultimate load values and normalized ultimate load ratios with respect to unanchored prisms and unstrengthened prisms. Furthermore, capacity percentage increase with respect to N-L1 and N-C was presented. In addition, Figure 47 summarizes the percentage increase in the load carrying capacities of all strengthened prisms in comparison with plain unstrengthened prism.

Table 12: Normalized ultimate load values.

<b>Prism</b>	$P_{ult}^1$ (kN)	$\frac{P_{u,a}^2}{P_{u,ua}}$	$\frac{P_{u,s}^3}{P_{u,us}}$	<b>% Increase of Pu with respect to N-L1</b>	<b>% Increase of Pu with respect to N-C</b>
<b>C</b>	20.81	-	-	-	-
<b>L1</b>	35.02	-	1.68	-	68
<b>N-AL1-C</b>	44.18	1.26	2.12	26	112
<b>N-AL1-D8</b>	39.03	1.11	1.88	11	88
<b>N-AL1-D12</b>	46.30	1.32	2.22	32	122
<b>N-AL1-E50</b>	40.26	1.15	1.93	18	93
<b>N-AL1-E100</b>	47.77	1.36	2.30	41	130
<b>N-AL1-E125</b>	52.18	1.49	2.51	49	151
<b>N-AL1-A45</b>	41.40	1.18	1.99	18	99
<b>N-AL1-A135</b>	49.45	1.41	2.38	41	138
<b>N-AL1-A155</b>	52.63	1.50	2.53	50	153

<sup>1</sup> Ultimate load (kN).

<sup>2</sup> Normalized ultimate load values, ratio of anchored to unanchored ultimate load.

<sup>3</sup> Normalized ultimate load values, ratio of strengthened to unstrengthened ultimate load.

FRP anchors enhanced the strength and deformability of concrete prisms strengthened with CFRP laminates. The anchors also utilized the strength properties of the CFRP laminates. However, their main role was to delay debonding by resisting the internal stresses through the sheet and providing a load transfer mechanism to the concrete.

Different anchor parameters showed different results in terms of load-carrying capacity, deflection, and strain values. Moreover, a percentage increase in the ultimate load carrying capacity ranging between 66%-158% was documented when compared to unstrengthened prism (N-C).

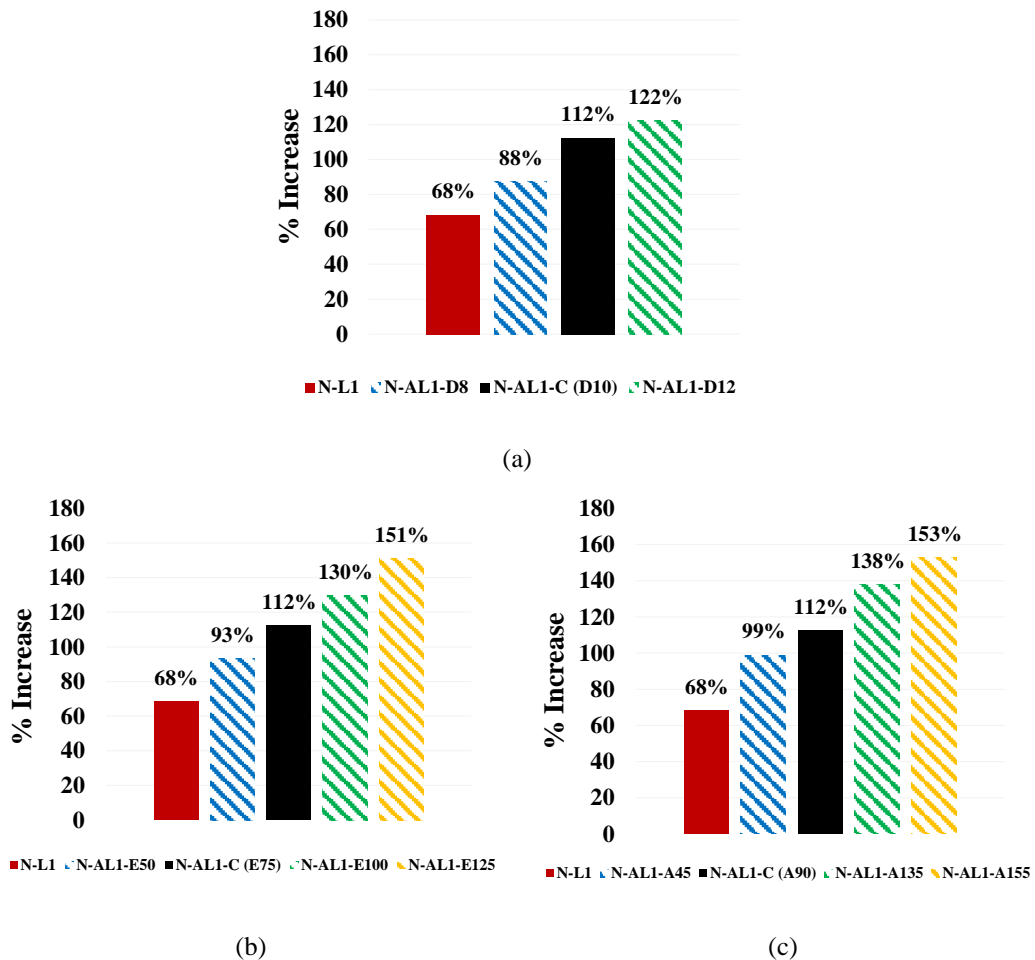
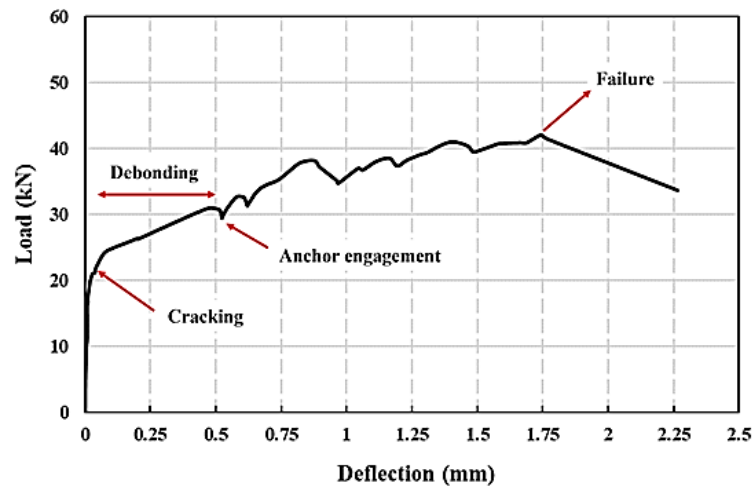


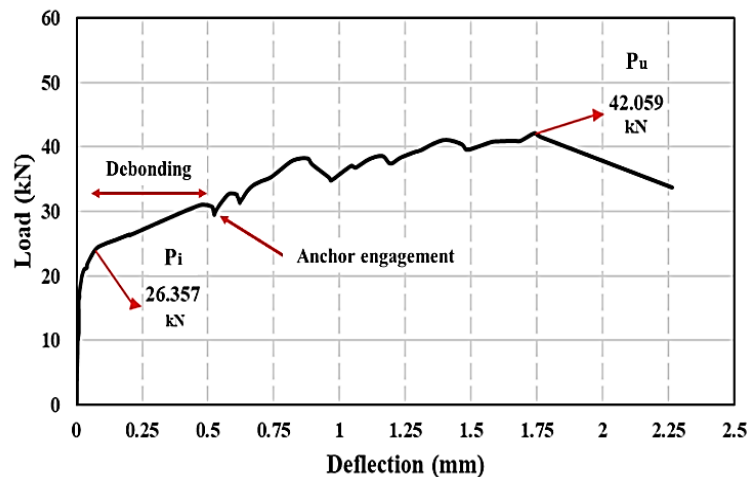
Figure 47: Percentage increase in terms of ultimate load capacity compared to unstrengthened prisms: (a) Anchor dowel angle group; (b) Anchor embedment depth group; (c) Anchor dowel angle group.

All load versus midspan deflection responses of strengthened prisms had a stiff linear segment reaching to the point that indicates the start of flexural cracking in concrete, followed by the increase in load with deflection due to engagement of CFRP laminates in carrying tension loads, then debonding progressively from the concrete substrate. Debonding initiated at the midspan flexural crack and propagated toward the anchors. As soon as it reached the anchors, they got engaged completely by resisting most of the tension force coming from the CFRP laminate, consequently delaying debonding failure. At that stage, the load-deflection response became mostly linear until reaching the ultimate load value and then dropped down suddenly indicating brittle failure mode.

These stages are illustrated in Figure 48a for a typical load-deflection response. The first stage is the flexural cracking stage where the prism cracks at the flexural region at cracking load ( $P_1$ ) when the CFRP laminate started to engage to resist tensile forces. Then, FRP sheets start resisting, and debonding is initiated; hence anchor engagement takes place. FRP reinforcement and anchors delay the failure, so the graph ascends till reaching the ultimate failure load ( $P_u$ ), then a sudden drop is observed. An example of the locations of the cracking load and failure load locations on the load-deflection graphs for the control prism N-AL1-C are explained in Figure 48b.



(a)



(b)

Figure 48: Typical load deflection response.

### 5.2.1. Effect of anchor dowel diameter

Three dowel diameters were considered in this study: 8-, 10-, and 12-mm. Test results in Table 10 show that increasing the diameter from 8 mm to 10 mm significantly increased the capacity; however, when comparing 10 mm and 12 mm diameter, it can be seen that there was not much enhancement. Furthermore, increasing the dowel diameter shows a trend in terms of increasing the capacity of the strengthened prisms. As shown in Figure 49, using 8 mm dowel angles slightly increased the capacity by 11%, compared to unanchored prisms (N-L1), which indicates that the dowel area of  $50.27 \text{ mm}^2$  was insufficient to transfer the load and held the sheet to prevent debonding. On the other hand, a percentage increase of 26% and 32% was documented for 10 mm and 12 mm diameters ( $78.54 \text{ mm}^2$  and  $113.10 \text{ mm}^2$  dowel area), respectively compared to the unanchored prisms (N-L1), which shows that larger dowel areas are required to increase the capacity and delay failures. This indicates that the AMR should be above 2 to ensure the effectiveness of the anchored laminates. This point is proved since prism with dowel diameter of 12 mm failed by middle sheet debonding with no anchor failure; however, the 8mm and 10 mm dowel diameter prisms failed by anchor rupture prior to sheet debonding. One of the factors that could affect structure with different anchor diameters is the hole diameter. Manufacturers suggest an extra 2-3 mm of space between the anchor dowel and concrete hole during installation to ensure a good load transfer mechanism and bond strength. Hole diameter is an important variable to determine the effect of the extra space between the anchor dowel and concrete surface on the tensile capacity of the anchor dowels[91] . Based on the drill bit availability, and for consistency purposes, 2 mm extra diameter was drilled for each dowel diameter to ensure a good bond of the impregnated dowel and maintain an increasing trend in the pullout capacity of the anchors. However, Kim and Smith [92] studied the effect of the hole diameter to embedment depth ratio, concluding that increasing that ratio could decrease the pullout capacity.

Ozdemir [91] also studied the effect of hole diameter and concluded that 2 mm free hole space is enough for the epoxy resin to maintain an effective bond with increasing dowel diameters. Furthermore, the holes were drilled and smoothed especially in the location of the transition segment of the anchors. According to Pudleiner et al.[93], drilling the holes with a chamfer radius prevents premature anchor failures and allows CFRP anchors to fully develop the strength of the CFRP laminates.



To sum up, it can be concluded that for a 75 mm embedment depth, anchor dowel diameter of 12 mm resulted in the highest enhancement capacity when compared to unanchored specimen, yet a slight enhancement was observed when compared to the 10 mm diameter. Figure 50 plots the ratios of ultimate load of anchored prism to unanchored prism for each anchor diameter to show the anchoring effect. It can be seen that the efficiency of the anchors was major when increasing the anchor diameter from 8 mm to 10 mm. However, increasing the anchor diameter to 12 mm is not as efficient; a minor increase in the index was obtained. So, more tests should be performed to study the effect of large anchor dowel diameters with varying hole diameters and embedment depths especially in RC beams.

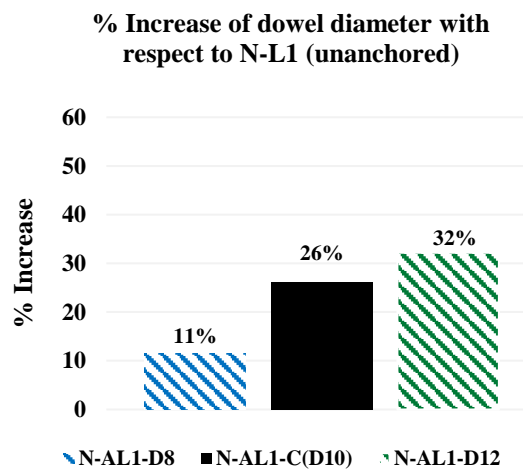


Figure 49: Percentage increase in capacity of anchor dowel diameter group with respect to unanchored prisms (N-L1).

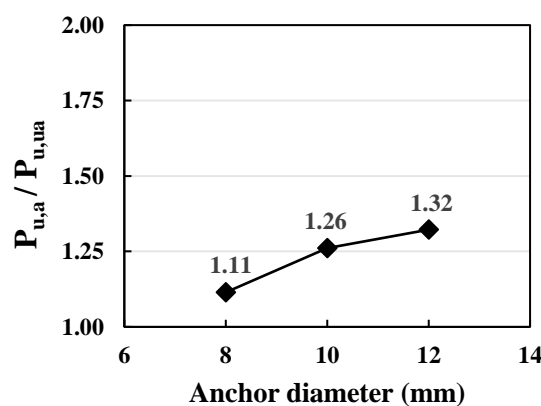


Figure 50: Normalized test results of anchor diameter group.

### **5.2.2. Effect of anchor embedment depth**

Embedment depth is the FRP anchor dowel length embedded into predrilled holes in the concrete. Four anchor embedment depths were examined in this experimental study which are 50-, 75-, 100-, and 125 mm. Based on the results presented in Table 10, it can be concluded that the embedment depth parameter highly effected the behavior and capacity of all anchored prisms, compared to unanchored ones. Also, there is a direct relation between the embedment depth and capacity, where increasing the embedment depths enhanced the capacity of the strengthened prisms. This is due to the increase in the pullout capacity of the anchors when longer embedment depths are installed, as reported in recent studies [55], [94], [95]. Therefore, increasing anchor embedment depths utilized the strength of CFRP laminates and delayed debonding. Some studies [34,38] indicated some limits to embedment depth in which increasing beyond that limit will not improve the strength of FRP dowel-concrete bond; however, it will switch the anchor failure mode from anchor pullout to anchor rupture.

Looking at Figure 51, the depths of 50-, 75-, 100- and 125 mm increased the capacity of the specimens by 15%, 26%, 36%, and 49%, respectively compared to unanchored prisms (N-L1). Thus, anchor embedment depth of 125 mm resulted in a capacity increase by about 30, 18 and 9%, compared to 50-, 75-, and 100mm embedment depths, respectively. Moreover, the minimum embedment depth is calculated by multiplying the anchor diameter by 6 according to current practices. Since 10 mm diameter anchors were used in this group, the minimum embedment depth considered is 60 mm. The findings of this study match these practical measures, as anchors with embedment depths of 50 mm were less effective, compared to highest embedment depths especially 125-mm embedment depth. The anchor efficiency as load ratio for each embedment depth is plotted in Figure 52, showing that anchors' efficiency was increasing with an increase in the depth. The anchors were most efficient with an embedment depth of 125 mm, where the normalized load (ratio of anchored to unanchored) value was 1.50 which is much higher than other recorded indices. However, indices of 50 mm to 100mm embedment depth increased linearly with increasing the depth. Some studies [44], [53] concluded that embedding anchors above 100 mm reduces the tensile capacity of the anchors; however, in this research using an anchor embedment depth of 125 mm increased the capacity further. It is recommended to design CFRP anchors based on the

minimum embedment depth length, especially if anchor diameter varied to utilize the CFRP laminate and prevent debonding failure.

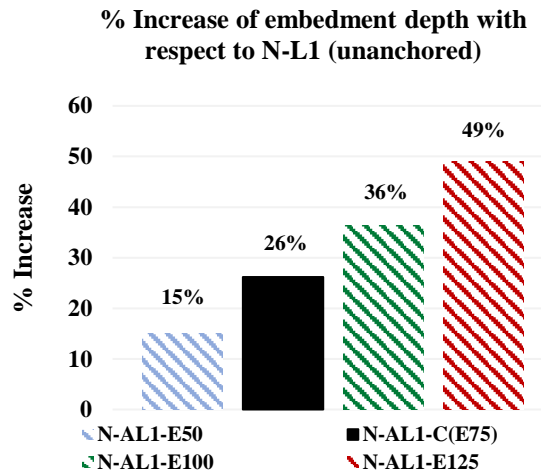


Figure 51: Percentage increase in capacity of anchor embedment depth group with respect to unanchored prisms (N-L1).

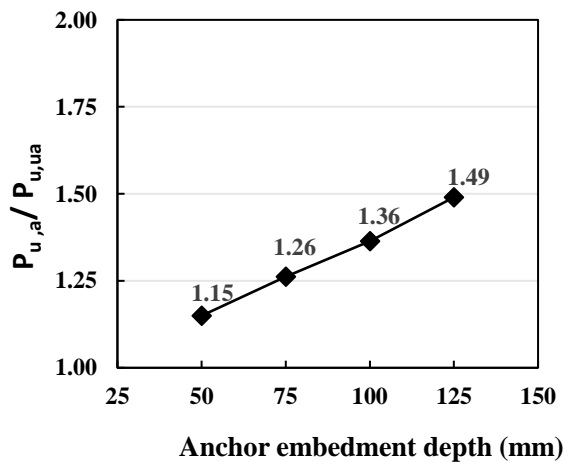


Figure 52: Normalized test results of anchor embedment depth group.

### 5.2.3. Effect of anchor dowel angle

FRP anchor insertion angle is the angle measured anticlockwise from the bottom surface of the prism. Anchor dowel angles of 45°, 90°, 135°, and 155° are examined in this experimental work; a schematic drawing for each anchor dowel angle is shown in Figure 53.

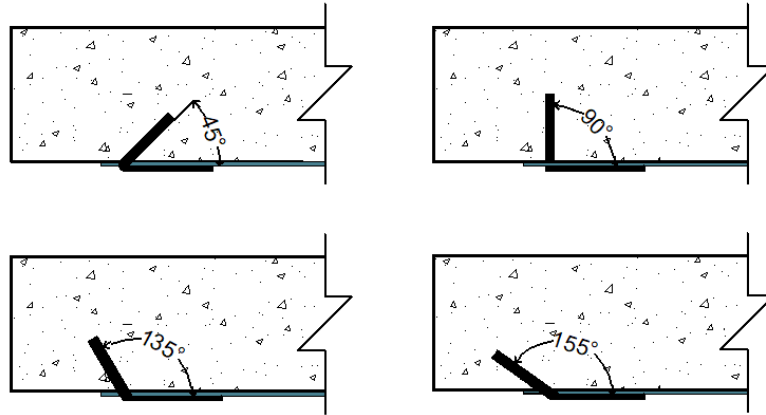


Figure 53:schematic drawing for each anchor dowel angle.

Test results presented in Table 10 showed a direct relation between anchor dowel angle and prism capacity. Specimens with obtuse insertion angles attained higher levels load capacity. Particularly, prisms with anchor dowel angles of  $135^\circ$  and  $155^\circ$  significantly enhanced the load capacities of the prisms compared to smaller dowel angles. The capacity of the previously mentioned angles was increased by 41% and 50%, respectively, compared to N-L1 as illustrated in Figure 54. The ideal prism in this group was N-AL1-A155 with anchor dowel angle of  $155^\circ$  that was the closest to straight anchors ( $180^\circ$ ) with an ultimate load value of 52.63 kN. Moreover, smaller dowel angles also showed minor enhancements compared to obtuse angles; N-AL1-C with  $90^\circ$  dowel angle increased the capacity of the strengthened prisms by 26% compared to N-L1. The least flexural enhancement was noticed in specimen N-AL1-A45 that was anchored with  $45^\circ$  anchors with an enhancement percentage compared to the unanchored strengthened specimen N-L1 of only 18%, implying that anchors closer to straight anchors are more effective than smaller angle anchors. The behavior of prisms in this group refers to the significant increase in pullout capacity of anchors with obtuse ( $\beta > 90^\circ$ ) angles, compared to acute ( $\beta < 90^\circ$ ) and vertical ( $\beta = 90^\circ$ ) angle, as reported elsewhere [71]–[74]. Moreover, it is observed that obtuse insertion angles increased the anchor strength, where a linear relationship was established between the insertion angle ( $\beta$ ) and strength. Obtuse angles resulted in higher capacity since they are close to the  $180^\circ$  dowels that resist the tensile stress transferred from the sheet. Also, the insertion angle ( $\beta$ ) controls the deformation capacity of the FRP structure, where larger deformations were observed with increasing the dowel angle ( $\beta$ ) especially above  $90^\circ$ . Similar conclusions were mentioned in a study by Zhang and Smith [78].

The strength of the joint increased as the anchor dowel angle increased relatively away from the load. Increasing anchor dowel angle has a major effect on the load carrying capacity of the structure, and this is demonstrated in Figure 55. It can be observed that anchors with obtuse angles were the most efficient showing high load ratio values of 1.44 and 1.55, respectively. The efficiency difference between the 45° and 90° was not major; however, a drastic increase was seen in anchor efficiency when increasing the anchor dowel angle from 90° to larger angles. Nevertheless, it is recommended to design inclined dowel anchors based on the provided depth and design requirements especially that drilling with an angle can be challenging in most structures.

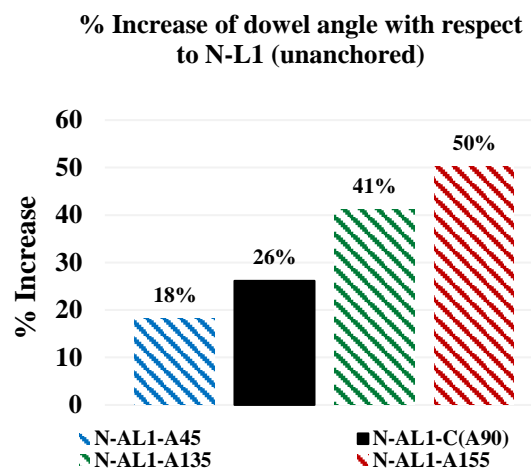


Figure 54: Percentage increase in capacity of anchor dowel angle group with respect to unanchored prisms (N-L1).

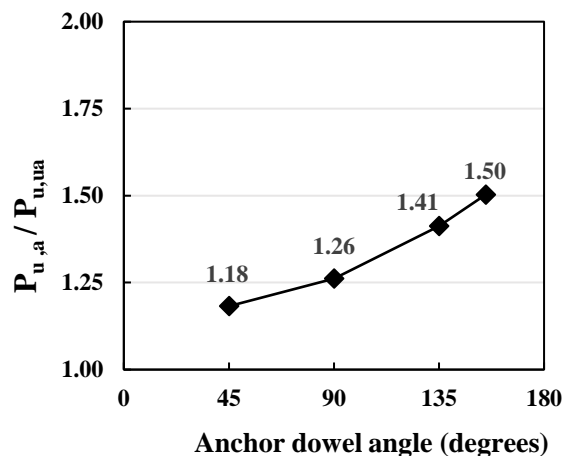


Figure 55: Normalized test results of anchor dowel angle group.

## Chapter 6. Bond-slip Models Results

In this chapter, bond-slip models are established to study the interface debonding due to flexural cracking of concrete beams strengthened with anchored CFRP laminates. The stress deformation is generally known as bond-slip relationship since the deformation in the interface is referred as the displacement (slip) between the laminate and the concrete. External load was applied leading to the development of interfacial shear stress along the FRP-concrete interface. When the load is high enough for the strengthened prism, debonding initiates at the interface causing premature failure of the strengthened prism beam [98]. It should be noted that the term “interface” used in this research refers to the interfacial bonded joint between the CFRP laminate and the concrete substrate including the adhesive which is responsible for the relative slip between the CFRP laminate and the concrete prism.

Bond stress versus slip bilinear relationships are attained experimentally to study the load-transfer mechanism from CFRP laminate to the concrete substrate and anchors. The debonding process of the bilinear bond-slip model can be described by different stages. The first stage introduces an elastic behavior due to flexural cracking where a minor slip occurs between the FRP and concrete at the location of the flexural crack; hence the bond stress concentration is established at the location of the crack. The maximum interfacial bond stress at that stage is less than the maximum bond stress. The second stage refers to the interfacial softening stage where the bond stress has reached its maximum value with the corresponding slip value and starts to decrease afterwards indicating the presence of concrete cracking and the propagation of debonding along the laminate. The final stage is the stage where the ultimate load and maximum slip value is met leading debonding failure and is referred as the failure stage [71], [72], [98].

The relation between bond stress and slip was extracted from the test data. Bond forces generate the change in the tensile force of the CFRP laminate to the interface layer between the laminate and the concrete substrate. Bond stress and slip distributions are calculated from strain measurements along the laminate. The bond shear stress between two consecutive gauge positions can be obtained by equilibrium of forces and compatibility equations. The equilibrium of bond/shear stress considers the normal

stresses  $\sigma_f$  and  $\sigma_f + d\sigma_f$  and shear stresses  $\tau(x)$  along a segment length  $d_x$  of the CFRP laminate, assuming linear elastic behavior till failure and is written as[99]–[102] :

$$n_f t_f d\sigma_f = \tau(x) dx \quad (55)$$

$$\text{where, } d\sigma_f = E_f d\varepsilon_f \quad (56)$$

Combining these (Eqs.55 and 56) will give the following bond shear stress equation:

$$\tau(x) = n_f t_f E_f d\varepsilon_f / dx \quad (57)$$

Since strain gauges are distributed at a segment of the CFRP laminate, Eq.57 is rewritten in a discrete manner to include the strain values obtained as shown in Eq.58:

$$\tau(x_i) = \frac{1}{2} n_f t_f E_f \left[ \frac{(\varepsilon_i - \varepsilon_{i-1})}{(x_i - x_{i-1})} + \frac{(\varepsilon_{i+1} - \varepsilon_i)}{(x_{i+1} - x_i)} \right] \quad (58)$$

where:

$\tau(x_i)$  : local bond/shear stress at different locations  $x$  (MPa).

$n_f$  : number of CFRP laminate ply.

$t_f$  : thickness of CFRP laminate (mm).

$E_f$  : modulus of elasticity of CFRP sheet (MPa).

$\varepsilon_i$  : strain reading from  $i^{\text{th}}$  strain gauge ( $\mu\varepsilon$ ).

$x_i$  : location of the  $i^{\text{th}}$  strain gauge (mm).

The cumulative slip between the concrete and CFRP laminate is the change in the slip value with the change in the segmental distance which is derived considering the FRP deformation and concrete deformation that could be neglected with respect to the FRP deformation. Therefore, integrating the FRP deformation(Eq.59) with respect to the segmental distances is computed as in Eq.60. Then, considering the strain gauges along the segment, Eq.60 is rewritten as to calculate the cumulative slip along the proposed segmental distance (Eq.61).

$$\frac{ds}{dx} = \varepsilon_f - \varepsilon_c \quad (59)$$

$$s(x) = s(0) + \int_0^x \varepsilon_f(x) dx \quad (60)$$

$$s(x) = s(0) + \sum_{i=n}^i \frac{1}{2} [(\varepsilon_i - \varepsilon_{i-1})(x_i - x_{i-1}) + (\varepsilon_{i+1} - \varepsilon_i)(x_{i+1} - x_i)] \quad (61)$$

where:

$\varepsilon_c$ : concrete deformation.

$\varepsilon_f$ : FRP deformation.

$s(x)$ : slip at distance x (mm).

$s(0)$ : local slip at maximum bond/shear stress (mm).

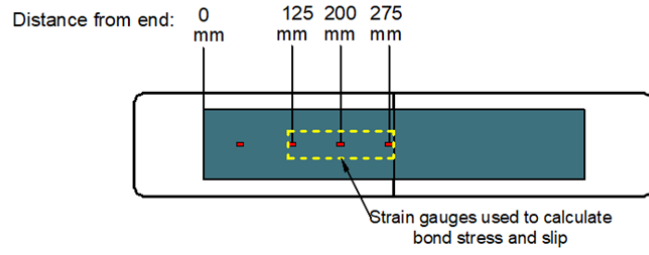
$s(l)$ : slip at end of bonded length (mm).

$n$ : total number of strain gauges.

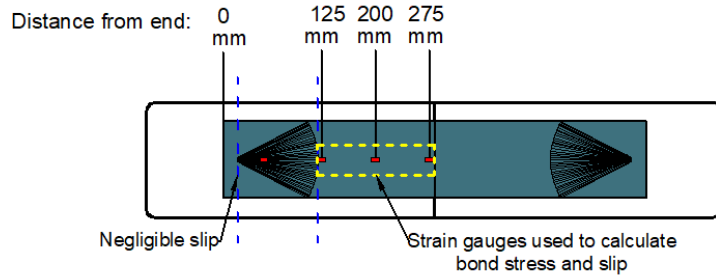
There is still a lack in literature for the study of bond/ shear stress and slip analysis for anchored strengthened structures with different anchor parameters. Bond stress-slip, bond stress-distance, and slip-distance plots will be presented in this chapter for all anchor parameters studied in this research in order to show the effect of each parameter on the load transfer mechanism from the CFRP laminate to the concrete and anchors. The order and location of the strain gauges of anchored and unanchored prisms are illustrated in Figure 56.

The slip on the anchors is negligible since there is no slip at that point due to anchoring effect that holds the sheet, so the strain gauges used to calculate bond stress and slip are the ones placed on the laminate only. To be consistent, the same strain gauge locations were used for unanchored prism. Moreover, maximum bond stress ( $\tau_{max}$ ), slip at maximum bond stress ( $S_0$ ), maximum slip ( $S_{max}$ ) and their normalized values are presented in Table 13. Figures 57 and 58 plot the normalized ratios (ratio of anchored to unanchored) for the maximum bond stress and maximum slip, showing the effect of each anchor parameter. Also, percentage increase of  $\tau_{max}$  and  $S_{max}$  is shown in Figures 59 and 60.





(a)



(b)

Figure 56: Strain gauges used for bond stress and slip models: (a)unanchored prism; (b)anchored prism.

Table 13: Maximum bond stress and slip values.

Prism	$\tau_{max}$ (MPa)	$S_0$ (mm)	$S_{max}$ (mm)	$\frac{\tau_{max,a}}{\tau_{max,ua}}$	% Increase of $\tau_{max}$ with respect to N-L1	$\frac{S_{max,a}}{S_{max,ua}}$	% Increase of $S_{max}$ with respect to N-L1
N-L1	1.43	0.25	0.43	-	-	-	-
N-AL1-C	3.65	0.54	0.89	2.56	156	2.06	106
N-AL1-D8	2.03	0.43	0.66	1.42	42	1.53	53
N-AL1-D12	4.22	0.60	0.99	2.96	196	2.29	129
N-AL1-E50	3.25	0.27	0.46	2.27	127	1.06	6
N-AL1-E100	3.74	0.99	0.99	2.62	162	2.27	127
N-AL1-E125	6.23	1.00	1.00	4.36	336	2.31	131
N-AL1-A45	2.69	0.48	0.48	1.89	89	1.11	11
N-AL1-A135	4.13	0.65	1.07	2.89	189	2.46	146
N-AL1-A155	5.70	0.57	1.02	3.99	299	2.35	135

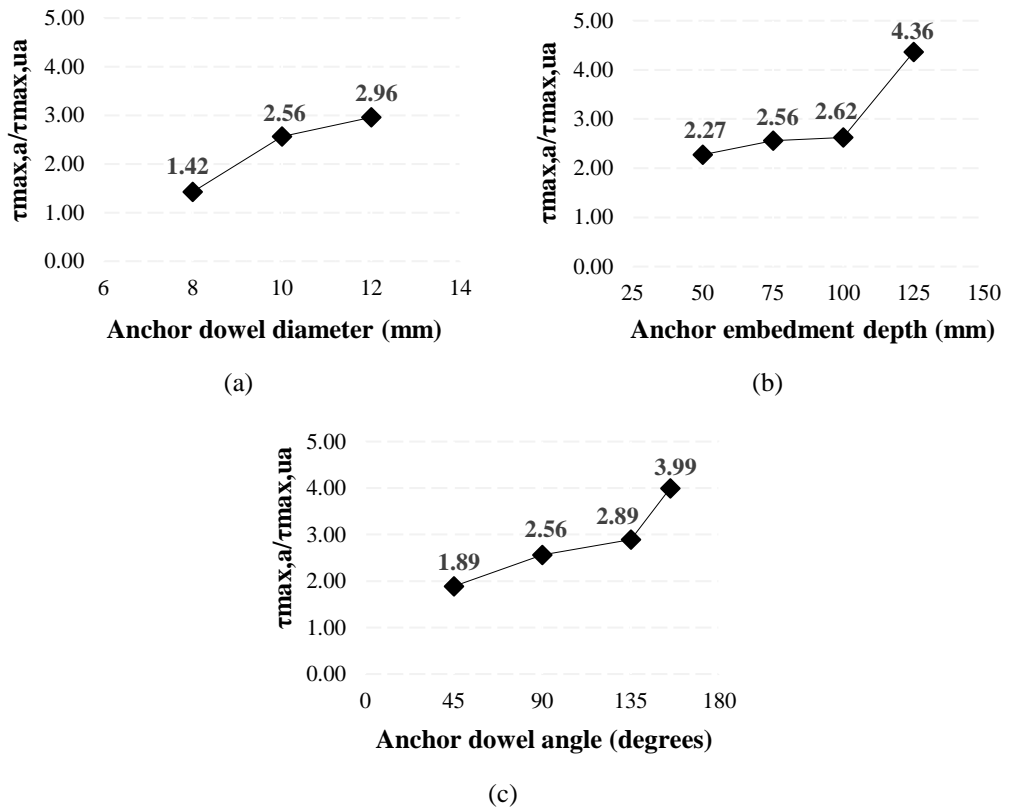


Figure 57: Normalized maximum bond stress values for different anchor parameters.

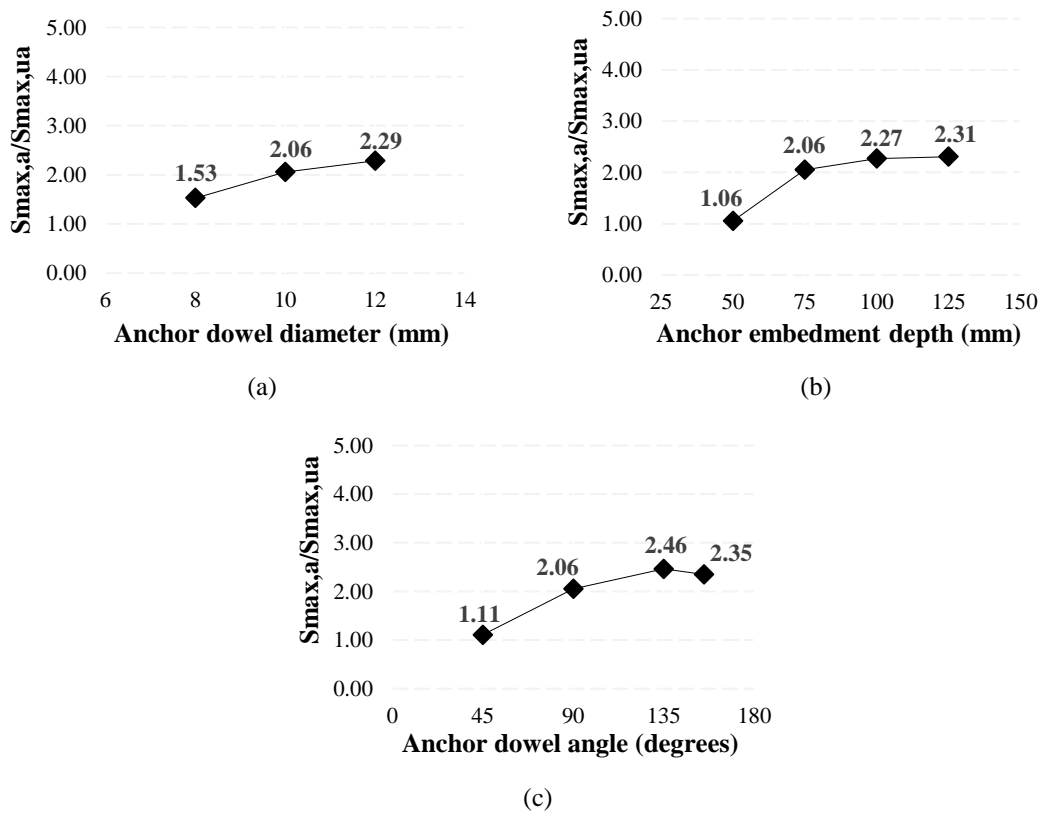


Figure 58: Normalized maximum slip values for different anchor parameters.

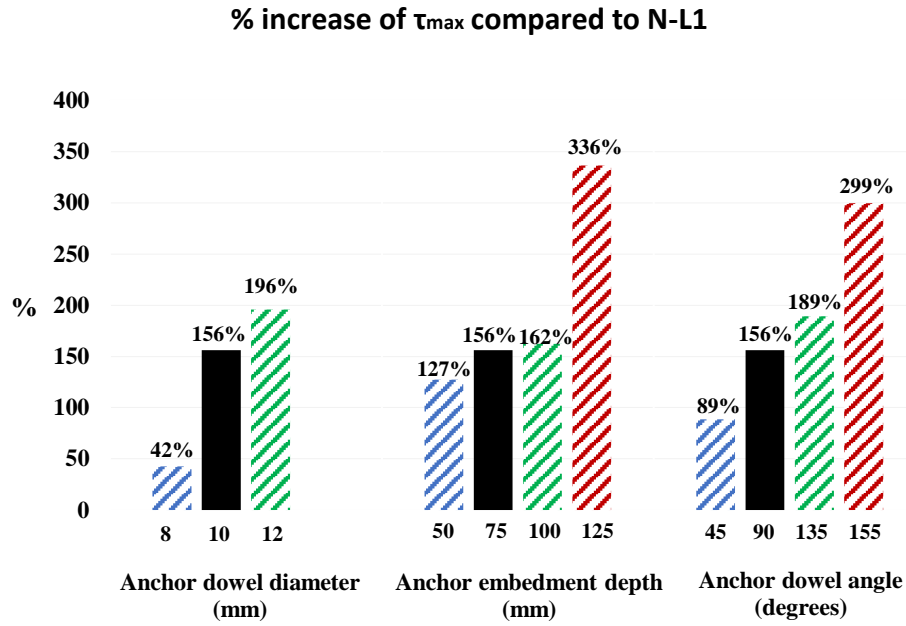


Figure 59: Percentage increase of  $\tau_{max}$  compared to N-L1

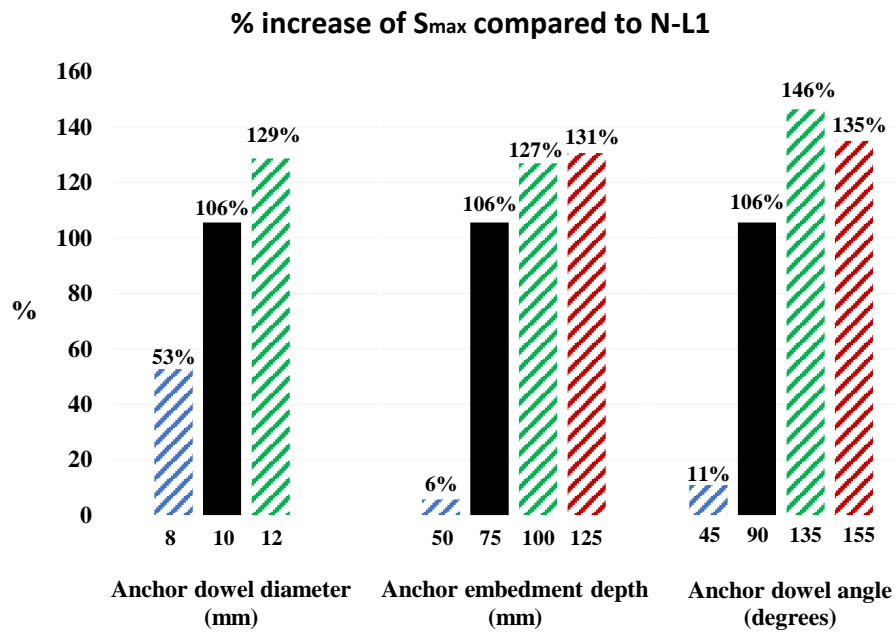


Figure 60: Percentage increase of  $S_{max}$  compared to N-L1.

### 6.1. Bond stress and slip models of control group

This group compares the bond stress and slip of unanchored prism N-L1 with the control anchored prism N-AL1-C. It can be observed that the anchored prism had higher values of bond stress and slip. Both had the maximum bond stress at the ultimate load level and failed after the descending part of the graph. However, the descending part,

indicating the stage after microcracking and the start of debonding, was not observed in the first load level of both graphs. Looking at Figure 61a, the debonding started at an earlier stage at the second load level (40%) where the last 2 plotted bond stress values were close to each other. After that, the descending part of the graph was clearly observed indicating that the bond stress started to drop down closer to failure with the increase of slip values directly after the flexural cracking stage. Furthermore, the anchored prism (Figure 61b) showed a better behavior in terms of delaying debonding and increasing bond stress value, where a clear drop in bond stress values occurred at the last load level with the increase in slip. Two full distinct portions of the stress curve including ascending and descending portions were developed at the last load level indicating that full bond strength was utilized at 100% of the ultimate load. This means that the anchors utilized the CFRP laminates and hence increased the load capacity of the prism and the bond strength between the FRP and concrete.

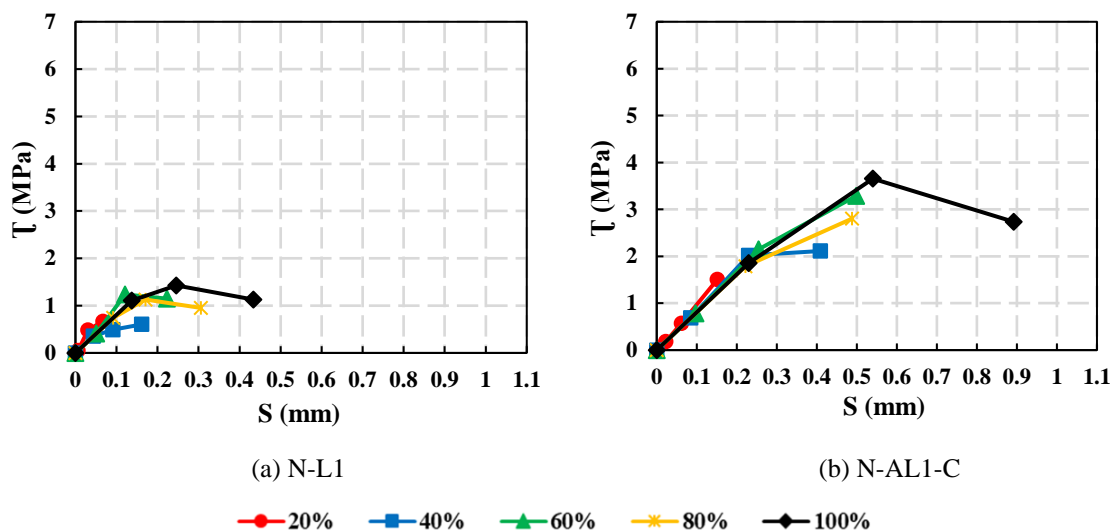


Figure 61: Bond stress-slip models of control group at different load levels.

Figure 62 shows the bond stress distribution versus distance for the control specimens at different load levels. The bond stress at the failure load showed the highest stress values along the sheet distance. As getting closer to the center, the stress increases in N-L1. However, N-AL1-C has the maximum stress value at the middle strain gauge location due to the anchorage effect, so lower bond stress value was obtained from the strain gauge beside the anchor. Furthermore, the slip versus distance graphs (Figure 63) shows a direct relation between the slip values and the increase of the distance from the end. The slip increases when getting closer to the center of the prism due to getting farther from the anchor that reduces the slippage effect. Also, the laminate segment

closer to the applied load is more vulnerable to slip. Similar graph shapes were obtained in strain versus distance graphs shown previously.

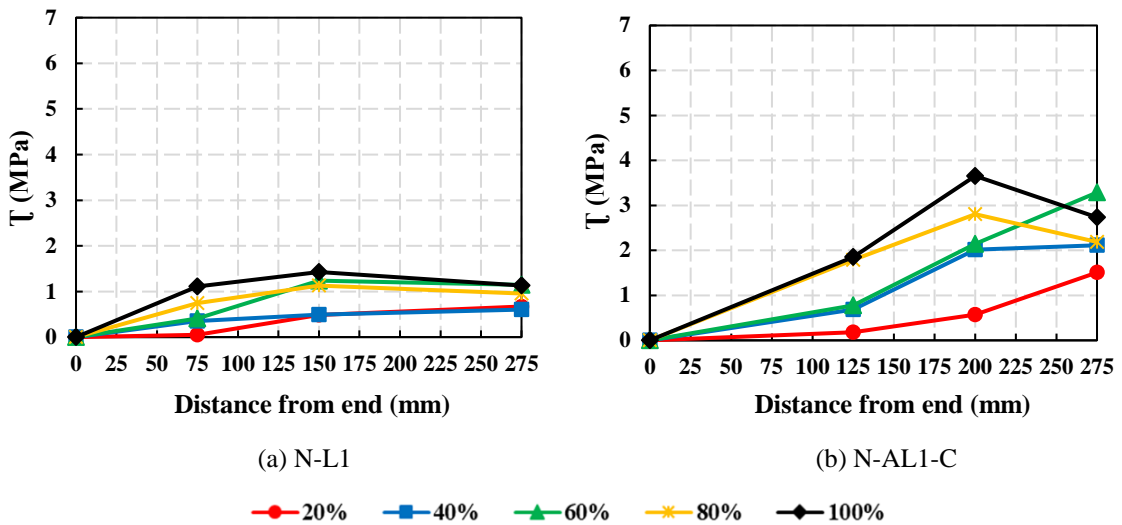


Figure 62: Bond stress vs. distance of control group at different load levels.

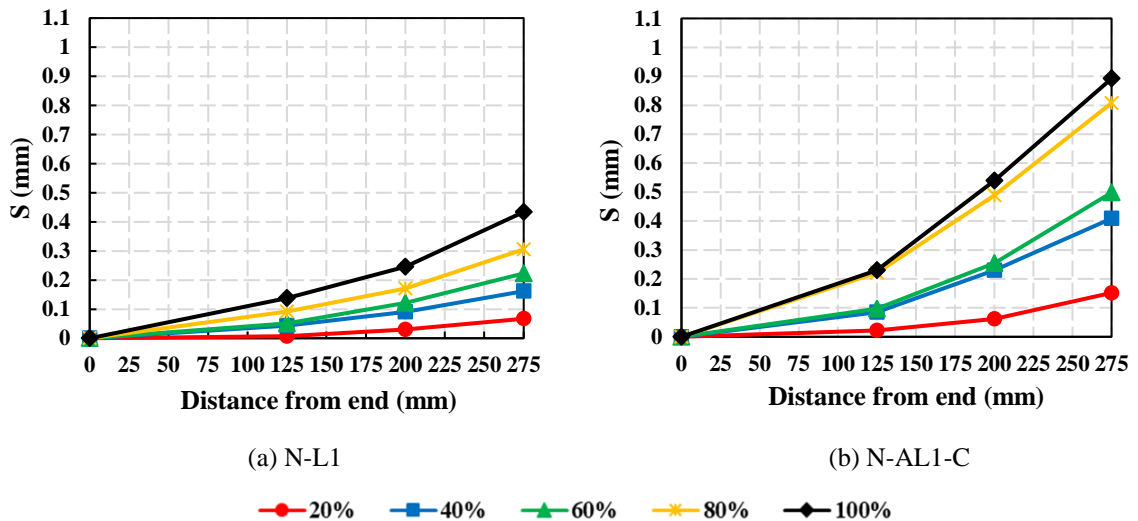


Figure 63: Slip vs. distance of control group at different load levels.

## 6.2. Bond stress and slip models of anchor dowel diameter group

The bond stress-slip graphs (Figure 64) of anchor dowel diameter group demonstrate that increasing the anchor diameter increased the maximum bond stress value. N-AL1-D8 had a  $\tau_{max}$  value of 2 MPa with a corresponding  $S_0$  of 0.43mm and  $S_{max}$  of 0.66 mm. Comparing N-AL1-C (D10) and N-AL1-D12 shows that increasing the anchor diameter from 10 mm to 12 mm resulted in a minor increase in bond stress and slip values. The maximum calculated  $\tau_{max}$  values were 3.65 and 4.22 MPa with corresponding  $S_0$  values of 0.54 and 0.6 mm, respectively. All prisms of this group

failed after the descending branch of the graph; however, the slope of the descending part of the prism with 8 mm anchor diameter was the highest, meaning that the development of debonding failure was major compared to other diameters. Also, ascending, and descending portions were clearly developed in the last three load levels of prisms with 8 mm and 12 mm anchor diameter, demonstrating that full bond length was utilized.

Bond stress versus distance graphs is illustrated in Figure 65. Bond stress of N-AL1-D8 was increasing linearly at the first two load levels, then started to decrease as getting closer to the center, so the stress concentration was maximum at the middle of the examined bonded length and then decreased at the center of the prism at later load levels, indicating that debonding has propagated throughout the laminate causing failure. A similar behavior was observed with other prisms of this group, and all prisms had their  $\tau_{max}$  values at ultimate load since the failure afterwards was sudden. Figure 66 shows the plots of slip versus distance; Figure 66a shows that the slip values significantly increased after the cracking load and got closer at the last 3 load levels. This explains that the 8 mm anchor diameter was not effective much in delaying debonding failure and improving the load transfer mechanism to the concrete, leading to a major increase in slip values after flexural cracking (40%  $P_u$ ). Moreover, the slip values of N-AL1-D12 were increasing with higher slip intervals at each loading stage, indicating that the anchor was delaying debonding until ultimate load was reached.

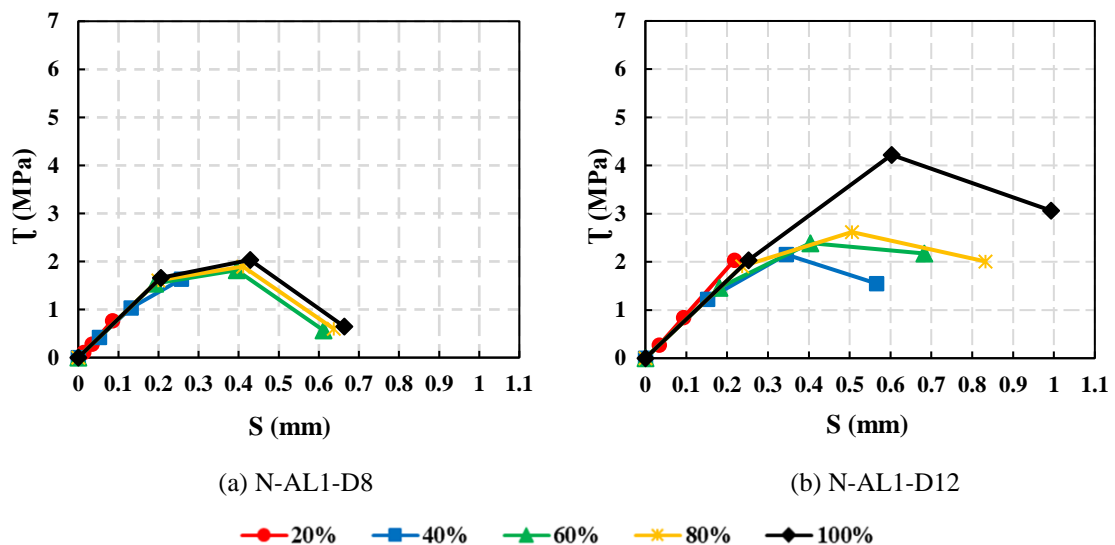


Figure 64: Bond stress vs. slip of anchor dowel angle group at different load levels.

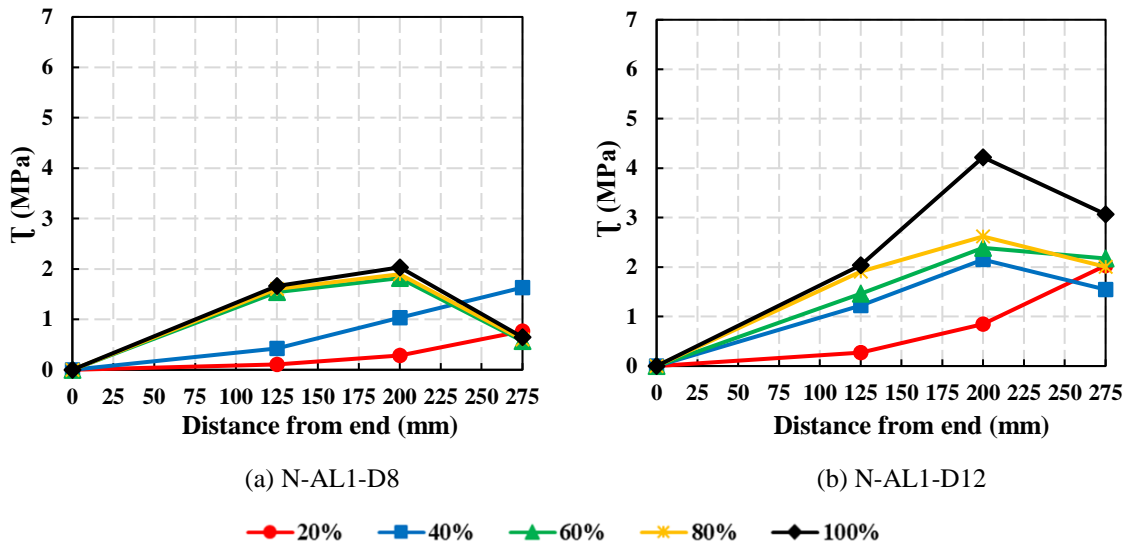


Figure 65: Bond stress vs. distance of anchor dowel angle group at different load levels.

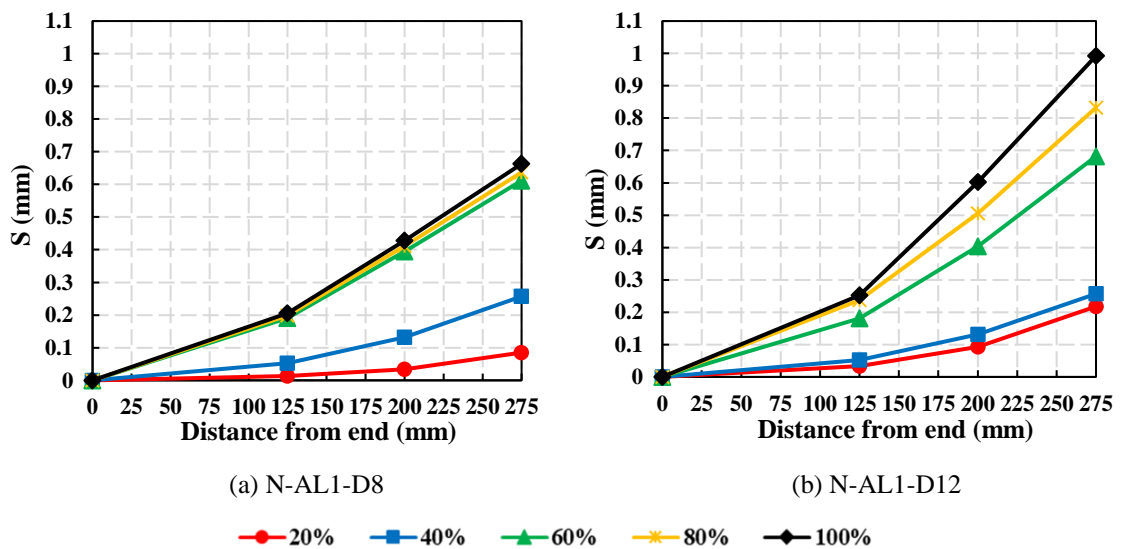


Figure 66: Slip vs. distance of anchor dowel angle group at different load levels.

### 6.3. Bond stress and slip models of anchor embedment depth group

Bond stress-slip of different anchor embedment depths presents different patterns in the bond-slip models. As shown in Figure 67a, embedding the anchors with 50 mm depth resulted in clear ascending and descending parts, implying that as the force in sheet increased, the stress was developed completely in the laminate at lower bond stress values compared to larger embedment depths, leading to complete debonding failure with a clear drop in bond stress. Therefore, 50 mm embedment is not enough for anchors to be active transferring the load to the concrete effectively, thus delaying debonding. On the other hand, Figures 67b and c for prisms with larger anchor embedment depths show only an ascending branch, meaning that the failure occurred

at maximum bond stress and corresponding slip values before reaching the descending branch. Comparing these prisms with N-AL1-C(E75), it can be seen that as a result of increasing the load, an ascending branch was developed with a gentle descending branch before failure. So, increasing embedment depth decreases the effect of bond stress drop and leads to failure closer to the maximum bond stress value. This indicates that large embedment depths are enough and efficient with respect to the proposed bonded length for the transfer of bond stress and load through the laminate. The maximum bond stress  $\tau_{max}$  calculated for embedment depths of 50-, 75-, 100- and 125 mm were 4.09, 3.65, 3.74, and 6.22 MPa with corresponding  $S_0$  values 0.34-, 0.54-, 0.99- and 1 mm, respectively. Furthermore, bond stress versus distance graphs is shown in Figure 68 indicating the locations of the calculated bond stresses at each load level.

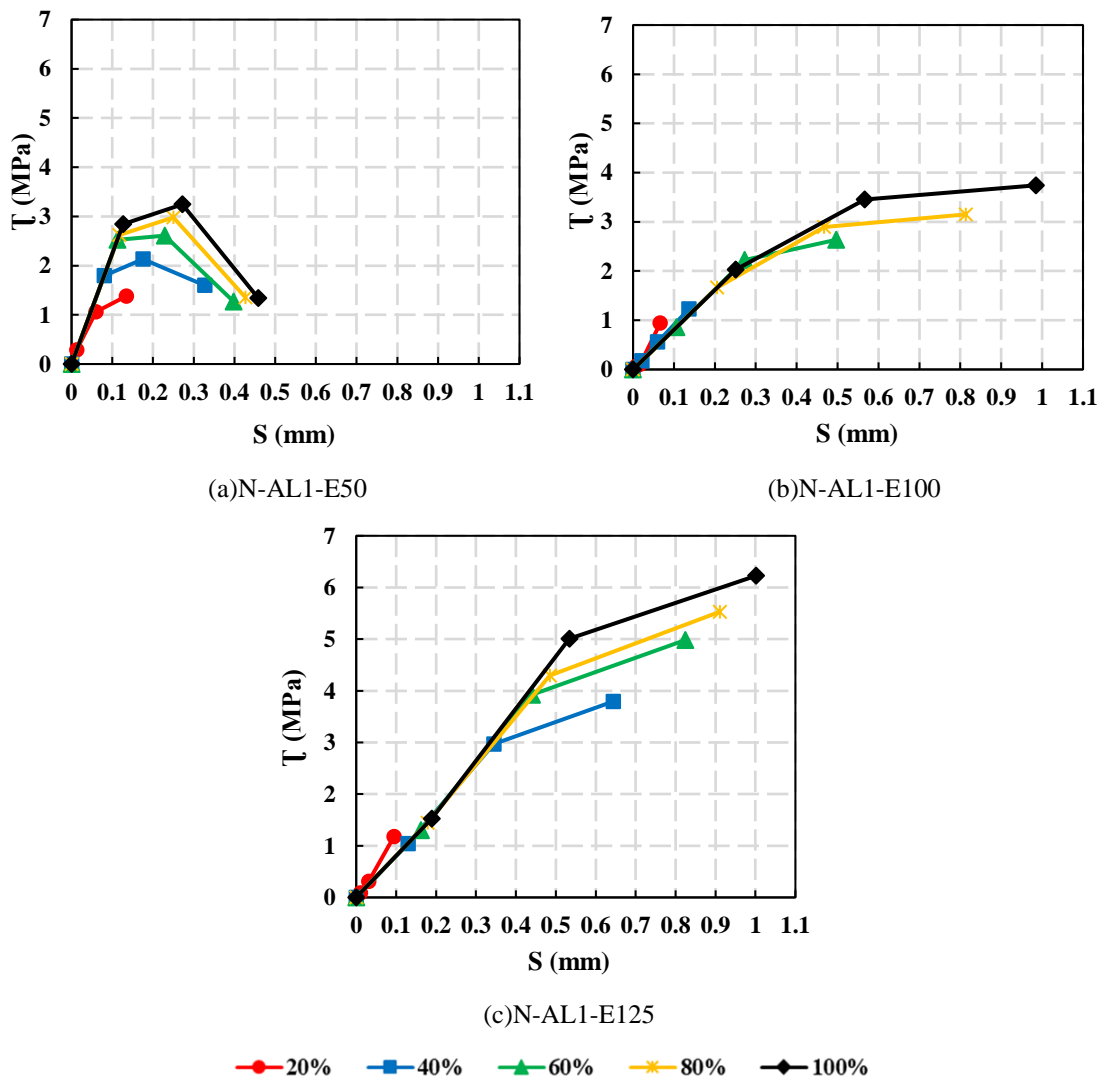


Figure 67: Bond stress vs. slip of anchor embedment depth group at different load levels.



It is observed that the maximum stress was located at the middle of the studied bonded length in N-AL1-E50, where it increases as moving towards the center of the bonded length until reaching a maximum value, and then decreases again at the loaded portion. However, the maximum stresses in N-AL1-E100 and N-AL1-E125 at ultimate load level were located at the center of the prism and approached zero at the end of the sheet due to the good anchoring effect. Figure 69 illustrates the plots of slip versus distance for all prism of that group. Figure 69a shows that the slip values significantly increased after the first load level and got closer after. Therefore, 50 mm embedment depth was not efficient enough in delaying debonding failure since it allowed a fast increase in slip after 20% only of the ultimate load. Moreover, the slip values of larger embedment prisms (Figures 69b and c) were increasing gradually at each loading stage towards the center, implying that the anchors were effective in delaying debonding.

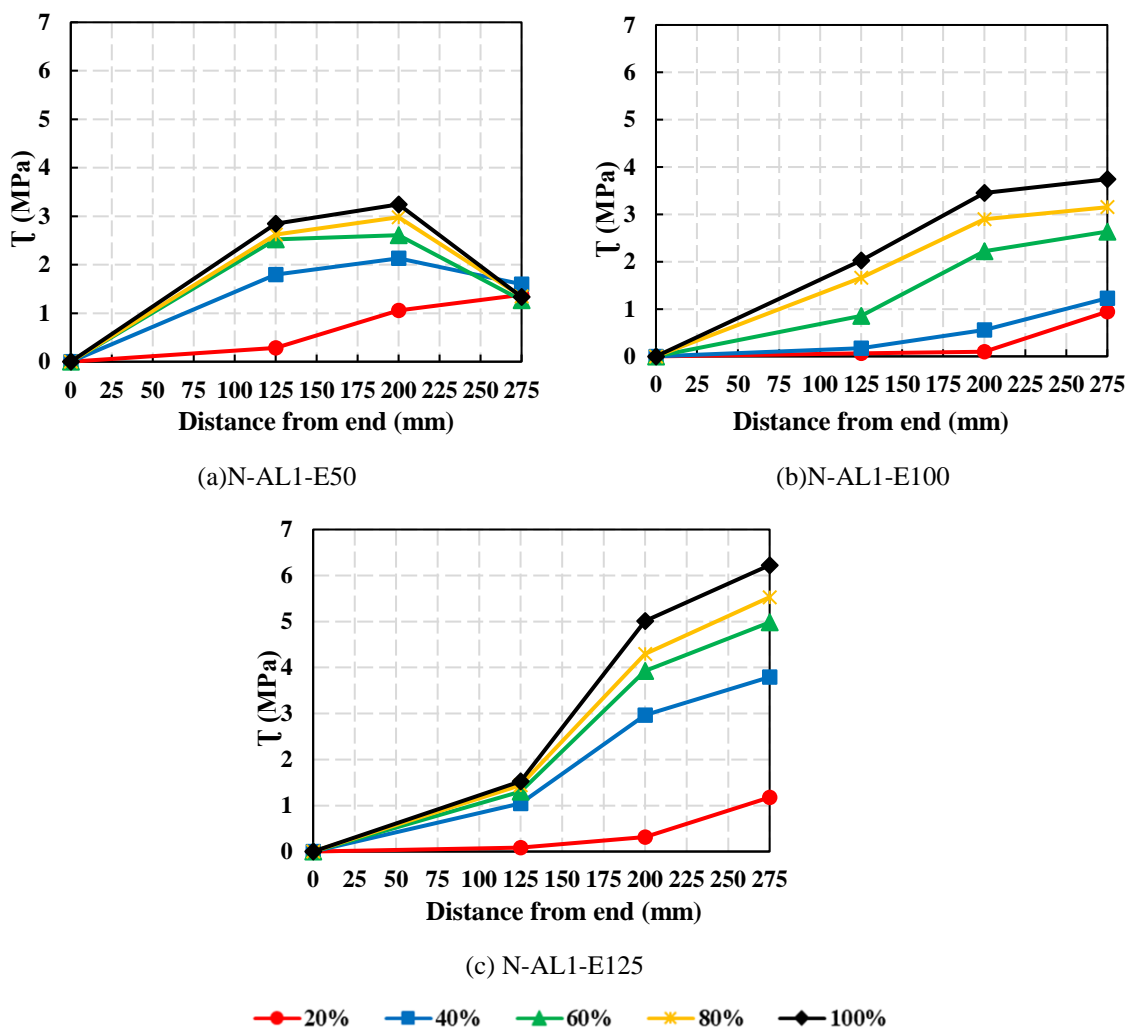


Figure 68: Slip vs. distance of anchor embedment depth group at different load levels.

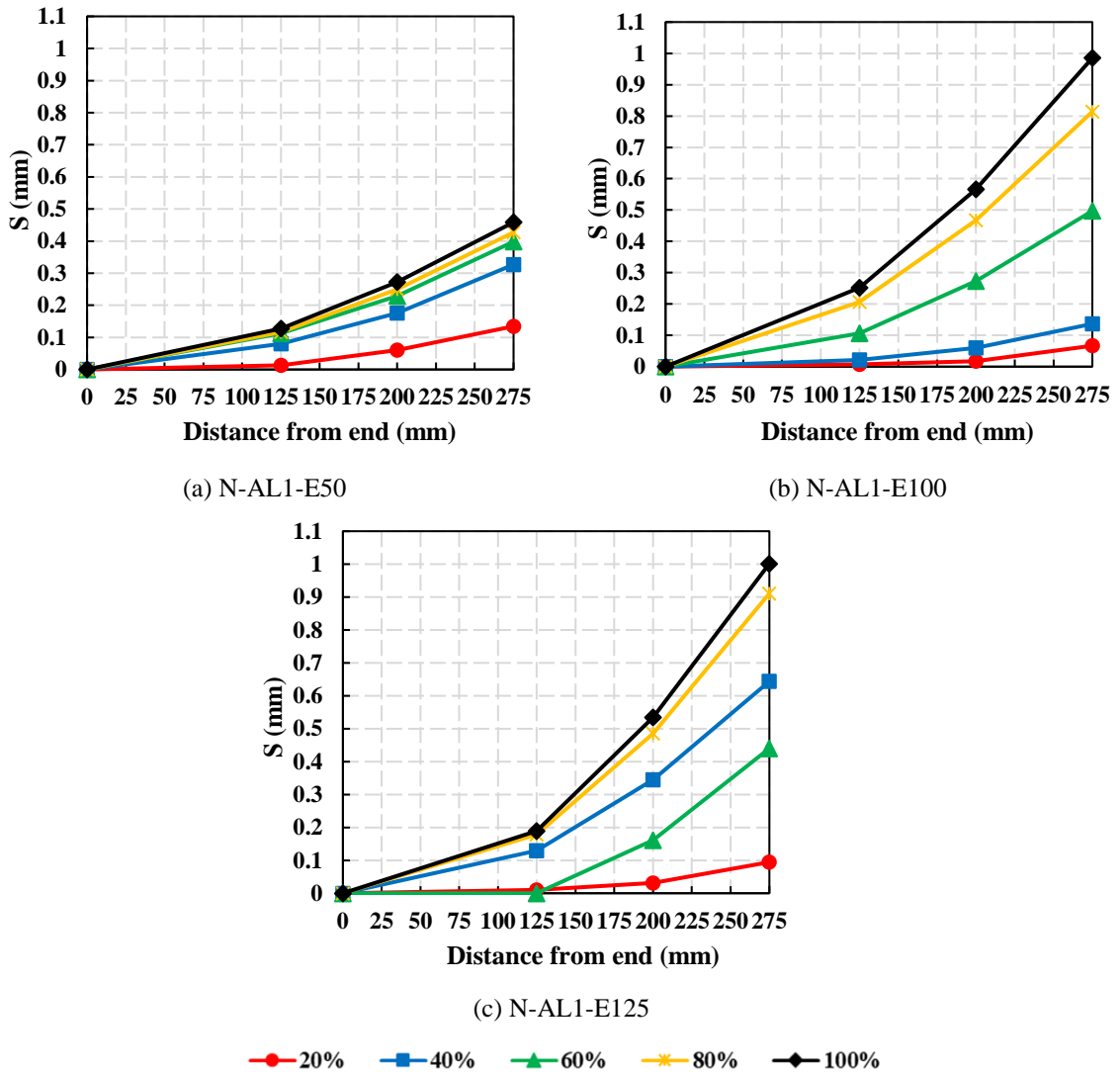


Figure 69: Slip vs. distance of anchor embedment depth group at different load levels.

#### 6.4. Bond stress and slip models of anchor dowel angle group

Anchor dowel diameter group revealed different bond-slip model; Figure 70 presents the models of dowel angle  $45^\circ$ ,  $135^\circ$  and  $155^\circ$ . As illustrated in Figure 70a for N-AL1-A45, a gentle descending branch was plotted at each load level except at the ultimate load level where  $\tau_{max}$  (at the last point of its ascending branch) was 2.69 MPa with corresponding maximum slip of 0.48 mm ( $S_0 = S_{max}$ ). Figure 70b shows the bond-slip models of the obtuse angle  $135^\circ$ ; the descending branch of the model was observed at ultimate load. Moreover, Figure 70c demonstrates that increasing the angle to  $155^\circ$  increased the bond stress significantly with a corresponding slip value close to the maximum slip of  $135^\circ$ . This explains that embedding the anchors at  $155^\circ$  angle was the most effective in terms of transferring the load where the bond stress was transferred along the laminate and increased as moving away from the anchors. The results reported

herein demonstrate that the bond shear stress ( $\tau$ ) increased with an increase in slip in all prisms of this group. The descending branch is not observed in the 45° anchored prism at the ultimate load level. However, a descending branch is observed in the 135° and 155° anchored prism at the last load level, which means that the bonded length was developed at the ultimate load level.

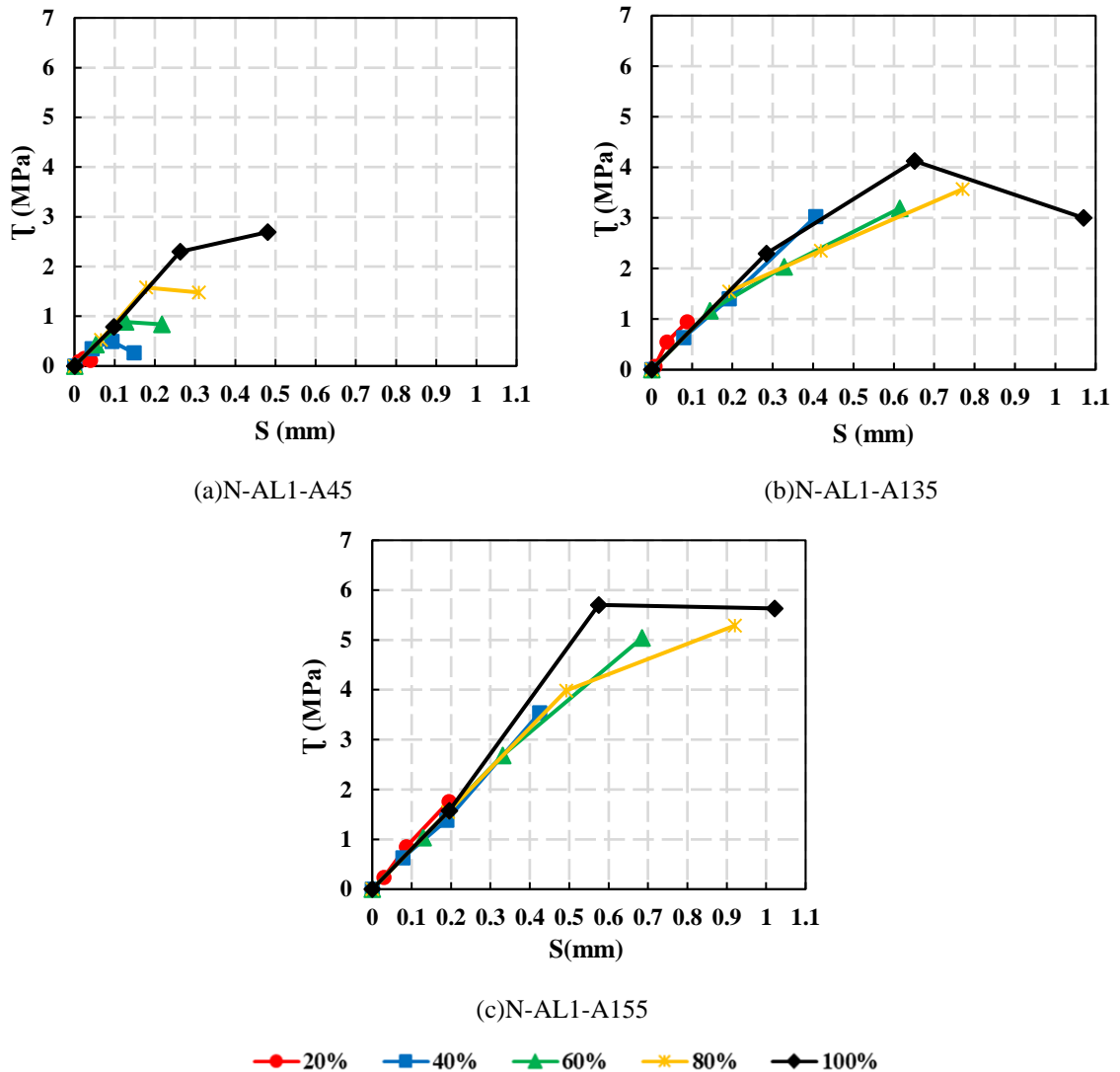


Figure 70: Bond stress vs. slip of anchor dowel angle group at different load levels.

Figure 71 presents the bond stress versus distance plots of this group, showing that bond stress values were increasing as moving towards the center of the prisms. Calculated  $\tau_{max}$  values of this group were 2.69, 4.12, and 5.70 MPa with corresponding  $S_0$  values of 0.48-, 0.65- and 0.57 mm respectively. Therefore, increasing the dowel angle especially above 90° had the most effective results in terms of increasing bond strength

between the concrete and CFRP laminate developing the load transfer mechanism along the interface.

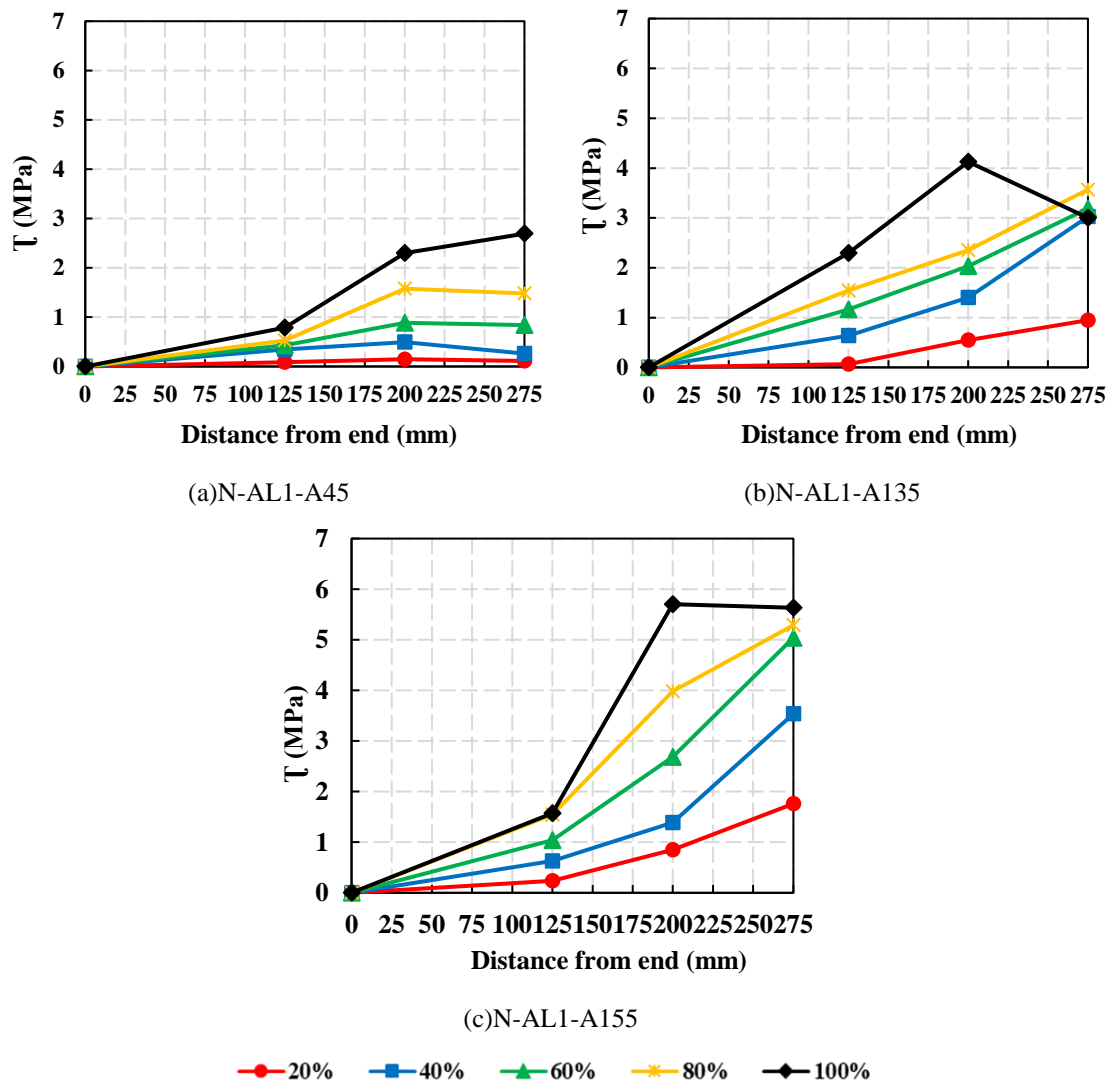
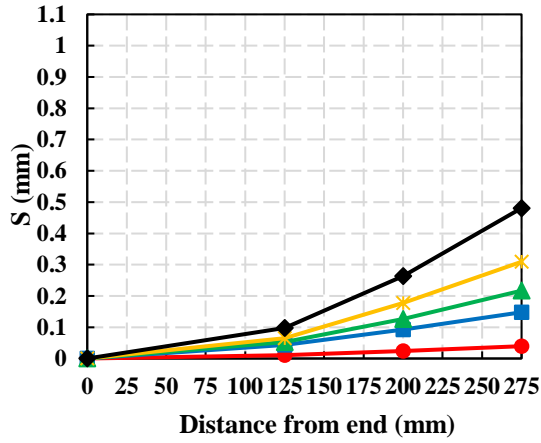
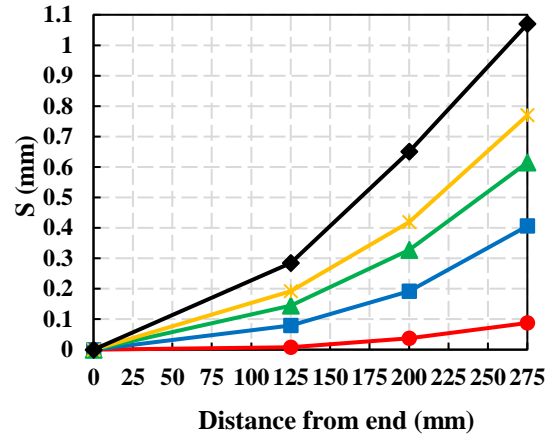


Figure 71: Bond stress vs. slip of anchor dowel angle at different load levels.

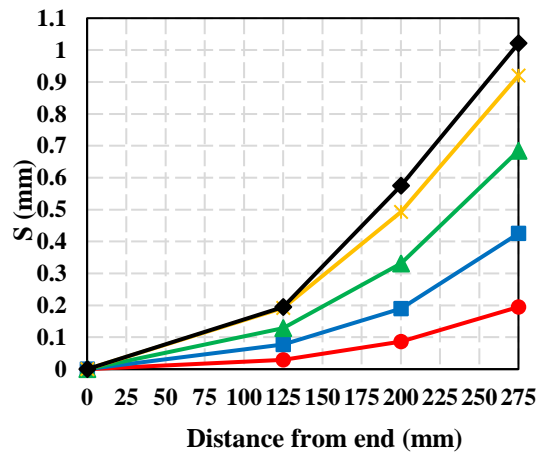
Figure 72 displays the slip versus distance of that group, where slip values significantly increased as a result of increasing the angle from  $45^\circ$  to larger obtuse angles; however, the slip values were close in prisms with anchor dowel angle  $90^\circ$  and more. To sum up, increasing the dowel angle ( $\beta \geq 90^\circ$ ) delays debonding failure by improving the load transfer to the concrete since it resisted larger slip values before failure.



(a)N-AL1-A45



(b)N-AL1-A135



(c)N-AL1-A155

—●— 20%    —■— 40%    —▲— 60%    —\*— 80%    —◆— 100%

Figure 72: Slip vs. distance for anchor dowel angle at different load levels.

## **Chapter 7. Summary and Conclusion**

### **7.1 Summary**

Strengthening of new and existing RC structures using FRP laminates has gained wide acceptance over the last three decades due to the superior effects on the structure. The main issue of strengthening with FRP is premature debonding of the FRP laminates before reaching the maximum capacity of the structure. Therefore, research has shown the importance of using anchoring systems like FRP spike anchors to delay or prevent brittle debonding failure.

There is still a gap in the available literature on the effect of FRP spike anchors on the strength of the structure, and there are no design guidelines in the codes for FRP anchors in flexure. So, more research is required to develop design guidelines and equations for different anchor parameters and configurations. To reduce the research gap, a total of 33 concrete prisms were cast and 30 prisms were strengthened with CFRP laminates and anchors with different anchor parameters like anchor dowel diameter, anchor embedment depth, and anchor dowel angle. Furthermore, 3 control designations were set as benchmark specimens, one unstrengthened prism, one unanchored prism, and one strengthened and anchored prisms with common anchor parameters. All specimens were tested under two-point loading with displacement control rate of 0.25mm/min. The performance of these prisms was studied in terms of load-deflection responses, ultimate load and deflection, strains in CFRP laminates, and bond stress-slip models.

### **7.2 Conclusion**

According to the obtained experimental results of this research, the main findings are:

1. Strengthening concrete structures with CFRP laminates increased the load carrying capacity of the prism by 68%, compared to unstrengthened prism. Moreover, strengthening using CFRP laminates and CFRP spike anchors significantly enhanced the capacity of the prisms in the range of 11%-50% and 88%-153%, compared to unanchored prisms and unstrengthened specimens, respectively.
2. All strengthened prisms failed by debonding of the CFRP laminates. The installation of CFRP anchors was effective in delaying debonding failure,

and thus utilizing the strength of the laminates leading to a ductile failure mode.

3. Unanchored prisms (N-L1) failed by sheet debonding, while the anchored control prism (N-AL1-C) failed by debonding and anchor rupture. Different anchor failure modes were observed for each group. In dowel diameter group, an anchor diameter of 8 mm led to anchor rupture failure along with debonding, while increasing the diameter to 12 mm resulted in debonding failure only. Furthermore, all prisms of embedment depth group failed by anchor rupture and debonding. Dowel angle group encountered two anchor failure modes with debonding, where small angles ( $45^\circ$  and  $90^\circ$ ) failed by anchor rupture and obtuse anchors ( $135^\circ$  and  $155^\circ$ ) by anchor pullout.
4. The inclusion of CFRP splay anchors increased the effective strain in the CFRP laminates. The strain values recorded at ultimate state for the anchored laminates ranged from  $5281 \mu\epsilon$  to  $10642 \mu\epsilon$  compared to  $4699 \mu\epsilon$  in the unanchored laminate. This indicates that the anchors utilized strain in the CFRP laminates in the range of 12-26%.
5. The lowest average strain values were displayed in the unanchored prism N-L1 and the anchored prism N-AL1-D8. Significantly higher strains were observed in prisms N-AL1-E125 and N-AL1-A155 due to the better anchor design.
6. Normalized load values (ratio of anchored load to unanchored load) were plotted for each studied anchor parameter to show anchor efficiency on the structure. It was observed that increasing the value of each parameter resulted in an increase in the efficiency of the anchors.
7. Increasing the anchor dowel diameter from 8 mm to 10 mm showed an increase in the efficiency of the anchors and significantly enhanced the capacity of the prisms by 26%, compared to unanchored prisms. However, increasing the diameter to 12 mm showed a slight enhancement in the capacity of 32%, compared to the 10 mm anchor. The ultimate load capacities recorded in the prisms of the 8-, 10-, and 12-mm anchors were 39.03 kN, 44.18 kN and 46.30 kN, respectively. Further research should be carried out to study the effect of larger dowel diameters with different anchor parameters.

8. A direct relationship was depicted between the anchor embedment depth and the load carrying capacity of the prisms. Prisms with embedment depth of 125 mm demonstrated the best performance in terms of load enhancement and strain utilization. Particularly, the load capacity of specimen A-L1-E125 was 49% more than the unanchored strengthened prism corresponding to 84% strain utilization.
9. Anchor dowel angle showed a consistent pattern where increasing the angle increased the anchor efficiency. Anchors with 135° and 155° angles showed a significant increase in the capacity of 41% and 50%, respectively with respect to unanchored strengthened prism.
10. Bond stress-slip models were obtained for all strengthened prisms. It was observed that all anchored prisms had higher values of bond stress and slip. All designations had their maximum bond stress values at the ultimate load level. In addition, the increase of maximum bond stress, compared to unanchored prisms, ranged between 42% and 336%. Furthermore, the maximum calculated slip increased by 6%-145% when compared to unanchored prism. This implies that the CFRP anchors utilized the bond strength between the laminate and concrete substrate.
11. Different anchor parameters resulted in different behaviors of bond stress and slip graphs. The highest bond stress value calculated was for N-AL1-A155 with a value of 5.70 MPa, corresponding slip of 0.57 mm and max slip of 1.02mm. This indicates that using obtuse angles delayed debonding failure by improving the load transfer to the concrete since it resisted larger slip values before failure.

### **7.3 Suggested Future Work**

The following proposed topics could be addressed in future research:

- Studying the effect of various FRP anchor parameters on the capacity of strengthened specimens.
- Studying the effect of large diameter FRP anchor on the capacity of RC beams in flexure.
- Performance of anchored strengthened specimens with various anchor parameters on the load transfer mechanism.



- Developing bond-slip models for anchored prisms including more anchor parameters and more strain gauges.
- Developing models that predict the FRP anchor capacity for the studied anchor parameters.

## References

- [1] A. Mohammed, J. A. Abdalla, R. A. Hawileh, and W. Nawaz, "Reinforced concrete beams externally strengthened in flexure using hybrid systems," *2018 Adv. Sci. Eng. Technol. Int. Conf. ASET 2018*, February 2018, pp. 1–5.
- [2] A. Siddika, M. A. Al Mamun, R. Alyousef, and Y. H. M. Amran, "Strengthening of reinforced concrete beams by using fiber-reinforced polymer composites: A review," *J. Build. Eng.*, vol. 25, p. 100798, September 2019.
- [3] W. Nawaz, R. A. Hawileh, E. I. Saqan, and J. A. Abdalla, "Effect of longitudinal carbon fiber-reinforced polymer plates on shear strength of reinforced concrete beams," *ACI Struct. J.*, vol. 113, no. 3, pp. 577–586, 2016.
- [4] R. A. Hawileh, H. A. Rasheed, J. A. Abdalla, and A. K. Al-Tamimi, "Behavior of reinforced concrete beams strengthened with externally bonded hybrid fiber reinforced polymer systems," *Mater. Des.*, vol. 53, pp. 972–982, January 2014.
- [5] A. S. D. Salama, R. A. Hawileh, and J. A. Abdalla, "Performance of externally strengthened RC beams with side-bonded CFRP sheets," *Composite Structures*, vol. 212, pp. 281–290, 2019.
- [6] K. Helal, S. Yehia, R. Hawileh, and J. Abdalla, "Performance of preloaded CFRP-strengthened fiber reinforced concrete beams," *Compos. Struct.*, vol. 244, p. 112262, July 2020.
- [7] J. A. Abdalla, A. Mohammed, and R. A. Hawileh, "Flexural strengthening of reinforced concrete beams with externally bonded hybrid systems," *Procedia Struct. Integr.*, vol. 28, pp. 2312–2319, 2020.
- [8] A. Ali, J. Abdalla, R. Hawileh, and K. Galal, "CFRP mechanical anchorage for externally strengthened RC beams under flexure," *Phys. Procedia*, vol. 55, pp. 10–16, October 2014.
- [9] H. A. Rasheed, *Strengthening Design of Reinforced Concrete with FRP*. Boca Raton: CRC Press, 2014, pp. 9-68.
- [10] P. Villanueva Llauradó, T. Ibell, J. Fernández Gómez, and F. J. González Ramos, "Pull-out and shear-strength models for FRP spike anchors," *Compos. Part B Eng.*, vol. 116, pp. 239–252, 2017.

- [11] N. Zhuang, J. Chen, M. Zheng, and D. Chen, "Flexural experimental study on reinforced concrete beams strengthened with carbon fiber-reinforced polymer laminates using anchorage systems," *Materials Express*, vol. 9, no. 8. pp. 923–930, 2019.
- [12] A. K. Al-Tamimi, R. Hawileh, J. Abdalla, and H. A. Rasheed, "Effects of ratio of CFRP plate length to shear span and end anchorage on flexural behavior of SCC RC beams," *J. Compos. Constr.*, vol. 15, no. 6, pp. 908–919, 2011.
- [13] R. A. Hawileh, M. Z. Naser, and J. A. Abdalla, "Finite element simulation of reinforced concrete beams externally strengthened with short-length CFRP plates," *Compos. Part B Eng.*, vol. 45, no. 1, pp. 1722–1730, 2013.
- [14] R. A. Hawileh, H. A. Musto, J. A. Abdalla, and M. Z. Naser, "Finite element modeling of reinforced concrete beams externally strengthened in flexure with side-bonded FRP laminates," *Compos. Part B Eng.*, vol. 173, no. October 2018, p. 106952, 2019.
- [15] M. Naser, R. Hawileh, J. A. Abdalla, and A. Al-Tamimi, "Bond behavior of CFRP cured laminates: Experimental and numerical investigation," *J. Eng. Mater. Technol. Trans. ASME*, vol. 134, no. 2, pp. 1–9, 2012.
- [16] O. R. Abuodeh, J. A. Abdalla, and R. A. Hawileh, "Prediction of shear strength and behavior of RC beams strengthened with externally bonded FRP sheets using machine learning techniques," *Compos. Struct.*, vol. 234, p. 111698, 2020.
- [17] M. Z. Naser, R. A. Hawileh, and J. A. Abdalla, "Fiber-reinforced polymer composites in strengthening reinforced concrete structures: A critical review," *Eng. Struct.*, vol. 198, p. 109542, 2019.
- [18] A. Belarbi and B. Acun, "FRP systems in shear strengthening of reinforced concrete structures," *Procedia Eng.*, vol. 57, pp. 2–8, 2013.
- [19] G. Sakar, R. A. Hawileh, M. Z. Naser, J. A. Abdalla, and M. Tanarslan, "Nonlinear behavior of shear deficient RC beams strengthened with near surface mounted glass fiber reinforcement under cyclic loading," *Mater. Des.*, vol. 61, pp. 16–25, 2014.
- [20] R. A. Hawileh, W. Nawaz, J. Abdalla, and E. Saqan, "External Strengthening of Shear Deficient Reinforced Concrete Beams with Flexural CFRP Laminates," *in*

*Proc. 5th Int. Work. Performance, Prot. Strength. Struct. under Extrem. Load. (PROTECT 2015)*, 2015, pp. 368–373.

- [21] R. Kalfat, R. Al-Mahaidi, and S. T. Smith, “Anchorage devices used to improve the performance of reinforced concrete beams retrofitted with FRP composites: State-of-the-art review,” *Journal of Composites for Construction.* , vol. 17, no. 1, pp. 14–33, Dec. 2011.
- [22] E. del Rey Castillo, R. Kanitkar, S. T. Smith, M. C. Griffith, and J. M. Ingham, “Design approach for FRP spike anchors in FRP-strengthened RC structures,” *Compos. Struct.*, vol. 214, pp. 23–33, 2019.
- [23] ACI Committee 440, "Guide for the Design and Construction of Externally Bonded FRP Systems for Strengthening Concrete Structures (ACI 440. 2R-17)," *American Concrete Institute*, Farmington Hills (MI), 2017.
- [24] D. Zhang, Y. Zhao, and T. Ueda, “Experimental investigation on shear strengthening of corroded reinforced concrete columns by pet fibers with large fracturing strain,” *Int. Conf. Performance-based Life-cycle Struct. Eng.*, 2015, pp. 563–570.
- [25] T. Ochi, S. Okubo, and K. Fukui, “Development of recycled PET fiber and its application as concrete-reinforcing fiber,” *Cem. Concr. Compos.*, vol. 29, no. 6, pp. 448–455, 2007.
- [26] R. N. Nibudey, P. B. Nagarnaik, D. K. Parbat, and A. M. Pande, “A model for compressive strength of PET fiber reinforced concrete," *American Journal of Engineering Research ( AJER )*, Vol. 2, no. 12, pp. 367–372, 2013.
- [27] O. R. Abuodeh, J. A. Abdalla, and R. A. Hawileh, “Flexural strengthening of RC beams using aluminum alloy plates with mechanically-fastened anchorage systems: An experimental investigation,” *Eng. Struct.*, vol. 234, p. 122904, 2021.
- [28] J. A. Abdalla, A. R. Abu-Obeidah, and R. A. Hawileh, “Use of aluminum alloy plates as externally bonded shear reinforcement for R/C beams,” *Procedia Struct. Integr.*, vol. 17, pp. 403–410, 2019.
- [29] O. R. Abuodeh, R. A. Hawileh, and J. A. Abdalla, “Finite element modelling of aluminum alloy plated reinforced concrete beams,” *Comput. Concr.*, vol. 27, no. 6, pp. 585–596, 2021.

- [30] J. A. Abdalla, A. Mirghani, and R. A. Hawileh, "Bond stress and behavior of interface between untreated aluminum alloy surface and concrete," *Procedia Struct. Integr.*, vol. 28, pp. 1295–1302, 2020.
- [31] O. R. Abuodeh, R. A. Hawileh, and J. A. Abdalla, "Nonlinear finite element models of reinforced concrete beams strengthened in bending with mechanically fastened aluminum alloy plates," *Comput. Struct.*, vol. 253, p. 106573, 2021.
- [32] M. H. Baluch, A. R. Khan, A. H. Al-Gadhib, R. A. Barnes, and G. C. Mays, "Fatigue Performance of Concrete Beams Strengthened with CFRP Plates," *J. Compos. Constr.*, vol. 4, no. 4, pp. 215–215, Nov. 2000.
- [33] Y. T. Obaidat, S. Heyden, and O. Dahlblom, "The effect of CFRP and CFRP / concrete interface models when modelling retrofitted RC beams with FEM," *Compos. Struct.*, vol. 92, no. 6, pp. 1391–1398, 2010.
- [34] H. Toutanji and G. Ortiz, "The effect of surface preparation on the bond interface between FRP sheets and concrete members," *Compos. Struct.*, vol. 4, no. 53, pp. 457–462, 2001.
- [35] M. N. Danraka, H. Mahir Mahmod, O.-K. J. Oluwatosin, and P. G. Student, "Strengthening of Reinforced Concrete Beams using FRP Technique: A Review," *Int. J. Eng. Sci. Comput.*, vol. 7, no. 6, pp.13199-13213, 2017.
- [36] J. Tatar and S. Milev, "Durability of externally bonded fiber-reinforced polymer composites in concrete structures: A critical review," *Polymers (Basel)*, vol. 13, no. 5, pp. 1–26, 2021.
- [37] M. Ghous Sohail, N. Al Nuaimi, R. A. Hawileh, J. A. Abdalla, and K. Douier, "Durability of plain concrete prism strengthened with galvanized steel mesh and CFRP laminates under harsh environmental conditions," *Constr. Build. Mater.*, vol. 286, p. 122904, 2021.
- [38] A. F. Ashour, S. A. El-Refaie, and S. W. Garrity, "Flexural strengthening of RC continuous beams using CFRP laminates," *Cem. Concr. Compos.*, vol. 26, no. 7, pp. 765–775, Oct. 2004.
- [39] C. Barris, P. Sala, J. Gómez, and L. Torres, "Flexural behaviour of FRP reinforced concrete beams strengthened with NSM CFRP strips," *Compos. Struct.*, vol. 241, p. 112059, 2020.

- [40] K. M. ud Darain *et al.*, “Strengthening of RC beams using externally bonded reinforcement combined with near-surface mounted technique,” *Polymers (Basel)*, vol. 8, no. 7, p. 261, 2016.
- [41] K. A. Douier, R. A. Hawileh, and J. A. Abdalla, “Behavior of RC Beams externally strengthened with GSM CFRP sheets,” *2020 Adv. Sci. Eng. Technol. Int. Conf. ASET 2020*, 2020, pp. 21–24.
- [42] D. Mostofinejad, S. M. Shameli, and A. Hosseini, “Experimental study on the effectiveness of ebrog method for flexural strengthening of RC beams,” *Proc. 6th Int. Conf. FRP Compos. Civ. Eng. CICE 2012*, no. 4, 2012, p.11025.
- [43] L. De Lorenzis and J. G. Teng, “Near-surface mounted FRP reinforcement: An emerging technique for strengthening structures,” *Composites Part B: Engineering*, vol. 38, no. 2. pp. 119–143, 2007.
- [44] R. A. Hawileh, “Nonlinear finite element modeling of RC beams strengthened with NSM FRP rods,” *Constr. Build. Mater.*, vol. 27, no. 1, pp. 461–471, 2012.
- [45] S. V. Grelle and L. H. Sneed, “Review of Anchorage Systems for Externally Bonded FRP Laminates,” *Int. J. Concr. Struct. Mater.*, vol. 7, no. 1, pp. 17–33, 2013.
- [46] S. V Grelle, “Categorization and experimental evaluation of anchorage systems for fiber-reinforced polymer laminates bonded to reinforced concrete structures,” Master of Science Thesis, Missouri University of Science and Technology, 2011.
- [47] G. M. Chen, J. G. Teng, and J. F. Chen, “Finite-element modeling of intermediate crack debonding in FRP-plated RC beams,” *J. Compos. Constr.*, vol. 15, no. 3, pp. 339–353, 2011.
- [48] T. Mohammadi, B. Wan, K. A. Harries, and M. E. Sweriduk, “Bond Behavior of FRP-Concrete in Presence of Intermediate Crack Debonding Failure,” *J. Compos. Constr.*, vol. 21, no. 5, pp. 1–12, 2017.
- [49] T. Aljaafreh, E. Beneberu, and N. Yazdani, “Anchorage Effect on Flexural Fiber Reinforced Polymer (FRP) Laminate Strengthening of Lightweight Concrete Beams,” *J. Eng. Archit.*, vol. 6, no. 1, pp. 14–25, 2018.

- [50] E. Del Rey Castillo, J. M. Ingham, S. T. Smith, R. Kanitkar, and M. C. Griffith, “A design approach for FRP anchors in FRP-strengthened RC structures,” in *American Concrete Institute, ACI Special Publication*, pp. 1–17, 2017.
- [51] E. del Rey Castillo, D. Dizhur, M. Griffith, and J. Ingham, “Strengthening RC structures using FRP spike anchors in combination with EBR systems,” *Compos. Struct.*, vol. 209, pp. 668–685, 2019.
- [52] A. Singh, E. del Rey Castillo, and J. Ingham, “FRP-to-FRP bond characterization and force-based bond length model,” *Compos. Struct.*, vol. 210, pp. 724–734, 2019.
- [53] H. H. Mhanna, R. A. Hawileh, and J. A. Abdalla, “Shear strengthening of reinforced concrete T-beams using CFRP laminates anchored with bent CFRP splay anchors,” *Procedia Struct. Integr.*, vol. 28, pp. 811–819, 2020.
- [54] W. Sun, H. Liu, Y. Wang, and T. He, “Impacts of configurations on the strength of FRP anchors,” *Compos. Struct.*, vol. 194, pp. 126–135, 2018.
- [55] T. Ozbakkaloglu and M. Saatcioglu, “Tensile Behavior of FRP Anchors in Concrete,” *J. Compos. Constr.*, vol. 13, no. 2, pp. 82–92, Apr. 2009.
- [56] S. J. Kim, S. T. Smith, and M. Asce, “Pullout Strength Models for FRP Anchors in Uncracked Concrete,” vol. 14, pp. 406–414, 2010.
- [57] W. Sun, J. O. Jirsa, and W. M. Ghannoum, “Behavior of anchored carbon fiber-reinforced polymer strips used for strengthening concrete structures,” *ACI Mater. J.*, vol. 113, no. 2, pp. 163–172, 2016.
- [58] H. H. Mhanna, R. A. Hawileh, and J. A. Abdalla, “Effect of FRP Anchor Inclination Angle on Shear Strengthening of Reinforced Concrete T-beams,” *10th International Conference on FRP Composites in Civil Engineering*, Dec. 2021, pp. 2169–2179.
- [59] S. M. S. Syed Mazlan, S. R. Abdullah, S. Shahidan, and S. R. Mohd Noor, “Failure Behaviour of Concrete Prisms Strengthened by Various Bond Widths of Carbon Fibre Reinforced Polymer (CFRP),” *MATEC Web Conf.*, vol. 103, 2017, pp. 102015.
- [60] Y. Murad, “An experimental study on flexural strengthening of RC beams using

- CFRP sheets,” *Int. J. Eng. Technol.*, vol. 7, no. 4, pp. 2075–2080, 2018.
- [61] J. Sim, C. Park, and D. Y. Moon, “Characteristics of basalt fiber as a strengthening material for concrete structures,” *Compos. Part B Eng.*, vol. 36, no. 6–7, pp. 504–512, 2005.
- [62] J. Duic, S. Kenno, and S. Das, “Flexural Rehabilitation and Strengthening of Concrete Beams with BFRP Composite,” *J. Compos. Constr.*, vol. 22, no. 4, pp. 1–11, 2018.
- [63] T. H. Almusallam, “Load-deflection behavior of RC beams strengthened with GFRP sheets subjected to different environmental conditions,” *Cem. Concr. Compos.*, vol. 28, no. 10, pp. 879–889, 2006.
- [64] N. Attari, S. Amziane, and M. Chemrouk, “Flexural strengthening of concrete beams using CFRP , GFRP and hybrid FRP sheets,” *Constr. Build. Mater.*, vol. 37, pp. 746–757, 2012.
- [65] G. Ozdemir and U. AKYUZ, “Tensile Capacities of CFRP Anchors,” *In book: Advances in Earthquake Engineering for Urban Risk Reduction*, pp. 471–487. 2006.
- [66] W. Sun, “Development of a testing methodology for the design and quality control of carbon fiber reinforced polymer (CFRP) anchors,” *Constr. Build. Mater.*, vol. 164, pp. 150–163, 2018.
- [67] A. T. Al-Sammari and S. F. Breña, “Finite element simulation and parametric study of anchored fiber-reinforced polymer sheets,” *ACI Struct. J.*, vol. 115, no. 2, pp. 365–377, 2018.
- [68] J. Lim, J. Kim, E. del Rey Castillo, M. C. Griffith, D. Dizhur, and J. M. Ingham, “Characterization of Bent Fibre Reinforced Polymer (FRP) Anchors Exhibiting Fibre Rupture Failure Mode,” *Proc. New Zeal. Concr. Ind. Conf.*, October 2016, pp.1-11.
- [69] T. Mohammadi, B. Wan, and K. A. Harries, “Bond-slip behavior of fiber-reinforced polymer/concrete interface in single shear pull-out and beam tests,” *J. Reinf. Plast. Compos.*, vol. 35, no. 5, pp. 375–386, 2016.



- [70] ACI Committee 318, "ACI 318-14 Building Code Requirements for Structural Concrete," American Concrete Institute, Farmington Hills (MI), 2014.
- [71] L. Augustus Nelson, M. Al-Allaf, and L. Weekes, "Analytical modelling of bond-slip failure between epoxy bonded FRP and concrete substrate," *Compos. Struct.*, vol. 251, p. 112596, 2020.
- [72] J. C. López-González, J. Fernández-Gómez, and E. González-Valle, "Effect of adhesive thickness and concrete strength on FRP-concrete bonds," *J. Compos. Constr.*, vol. 16, no. 6, pp. 705–711, 2012.
- [73] X. Z. Lu, J. G. Teng, L. P. Ye, and J. J. Jiang, "Bond-slip models for FRP sheets/plates bonded to concrete," *Eng. Struct.*, vol. 27, no. 6, pp. 920–937, 2005.
- [74] L. Augustus Nelson, M. Al-Allaf, and L. Weekes, "Analytical modelling of bond-slip failure between epoxy bonded FRP and concrete substrate," *Compos. Struct.*, vol. 251, p. 112596, 2020.
- [75] R. Castillo, R. Kanitkar, S. T. Smith, M. C. Gri, and J. M. Ingham, "Design approach for FRP spike anchors in FRP-strengthened RC structures," vol. 214, pp. 23–33, 2019.
- [76] K. Masuo, S. Morita, Y. Jinno, and H. Watanabe, "Advanced Wrapping System with CF-anchor-Seismic strengthening of RC columns with Wing Walls," in *FRPRCS-5: Fibre-reinforced plastics for reinforced concrete structures Volume 1*, pp. 299–308, 2015.
- [77] R. Kanitkar, S. T. Smith, and C. Lewis, "An experimental investigation on the splay portion of embedded FRP tension anchors," *Proc. Eighth Int. Conf. Fibre-Reinforced Polym. Compos. Civ. Eng. (CICE 2016)*, 2016, pp.388-398.
- [78] H. W. Zhang and S. T. Smith, "Influence of FRP anchor fan configuration and dowel angle on anchoring FRP plates," *Compos. Part B Eng.*, vol. 43, no. 8, pp. 3516–3527, 2012.
- [79] T. Ozbakkaloglu and M. Saatcioglu, "Tensile behavior of frp anchors in concrete," *J. Compos. Constr.*, vol. 13, no. 2, pp. 82–92, 2009.
- [80] M. Cabinets, M. Rooms, B. Statements, and D. Mass, "Compressive Strength of Hydraulic Cement Mortars ( Using 2-in . or [ 50-mm ] Cube Specimens ) 1,"

*ASTM International*, 2008, pp. 1–9.

- [81] Mape Wrap Primer 1- Epoxy primer specific for the MapeWrap system, Mapei Construction Chemicals LLC, 2019.
- [82] Mape Wrap 31- Medium viscosity epoxy resin for impregnation of MapeWrap with “dry system,” Mapei Construction Chemicals LLC, 2019.
- [83] MapeWrap C UNI-AX - High strength uni-directional carbon fibre fabric with high modulus of elasticity, Mapei Construction Chemicals LLC, 2016.
- [84] ASTM International, “ASTM D 3039M - Standard Test Method for Tensile Properties of Polymer Matrix Composite Materials,” *Annu. B. ASTM Stand.*, vol. 15.03, pp. 1–13, 2008.
- [85] MapeWrap C FIOCCO - High strength uni-directional carbon fibre fabric with high modulus of el Unidirectional high strength carbon fibre cord for impregnation with MapeWrap 21 to make “structural connections”, Mapei Construction Chemicals LLC, 2019.
- [86] ASTM C 1609, “ASTM C1609 Standard test method for flexural performance of fiber-reinforced concrete (using beam with third-point loading).” p. 8, 2010.
- [87] J. O. Jirsa, W. A. Shekarchi, D. K. Pudleiner, and H. Wang, “Use of Carbon Fiber Reinforced Polymer ( CFRP ) with CFRP Anchors for Shear-Strengthening and Design Recommendations/Quality Control Procedures for CFRP Anchors,” *The National Academics of Sciences Engineering Medicine*, no.1, p.6783, 2017.
- [88] M. Griffith, J. M. Ingham, and N. Zealand, “Force-based model for straight FRP anchors exhibiting fibre,” *The 8th International Conference on Fibre-Reinforced Polymer (FRP) Composites in Civil Engineering (CICE 2016)*, 2013, pp. 2–9.
- [89] W. Sun and W. M. Ghannoum, “Modeling of anchored CFRP strips bonded to concrete,” *Constr. Build. Mater.*, vol. 85, pp. 144–156, 2015.
- [90] P. Villanueva Llauradó, J. F. Gómez, and F. J. González Ramos, “Influence of the Anchor Fan Position on the Performance of FRP Anchors,” in *High Tech Concrete: Where Technology and Engineering Meet*, pp. 191–198, 2018.
- [91] U. Akyuz and G. Ozdemir, “Mechanical Properties of Cfrp Anchorages,” *13th World Conf. Earthq. Eng.*, 2004, pp.456-478.

- [92] S. J. Kim and S. T. Smith, “Behaviour of Handmade FRP Anchors under Tensile Load in Uncracked Concrete,” *Advances in Structural Engineering*, vol. 12, no. 6, pp. 845–866, 2009.
- [93] D. Pudleiner, W. M. Ghannoum, and J. O. Jirsa, “Influence of Anchor Size on Anchored CFRP Systems,” *J. Compos. Constr.*, vol. 23, no. 5, p. 04019033, 2019.
- [94] P. V. Llauradó, T. Ibell, J. F. Gómez, and F. J. G. Ramos, “Pull-out and shear-strength models for FRP spike anchors,” *Composites: Part B*, vol. 116, pp. 239–252, 2017.
- [95] E. del Rey Castillo, D. Dizhur, M. Griffith, and J. Ingham, “Strengthening RC structures using FRP spike anchors in combination with EBR systems,” *Compos. Struct.*, vol. 209, pp. 668–685, 2019.
- [96] H. W. Zhang, S. T. Smith, and S. J. Kim, “Optimisation of carbon and glass FRP anchor design,” *Constr. Build. Mater.*, vol. 32, pp. 1–12, 2012.
- [97] E. del Rey Castillo, D. Dizhur, M. Griffith, and J. Ingham, “Strengthening RC structures using FRP spike anchors in combination with EBR systems,” *Compos. Struct.*, vol. 209, pp. 668–685, 2019.
- [98] J. Wang, “Debonding of FRP-plated reinforced concrete beam, a bond-slip analysis. I. Theoretical formulation,” *Int. J. Solids Struct.*, vol. 43, no. 21, pp. 6649–6664, 2006.
- [99] C. Pellegrino, D. Tinazzi, and C. Modena, “Experimental Study on Bond Behavior between Concrete and FRP Reinforcement,” *J. Compos. Constr.*, vol. 12, no. 2, pp. 180–189, 2008.
- [100] C. Mazzotti, M. Savoia, and B. Ferracuti, “An experimental study on delamination of FRP plates bonded to concrete,” *Construction and Building Materials*, vol. 22, no. 7, pp. 1409–1421, 2008.
- [101] B. Ferracuti, M. Savoia, and C. Mazzotti, “Interface law for FRP – concrete delamination,” *Composite Structures*, vol. 80, no. 4, pp. 523–531, 2007.
- [102] J. A. Abdalla, F. H. Hraib, R. A. Hawileh, and A. M. Mirghani, “Experimental investigation of bond-slip behavior of aluminum plates adhesively bonded to concrete,” *J. Adhes. Sci. Technol.*, vol. 31, no. 1, pp. 82–99, 2017.

## Appendix

### Sample Calculations - Bond-slip Models

Table 14: Sample Calculations - Strain values of N-AL1-155.

Strains :	$\varepsilon_1$	$\varepsilon_2$	$\varepsilon_3$	$\varepsilon_4$
Distance from end:	@0 mm	@125 mm	@200 mm	@275 mm
0.2 P	0	0.000475	0.001202	0.00257
0.4 P	0	0.001244	0.002147	0.005455
0.6 P	0	0.00206	0.004018	0.00806
0.8 P	0	0.00307	0.005969	0.009366
1P	0	0.003122	0.008038	0.009824

#### Equations:

$$\tau(x_i) = \frac{1}{2} n_f t_f E_f \left[ \frac{(\varepsilon_i - \varepsilon_{i-1})}{(x_i - x_{i-1})} + \frac{(\varepsilon_{i+1} - \varepsilon_i)}{(x_{i+1} - x_i)} \right]$$

$$s(x) = s(0) + \sum_{i=n}^i \frac{1}{2} [(\varepsilon_i - \varepsilon_{i-1})(x_i - x_{i-1}) + (\varepsilon_{i+1} - \varepsilon_i)(x_{i+1} - x_i)]$$

#### Calculations:

At 20%  $P_u$ :

Bond stress,  $\tau$  (MPa)

$$\tau(0) = 0$$

$$\tau(1) = \frac{1}{2} (1 \times 0.5 \times 252000) \left[ 0 + \frac{(0.000475 - 0)}{(125 - 0)} \right] = 0.240 \text{ MPa}$$

$$\tau(2) = \frac{1}{2} (1 \times 0.5 \times 252000) \left[ \frac{(0.000475 - 0)}{(125 - 0)} + \frac{(0.001202 - 0.000475)}{(200 - 125)} \right] = 0.850 \text{ MPa}$$

$$\tau(3) = \frac{1}{2} (1 \times 0.5 \times 252000) \left[ \frac{(0.001202 - 0.000475)}{(200 - 125)} + \frac{(0.00257 - 0.001202)}{(225 - 200)} \right] = 1.76 \text{ MPa}$$

Slip, S (mm)

$$s(0) = 0$$

$$s(1) = 0 + \frac{1}{2}[0 + (0.000475 - 0)(125 - 0)] = 0.0297 \text{ mm}$$

$$s(2) = 0 + 0.029704 + \frac{1}{2}[(0.000475 - 0)(125 - 0) + (0.001202 - 0.000475)(200 - 125)] \\ = 0.0867 \text{ mm}$$

$$s(3) = 0 + 0.0297 + 0.086 \\ + \frac{1}{2}[(0.001202 - 0.000475)(200 - 125) + (0.00257 - 0.001202)(225 - 200)] \\ = 0.195 \text{ mm}$$

**At 40% P<sub>u</sub>:**

Bond stress,  $\tau$  (MPa)

$$\tau(0) = 0$$

$$\tau(1) = \frac{1}{2}(1 \times 0.5 \times 252000) \left[ 0 + \frac{(0.00124 - 0)}{(125 - 0)} \right] = 0.627 \text{ MPa}$$

$$\tau(2) = \frac{1}{2}(1 \times 0.5 \times 252000) \left[ \frac{(0.00124 - 0)}{(125 - 0)} + \frac{(0.00215 - 0.00124)}{(200 - 125)} \right] = 1.386 \text{ MPa}$$

$$\tau(3) = \frac{1}{2}(1 \times 0.5 \times 252000) \left[ \frac{(0.00215 - 0.00124)}{(200 - 125)} + \frac{(0.00546 - 0.00215)}{(225 - 200)} \right] = 3.537 \text{ MPa}$$

Slip, S (mm)

$$s(0) = 0$$

$$s(1) = 0 + \frac{1}{2}[0 + (0.00124 - 0)(125 - 0)] = 0.0778 \text{ mm}$$

$$s(2) = 0 + 0.0778 + \frac{1}{2}[(0.00124 - 0)(125 - 0) + (0.00215 - 0.00124)(200 - 125)] \\ = 0.189 \text{ mm}$$

$$s(3) = 0 + 0.0778 + 0.189 \\ + \frac{1}{2}[(0.00215 - 0.00124)(200 - 125) + (0.00546 - 0.00215)(225 - 200)] \\ = 0.425 \text{ mm}$$

**At 60% P<sub>u</sub>:**

Bond stress,  $\tau$  (MPa)

$$\tau(0) = 0$$

$$\tau(1) = \frac{1}{2}(1 \times 0.5 \times 252000) \left[ 0 + \frac{(0.00206 - 0)}{(125 - 0)} \right] = 1.038 \text{ MPa}$$

$$\tau(2) = \frac{1}{2}(1 \times 0.5 \times 252000) \left[ \frac{(0.00206 - 0)}{(125 - 0)} + \frac{(0.00402 - 0.00206)}{(200 - 125)} \right] = 2.682 \text{ MPa}$$

$$\tau(3) = \frac{1}{2}(1 \times 0.5 \times 252000) \left[ \frac{(0.00402 - 0.00206)}{(200 - 125)} + \frac{(0.00806 - 0.00402)}{(225 - 200)} \right] = 5.040 \text{ MPa}$$

Slip, S (mm)

$$s(0) = 0$$

$$s(1) = 0 + \frac{1}{2}[0 + (0.00206 - 0)(125 - 0)] = 0.129 \text{ mm}$$

$$s(2) = 0 + 0.0778 + \frac{1}{2}[(0.00206 - 0)(125 - 0) + (0.00402 - 0.00206)(200 - 125)] \\ = 0.331 \text{ mm}$$

$$s(3) = 0 + 0.0778 + 0.189 \\ + \frac{1}{2}[(0.00402 - 0.00206)(200 - 125) + (0.00806 - 0.00402)(225 - 200)] \\ = 0.685 \text{ mm}$$

**At 80% P<sub>u</sub>:**

Bond stress,  $\tau$  (MPa)

$$\tau(0) = 0$$

$$\tau(1) = \frac{1}{2}(1 \times 0.5 \times 252000) \left[ 0 + \frac{(0.00307 - 0)}{(125 - 0)} \right] = 1.547 \text{ MPa}$$

$$\tau(2) = \frac{1}{2}(1 \times 0.5 \times 252000) \left[ \frac{(0.00307 - 0)}{(125 - 0)} + \frac{(0.00597 - 0.00307)}{(200 - 125)} \right] = 3.982 \text{ MPa}$$

$$\tau(3) = \frac{1}{2}(1 \times 0.5 \times 252000) \left[ \frac{(0.00597 - 0.00307)}{(200 - 125)} + \frac{(0.00937 - 0.00597)}{(225 - 200)} \right] = 5.289 \text{ MPa}$$

Slip, S (mm)

$$s(0) = 0$$

$$s(1) = 0 + \frac{1}{2}[0 + (0.00307 - 0)(125 - 0)] = 0.192 \text{ mm}$$

$$s(2) = 0 + 0.0778 + \frac{1}{2}[(0.00307 - 0)(125 - 0) + (0.00597 - 0.00307)(200 - 125)] \\ = 0.492 \text{ mm}$$

$$s(3) = 0 + 0.0778 + 0.189 \\ + \frac{1}{2}[(0.00597 - 0.00307)(200 - 125) + (0.00937 - 0.00597)(225 - 200)] \\ = 0.920 \text{ mm}$$

**At 100% P<sub>u</sub>:**

Bond stress,  $\tau$  (MPa)

$$\tau(0) = 0$$

$$\tau(1) = \frac{1}{2}(1 \times 0.5 \times 252000) \left[ 0 + \frac{(0.00312 - 0)}{(125 - 0)} \right] = 1.573 \text{ MPa}$$

$$\tau(2) = \frac{1}{2}(1 \times 0.5 \times 252000) \left[ \frac{(0.00312 - 0)}{(125 - 0)} + \frac{(0.00804 - 0.00312)}{(200 - 125)} \right] = 5.703 \text{ MPa}$$

$$\tau(3) = \frac{1}{2}(1 \times 0.5 \times 252000) \left[ \frac{(0.00804 - 0.00312)}{(200 - 125)} + \frac{(0.00982 - 0.00804)}{(225 - 200)} \right] = 5.630 \text{ MPa}$$

Slip, S (mm)

$$s(0) = 0$$

$$s(1) = 0 + \frac{1}{2}[0 + (0.00312 - 0)(125 - 0)] = 0.195 \text{ mm}$$

$$s(2) = 0 + 0.0778 + \frac{1}{2}[(0.00312 - 0)(125 - 0) + (0.00804 - 0.00312)(200 - 125)] \\ = 0.575 \text{ mm}$$

$$s(3) = 0 + 0.0778 + 0.189 \\ + \frac{1}{2}[(0.00804 - 0.00312)(200 - 125) + (0.0111 - 0.00804)(225 - 200)] \\ = 1.021 \text{ mm}$$

## **Vita**

Ghusoon Subhi Alshami was born in 1998, in Abu Dhabi, United Arab Emirates. She graduated from high school in 2015 from International Community School. She joined Abu Dhabi University in fall of 2015 where she pursued Bachelor of Science degree in Civil Engineering and graduated in spring 2019. In Fall 2019, she joined the Civil Engineering master's program in the American University of Sharjah and was awarded a graduate teaching assistantship. She graduated from the master program in Fall 2021. Her research interest lies in structures and rehabilitation and strengthening of concrete structures.